UNIVERSIDADE FEDERAL DO CEARÁ
CENTRO DE TECNOLOGIA
DEPARTAMENTO DE ENGENHARIA HIDRÁULICA E AMBIENTAL
PROGRAMA DE PÓS-GRADUAÇÃO EM ENGENHARIA CIVIL

ARTHUR JORDAN DE AZEVEDO TONÉ

MODELING RIVER-AQUIFER INTERACTIONS IN DRYLAND REGIONS TO ENHANCE WATER MANAGEMENT STRATEGIES

FORTALEZA
2026

ARTHUR JORDAN DE AZEVEDO TONÉ

MODELING RIVER-AQUIFER INTERACTIONS IN DRYLAND REGIONS TO ENHANCE WATER MANAGEMENT STRATEGIES

Tese apresentada ao Programa de Pós-Graduação em Engenharia Civil da Universidade Federal do Ceará, como requisito parcial à obtenção do título de Doutor em Engenharia Civil. Área de concentração: Recursos Hídricos.

Orientador: Prof. Dr. Iran Eduardo Lima Neto.
Coorientador: Prof. Dr. Alexandre Cunha Costa.

FORTALEZA
2026

ARTHUR JORDAN DE AZEVEDO TONÉ

MODELING RIVER-AQUIFER INTERACTIONS IN DRYLAND REGIONS TO ENHANCE WATER MANAGEMENT STRATEGIES

Tese apresentada ao Programa de Pós-Graduação em Engenharia Civil da Universidade Federal do Ceará, como requisito parcial à obtenção do título de Doutor em Engenharia Civil. Área de concentração: Recursos Hídricos.

Orientador: Prof. Dr. Iran Eduardo Lima Neto.
Coorientador: Prof. Dr. Alexandre Cunha Costa.

Aprovada em: 09/03/2026.

BANCA EXAMINADORA

Prof. Dr. Iran Eduardo Lima Neto (Orientador)
Universidade Federal do Ceará (UFC)

Prof. Dr. Alexandre Cunha Costa (Coorienador)
Universidade da Integração Internacional da Lusofonia Afro-Brasileira (UNILAB)

Prof. Dr. Cleiton da Silva Silveira
Universidade Federal do Ceará (UFC)

Prof. Dr. Rodolfo Bezerra Nobrega
University of Bristol (UoB)

Prof. Dr. Adriano Rolim da Paz
Universidade Federal da Paraíba (UFPB)

Profa. Dra. Suzana Maria Gico Lima Montenegro
Universidade Federal de Pernambuco (UFPE)

Prof. Dr. François Molle
Institut de Recherche pour le Développement (IRD)

A Deus e a Nossa Senhora.

À minha esposa amada, Talyta.

Aos meus filhos.

Aos meus pais.

Ao meu irmão.

Aos meus familiares.

AGRADECIMENTOS

À Fundação Coordenação de Aperfeiçoamento de Pessoal de Nível Superior (CAPES), pelo apoio financeiro mediante bolsa durante cinco meses deste doutorado, e que, por breve que tenha sido, ajudou-me bastante.

Ao Instituto Federal de Educação, Ciência e Tecnologia do Ceará (IFCE), por permitir o afastamento para que eu terminasse este doutorado.

Ao Prof. Dr. Iran Eduardo Lima Neto, por ter aceitado ser meu orientador desde 2012, ainda na iniciação científica, quando eu era jovem e sem experiência de vida, e que, nestes 14 anos, tornou-se um verdadeiro pai, mestre e amigo.

Ao Prof. Dr. Alexandre Cunha Costa, por ser um coorientador paciente, sábio e bondoso. Eu não teria conseguido concluir este caminho do doutorado sem as suas orientações.

Aos membros da banca examinadora, pela bondade e disposição em sacrificar algumas horas de seus compromissos diários para contribuir com a defesa da tese.

À minha amada esposa Talyta, por quem gasto amorosamente e alegremente todos os meus dias para fazê-la feliz, e através dela agradeço à paciência dos meus amados filhos.

Aos meus amados pais, irmão, avós, sogros e familiares, por todo o apoio diuturno desde o princípio.

Enfim, agradeço a Deus e à Nossa Senhora por tantos bens que não mereço.

“Confia no Senhor com todo o teu coração, não te fies em tua própria inteligência.” (Provérbios 3,5)

RESUMO

A segurança hídrica depende da representação precisa dos processos hidrológicos na dinâmica rio-aquífero, incluindo a recarga de aquíferos decorrente da precipitação, o escoamento hiporreico e o escoamento lateral de tributários. Estudos sobre a interação rio-aquífero e modelos de *hedging* frequentemente negligenciam estes processos. Este estudo propõe um modelo perceptual das interações rio-aquífero em regiões com escassez de dados (Capítulo 2). Com base neste modelo perceptual, foi desenvolvido um modelo numérico parcimonioso, e esses processos foram calculados com precisão significativa numa região com escassez de dados, em escalas relevantes para a gestão hídrica (Capítulo 3). Além disso, apresenta-se um modelo numérico de *hedging* para um reservatório em regiões secas, dispondo de um sistema de racionamento antecipado baseado na identificação de eventos de seca e na dinâmica rio-aquífero (Capítulo 4). Foram analisados dados hidrológicos de curto prazo medidos em campo, juntamente com dados secundários sobre hidrogeologia, uso da água, participação dos usuários e imagens de satélite. Os resultados do Capítulo 2 indicam que as perdas médias em trânsito variaram de 12% a 28% da vazão de entrada no rio, enquanto os ganhos em trânsito variaram de 10% a 34%. As perdas em trânsito foram prevalentes no início da estação chuvosa (precipitação ≤ 10 mm/dia), ao passo que os ganhos em trânsito foram dominantes após eventos de precipitação intensa (> 20 mm/dia). Os resultados do Capítulo 3 indicam que as medidas de desempenho do modelo numérico (eficiência de Kling-Gupta, eficiência de Nash-Sutcliffe e viés percentual) estimam eficazmente o escoamento fluvial e subterrâneo utilizando uma abordagem de modelação simples, requerendo apenas uma calibração mínima (três parâmetros). De modo particular, os dados necessários para o modelo estão frequentemente disponíveis em regiões com escassez de dados. A análise de sensibilidade dos parâmetros do modelo simplificado demonstrou que a condutividade hidráulica do leito do rio e a largura do aquífero afetaram significativamente a vazão de saída em ambientes com escassez de dados. O escoamento hiporreico se mostrou crucial para o balanço hídrico em rios de regiões secas. Em contrapartida, o escoamento superficial da sub-bacia demonstrou uma influência pequena em comparação com a vazão de entrada e o escoamento de água subterrânea, sugerindo uma maior dependência do volume e do nível do rio do que da precipitação intra-sazonal. No Capítulo 4, o modelo de *hedging* apresenta vantagens importantes, incluindo a otimização de variáveis de decisão (volumes de gatilho e coeficientes de racionamento) utilizando um algoritmo genético (NSGA-II), a integração da participação dos usuários de água, a alocação de água conectada a avaliações de seca através de um índice de seca simples, a previsão de vazão baseada na dinâmica rio-aquífero e o uso de dados hidrológicos de curto prazo medidos em campo. Os resultados mostram que a regra de *hedging* proposta manteve a vulnerabilidade do sistema abaixo de 10%, utilizando dados de escoamento tanto simulados quanto medidos, e a função objetivo (o índice de escassez modificado) foi otimizada com sucesso, mesmo quando o racionamento antecipado ocorreu durante a estação chuvosa. A análise quantitativa sugere que, para um *hedging* adaptativo em regiões secas com escassez de dados, o método de cálculo (a própria regra) é mais crítico do que a disponibilidade de medições de escoamento *in situ*. Portanto, as regras de operação para um reservatório em regiões secas otimizadas com dados simulados podem ser eficazes para satisfazer as demandas hídricas e os requisitos das partes interessadas, mesmo quando integradas a um índice de seca simples e na presença de incertezas nos dados. Este estudo contribui para um balanço hídrico mais preciso dos principais processos hidrológicos em regiões com escassez de dados e fornece ferramentas valiosas para áreas semelhantes que requerem soluções de gestão viáveis.

Palavras-chave: interação rio-aquífero; região semiárida; gerenciamento de recursos hídricos; regras de *hedging*

ABSTRACT

Water security relies on accurately representing hydrological processes in river-aquifer dynamics, including aquifer recharge driven by rainfall, hyporheic flow, and lateral tributary inflow. River–aquifer studies and hedging models often overlook these processes. This study proposes a conceptual model of river-aquifer interactions in data-scarce regions (Chapter 2). Building on this conceptual model, a parsimonious numerical model was developed, and these processes were accurately calculated in a data-scarce region at scales relevant to water management (Chapter 3). Furthermore, a numerical hedging model for a dryland reservoir, featuring an early rationing system based on the identification of drought events and river-aquifer dynamics, is presented (Chapter 4). Short-term field-measured hydrological data were analyzed along with secondary data on hydrogeology, water use, water participation, and satellite imagery. The results from Chapter 2 indicate that the average transmission losses ranged from 12% to 28% of river inflow, while the transmission gains ranged from 10% to 34%. Transmission losses were prevalent at the beginning of the rainy season (rainfall ≤ 10 mm/day), whereas transmission gains were dominant following intense rainfall events (> 20 mm/day). The results from Chapter 3 indicate that the numerical model's performance measures (Kling-Gupta efficiency, Nash–Sutcliffe efficiency, and percent bias) effectively estimate river and groundwater flow using a simple modeling approach, requiring only minimal calibration (three parameters). Notably, the data required for the model are often available in regions with scarce data. Sensitivity analysis of the simplified model parameters showed that riverbed hydraulic conductivity and aquifer width significantly affected outflow in data-scarce environments. Hyporheic flow is crucial for the water balance in dryland rivers. In contrast, subcatchment runoff demonstrated minimal influence compared to inflow and groundwater fluxes, suggesting a greater dependence on river volume and stage than on intraseasonal rainfall. In Chapter 4, the heading model has key advantages, including the optimization of decision variables (trigger volumes and rationing coefficients) using a genetic algorithm (NSGA-II), integration of water user participation, water allocation connected with drought assessments through a simple drought index, streamflow prediction based on river-aquifer dynamics, and the use of short-term field-measured hydrological data. The results show that the proposed hedging rule maintained system vulnerability below 10% using both simulated and measured inflow data, and the objective function (the modified shortage index) was successfully optimized, even when early rationing occurred during the rainy season. The quantitative analysis suggests that for adaptive hedging in data-scarce drylands, the calculation method (the rule itself) is more critical than the availability of on-site inflow measurements. Therefore, operating rules for a dryland reservoir optimized using simulated data may be effective in satisfying water demands and stakeholder requirements, even when integrated with a simple drought index and in the presence of data uncertainties. This study contributes to a more accurate water balance of key hydrological processes in data-scarce regions and provides valuable tools for similar areas that require viable management solutions.

Keywords: river-aquifer interaction; semi-arid region; water management; hedging rules

LIST OF FIGURES

LIST OF TABLES

LIST OF ABBREVIATIONS AND ACRONYMS

ANA	Agência Nacional de Águas e Saneamento Básico
ADS	Airbus Defence And Space
FUNCEME	Fundação Cearense de Meteorologia e Recursos Hídricos
COGERH	Companhia de Gestão dos Recursos Hídricos do Ceará
CPRM	Companhia de Pesquisa de Recursos Minerais
INMET	Instituto Nacional de Meteorologia
UFC	Universidade Federal do Ceará

TABLE OF CONTENTS

1 INTRODUCTION

1.1 Background and overview

Drylands are environments where water is a critical limiting factor for human systems and land use. These regions are home to nearly 40% of the global population, most of whom already face fluctuations in water access, availability, and quality. Extreme droughts, the frequency of which is expected to increase, and decreasing storage of surface water pose appreciable challenges to water management decisions. These challenges may have profound consequences for drylands and their populations in the near future (Daramola; Xu, 2022; Stringer *et al.*, 2021). Therefore, climate change and human factors, such as dam operation policies and water consumption patterns, could significantly affect streamflow processes, which are crucial for quantifying groundwater storage and direct runoff (Saedi *et al.*, 2022).

Streamflow is a key component of the hydrological cycle and arises particularly from the interaction of geomorphological characteristics of the underlying conditions and meteorological processes (Swain *et al.*, 2020). Many studies have employed machine learning, physically based, and parametric hydrological models to forecast streamflow in dryland regions with limited observational data (for instance, Costa *et al.*, 2012; Kim *et al.*, 2022; Pacheco-Guerrero *et al.*, 2017; Rabelo *et al.*, 2021; Yang *et al.*, 2020). These models are typically applied at small catchment or basin scales and require many parameters to be regionally computed or calibrated, yet, as numerical models, they can effectively handle long-term hydrological series (Saedi *et al.*, 2022; Sood; Smakhtin, 2015).

Nevertheless, Addor and Melsen (2019) identified a tendency within the scientific community to select hydrological models based on factors such as practicality, and adequacy, meaning the model's ability to represent the hydrological processes relevant to the extent of the objective's scope. Ideally, this criterion of adequacy should be met by grounding hydrological modeling in a well-defined conceptual model, as the accuracy of hydrological simulations in data-scarce regions largely depends on the model's structure (Devia; Ganasri; Dwarakish, 2015; Guo *et al.*, 2021). The conceptual model should clearly outline its assumptions, even when not directly based on field measurements, to enhance the reproducibility of model-driven decisions and, consequently, the overall modeling work (Horton; Schaefli; Kauzlaric, 2022).

For the criterion of practicality, it is important to underline that uncertainties related to hydrological modeling arise not only from the model structure and calculations but also from the quality of hydrological data and the density of hydrological gauges (Guo *et al.*, 2021; Horton; Schaefli; Kauzlaric, 2022). One method to improve hydrological data and, consequently, enhance the accuracy of calibration parameters is the use of remote sensing data (Gui *et al.*, 2019). Nevertheless, a long-term series of measured streamflow data remains essential for ensuring the best calibration results, which is a fundamental step in hydrological modeling (Guo *et al.*, 2021).

In this context, this thesis aims to develop a numerical hydrological model that is both practical and adequate for predicting streamflow in data-scarce dryland regions, at a daily time step and at a basin scale. These conditions are crucial for efficient water management policies and river operations (Kim *et al.*, 2022; Ntona *et al.*, 2022). This approach is developed for streamflow in river-aquifer dynamics, as it is a key hydrological component for an adequate analysis of the hydrological cycle. The numerical model will be grounded in a conceptual model, developed from a long-term series of measured streamflow data and supported by remote sensing observations. It aims to describe all the hydrological processes that combine to generate streamflow, including those often neglected in river-aquifer studies, such as hyporheic flow (Hussain; Wu; Shih, 2022; Mujere *et al.*, 2022). The measured data will enhance the reliability of the calibration process, and the numerical model aims to minimize the number of parameters requiring calibration, ensuring its practicality for application in water resources management.

Furthermore, as reservoirs are often the sole water source in drylands (Lopes; Freitas, 2007), effective operation during droughts is important to mitigate supply demand imbalances. While existing operation models generally seek to minimize deficits or maximize economic benefits, few have proposed adaptive operation rules for multi-use dryland reservoirs that account for both the rapid impacts of climate change on streamflow and river-aquifer interactions (Mujere *et al.*, 2022; Coulibaly *et al.*, 2025). Consequently, this thesis aims to develop a numerical operation rule that integrates water allocation with drought assessment and river-aquifer hydrological processes, offering a valuable tool for management in data-scarce arid environments.

1.2 Objectives

The general objective of this thesis is to model river-aquifer interactions in dryland regions at the basin scale to improve water resource management strategies in these areas. This task will be achieved through three specific objectives:

1. To develop a conceptual model of the dominant processes in river-aquifer dynamics at the basin scale for a dryland river.

2. To develop a parsimonious numerical model to simulate hydrological processes in river-aquifer dynamics.

3. To develop a hedging rule for a data-scarce dryland reservoir that seeks to balance the complexity of water allocation, drought assessment, and dryland hydrological processes while maintaining operational simplicity.

1.3 Outline of the thesis

The daily monitoring of runoff events in a dry region on a basin-scale and the development of a conceptual model of the river-aquifer interaction will be shown in Chapter II. This model proposes an explanation for the observed data, highlighting the important contributions of hyporheic flow and baseflow to river flow, in addition to the rainfall volumes directly over the river. Chapter III focuses on the development of a simple numerical model for river-aquifer interactions in dryland rivers. It is designed to address data scarcity and more accurately represent hydrological processes, including aquifer recharge driven by rainfall, hyporheic flow, and lateral tributary inflow. A more precise representation of these processes at the basin scale in a dry region could enhance water security in Northeast Brazil by offering valuable insights into water management.

Chapter IV proposes an optimized hedging rule for a large reservoir system in Northeast Brazil, building on the insights and methods developed in Chapters II and III. Chapter V presents the general conclusions of this study and recommendations for future work. Chapters II, III, and IV were written as independent manuscripts that have either been published or are awaiting publication in international peer-reviewed journals. Full references are provided on the front page of each chapter.

2 SPATIOTEMPORAL RIVER-AQUIFER INTERACTIONS OF A LARGE TROPICAL DRYLAND RIVER WITH HIGH ANTHROPIC INTERVENTION[1]

2.1 Introduction

The interaction between surface water and groundwater along river reaches occurs in a wide variety of landscapes and depends on geomorphological, geological and climatological aspects. The riverbed controls the interactions, depending on the hydraulic and sedimentological mechanisms working on the river. In dry regions with high seasonal and interannual rainfall variability, such as semi-arid areas in the tropics, loss of river water toward the soil through infiltration, known as channel transmission losses, is an important component of watershed water balance. These losses play a significant role in groundwater recharge and serve as one of its primary sources (Brunner *et al.*, 2017; Karlović *et al.*, 2021).

Channel transmission losses can occur in all rivers, whether allogenic (typically perennial) or endogenic (typically intermittent or ephemeral) (Bull; Kirkby, 2002). Natural transmission losses also encompass the amount of water that is lost to the atmosphere through direct evaporation from the river and evapotranspiration occurring in the surrounding riparian zone (McMahon; Nathan, 2021). Anthropogenic activities in dry regions, such as river damming or groundwater extraction through artificial pumping in areas adjacent to the river, can intensify transmission losses, thereby reducing water availability downstream (Costa *et al.*, 2013; Rabelo *et al.*, 2021). When the water table is higher than the river stage, groundwater flows toward the river from the saturated zone, resulting in transmission gains that can potentially compensate for the losses (Choi, 2017). The magnitude of these water exchanges in river-aquifer interaction depends on the hydraulic gradient between these systems, in addition to the hydraulic conductivity of the riverbed (Sophocleous, 2002; Woessner, 2000).

The analysis of this interaction is important for an integrated management of

---

[1] A paper based on the content of this chapter has been published in the *Hydrological Sciences Journal* as Toné, A. J. A., Costa, A. C., Gonçalves Barros, M. U., Barros de Freitas, H., Vasconcelos Cavalcante, J. R., & Lima Neto, I. E. (2023). Spatiotemporal river–aquifer interactions of a large tropical dryland river with high anthropic intervention. *Hydrological Sciences Journal*, *68*(14), 2009–2026.

surface and groundwater resources and for the maintenance of ecological habitat and river runoff regime (Costa *et al.*, 2012; Kim *et al.*, 2022; Mujere *et al.*, 2022; Sophocleous, 2002; Wang *et al.*, 2021). Recent studies on river-aquifer interaction in dry regions, based on data analysis of surface and groundwater flows, have focused on China, East Africa, South Africa, the United States, Australia and Saudi Arabia (Hughes, 2019; Kim *et al.*, 2022; McMahon; Nathan, 2021; Wang; Pozdniakov; Vasilevskiy, 2017), with few studies conducted in large rivers (Brunner *et al.*, 2017). Large rivers are heterogeneous and complex systems with normally high anthropic intervention, where the anthropogenic-modified hydrological processes operating on a multi-kilometre scale can significantly influence the interaction between river flow and the underlying groundwater flow at spatial and temporal scales (Boano *et al.*, 2014).

Global land regions are expected to confront unprecedented drought conditions over the next three decades, with an increase in the frequency of drought days compared to past historical occurrences (Satoh *et al.*, 2022). The impact on the flow regime of large rivers is expected to be notable due to the decrease in precipitation and the corresponding temporal variation in groundwater contribution to river flow (Carvalho *et al.*, 2020; Wang *et al.*, 2021). Addressing river-aquifer interactions is especially important for water security, particularly where they occur over long distances in warmer climate conditions (Kim *et al.*, 2022).

The aim of this research is to investigate the river-aquifer interaction in large dryland river with high anthropic intervention. The specific objectives are: (1) to quantify water flux between river reaches; (2) to identify the threshold that governs predominant hydrological behaviours in the river (influent/effluent); (3) to investigate the relationship between transmission losses/gains and the inflow volume per river reach; and (4) to formulate a conceptual model of the dominant processes in the river-aquifer interaction. The experimental site is a part of the Jaguaribe River, the largest semiarid river in Brazil. This study is relevant not only for large dryland environments, but also for other anthropic-modified environments under different climates since: (a) it considers the water resource management scale with the analysis of three contiguous river reaches (71 km in total) that drain an area of 38,000 km^2; (b) it analyses direct field measurements of river level and flow rate in four stream gauges during a complete rainy season (six months) in a dry region, where hydrological data are scarce, to estimate induced transmission losses or gains; and (c) it integrates daily hydrological data from a dryland area with multi-temporal satellite imagery to investigate the spatiotemporal dynamics of water flux between the surface and groundwater in a large river.

Additionally, the scarcity of studies in South America is notorious and makes it difficult to understand the dynamics between surface and groundwater in large rivers in the region, especially in drylands. One of the last studies on the river-aquifer interaction in a large river in the Brazilian dry region was a decade ago (Costa *et al.*, 2013). The authors verified the influent/effluent nature of the river (influent in the dry season, influent/effluent in the rainy season), the hydraulic connection between the river and the alluvium, the occurrence of transmission losses only in riverbed and the predominant influence of infiltration and baseflow in predicting river flow and transmission losses. More recently, Cunha (2017) proposed a conceptual model of river-aquifer interaction on a basin-scale in the dry region of the State of Bahia, Brazil, focusing on the hydrological cycle processes that influence water flows on a large scale, and from a limited amount of data observed in the field. Sandoval *et al.* (2018) analysed the river-aquifer interaction in 60 km of river in the dry region of Chile with monthly and annual rainfall and river flow data, monitored in one rain gauge and stream gauge, respectively, and verified the control of river flow by the baseflow. Gomez *et al.* (2022) highlighted the absence of studies on the river-aquifer interaction in a dry region of Argentina and evaluated that existing hydrological studies do not allow an effective water resources management. To the best of our knowledge, a study encompassing characteristics (a) through (c) in the dryland regions of South America has not yet been conducted.

2.2 Data and methods

2.2.1 Study site

Located in the semiarid region of northeastern Brazil, State of Ceará, the Jaguaribe River is the largest river there, with 610 km length, draining an area of 74,000 km2, with cross-section widths ranging from 60 to 450 m in the main channel and slopes ranging from 1.0 to 0.3 m.km-1 from its headwater to the mouth (Figure 1). The region is characterized by a rainy season concentrated from January to June, with an annual rainfall average between 500 and 1,000 mm, and high annual potential evapotranspiration, estimated at 2,200 mm, from which there is a high local water deficit. The causes of rainfall variability in the region range from the influence of the

Atlantic Intertropical Convergence Zone, the main active meteorological factor for rainy conditions, to descending air currents and relief. In addition, the site is marked by sporadic floods and periodic droughts (Cavalcante, 2018; Costa; Bronstert; De Araújo, 2012; Costa *et al.*, 2020; de Araújo; Bronstert, 2016; Raulino; Silveira; Lima Neto, 2021). Reservoirs store most of the surface water resource in the region (Campos, 2015); Castanhão and Orós reservoirs are the largest ones, and the study site is located upstream and downstream them, respectively.

The river reaches under analysis span 71 km and are situated within the Middle Jaguaribe basin, draining an area of 2,898 km^2. In this study, water flow in the river reaches is measured using four stream gauges (N1, N2, N3, and N4) (Figure 1). While the N3 gauge is provided by ANA, the remaining gauges were specifically installed for this research. N1 gauge receives the contribution from the drainage basin of the Salgado River and the Orós reservoir (38,000 km^2), and the N4 gauge monitors river flow downstream, at the entrance of the Castanhão reservoir. Despite its proximity to the reservoir, field measurements (section 2.2.4) confirmed that the N4 gauge remained unaffected by the backwater influence and operated under free-flow conditions throughout the study period. The distances between stream gauges are: - N1-N2: 34,719 km (reach 1); - N2-N3: 15,231 km (reach 2); - N3-N4: 20,956 km (reach 3).

The geology in the study site is composed of a Precambrian crystalline basement (85%), metamorphic and igneous lithologies, under a Cenozoic alluvium (clay, sand and gravel) (15%) (Figure 2). Borborema Province, geological context of the study site, is characterized by fractures and structural lineaments (faults that influence sediment deposition and the local drainage system), with predominantly NE-SW and E-W orientation, as well as shear zones from the Brasiliano Cycle, width between 1 and 5 km, which cut kilometres of land with various lithologies, and with predominantly E-W and NE-SW orientation. These characteristics influence the study site relief, which is arranged in a sequence of highs and valleys according to the orientation of the structural lineaments and shear zones (Costa *et al.*, 2013; de Araújo; Bronstert, 2016; Maia; Bezerra, 2020).

The alluvial deposit (granular unit) along the analysed river is a free and discontinuous aquifer, with a maximum thickness of 25 m, and with very low productivity (private consumption and local supplies), having a hydraulic conductivity of 8,640 mm/d, with a significant variability of the groundwater level (CPRM, 2014, 2015; Palheta; Holanda; Gomes, 2019). The crystalline rock is connected to the alluvium (Kreis *et al.*, 2020; Lachassagne; Dewandel; Wyns, 2021), and it is a discontinuous medium with saline water flow through preferential paths, with a hydraulic conductivity of 0.860 mm/d, and without regional flow (CPRM, 2015).

Water demand at the study site is divided into human supply and irrigation, currently relying on 13 water-use permits. COGERH assumes that the flows granted correspond to the flows effectively withdrawn and does not identify relevant uses of water beyond those granted (COGERH, 2017). In this sense, groundwater exploitation with tubular wells in the alluvium supplies irrigation demands (0.22 hm^3/y), whereas water volume for human supply is derived from the Jaguaribe River (0.17 hm^3/y) (COGERH, 2023).

Figure 1 - The location of the analyzed rivers within the Middle Jaguaribe basin is shown, with the study site highlighted in relation to the Castanhão and Orós reservoirs.

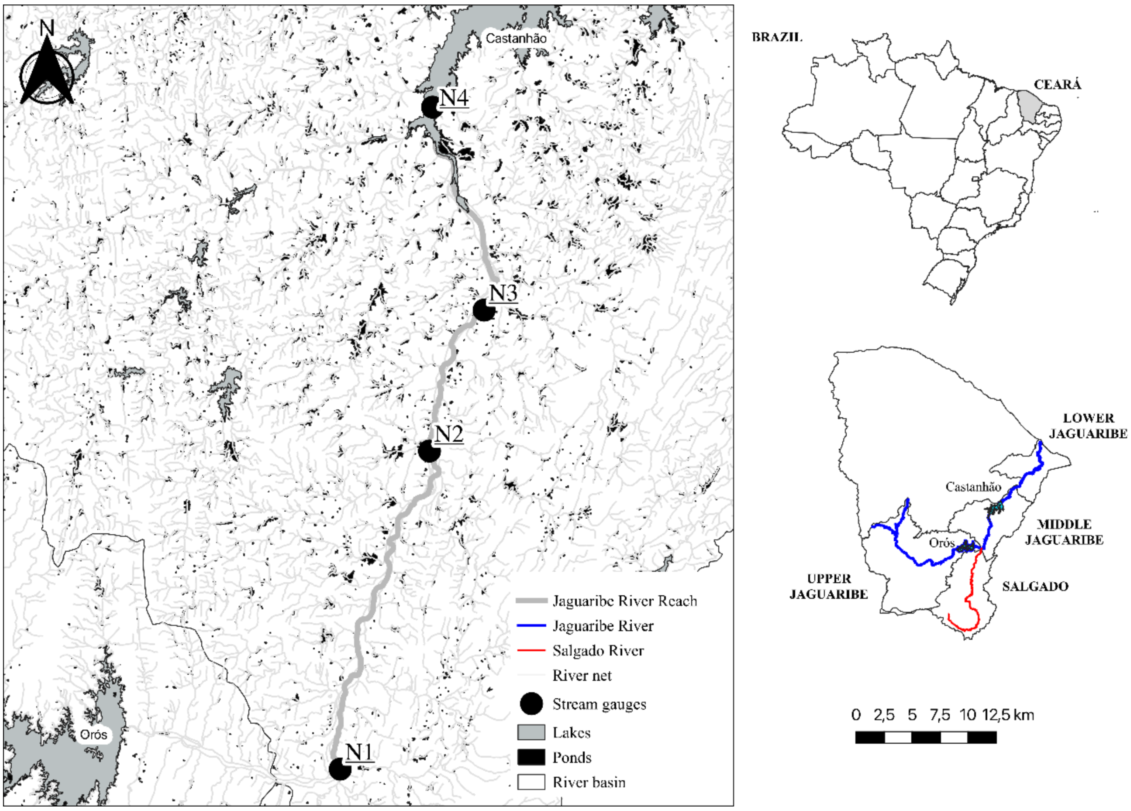

Source: prepared by the author.

Figure 2 - Hydrological and geological characterization of the study site, with identification of rain gauges, stream gauges and withdraw points for demand supply.

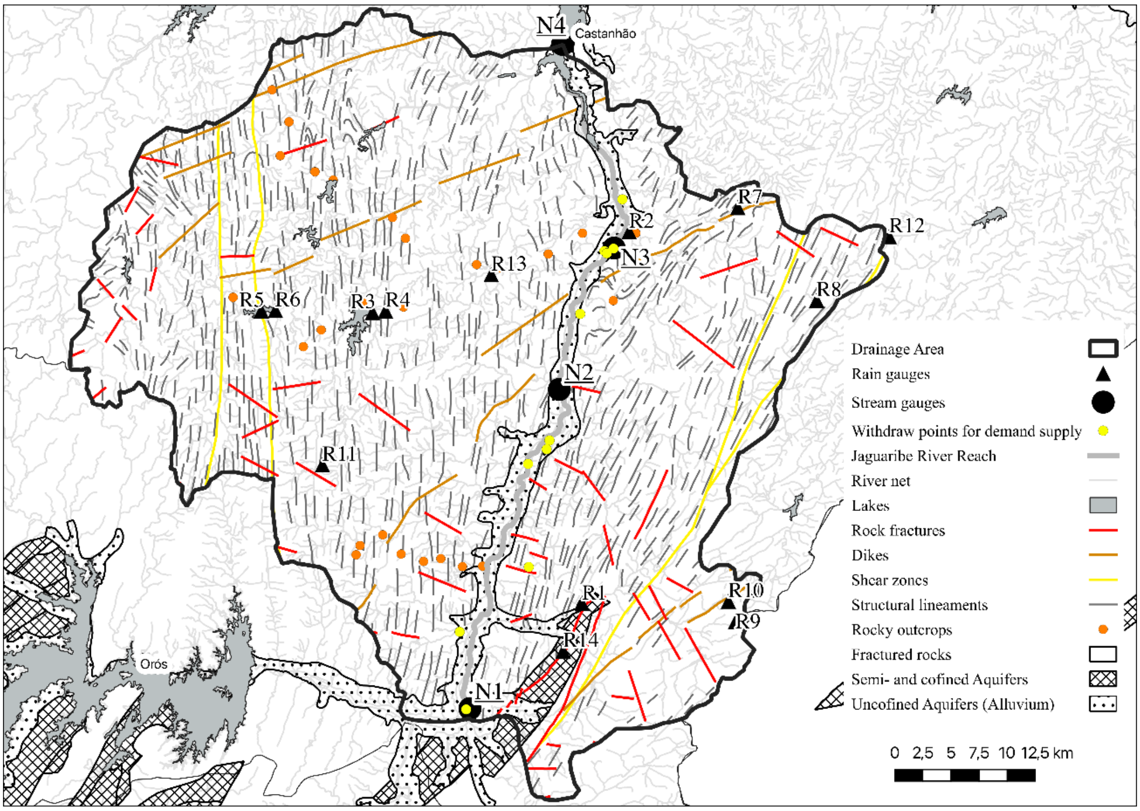

Source: prepared by the author.

2.2.2 Topographic data

The European Space Agency (ESA) provides, through Planetary Data Access (PANDA) (see https://panda.copernicus.eu), the Copernicus GLO-30 digital elevation model (DEM) (1-arcsec. X-band radar) covering the entire surface of the planet, with satellite images acquired between 2011 and 2015 during the TanDEM-X mission. The model was got from WorldDEM™, a digital surface model that includes bodies of water and rivers (ADS, 2023; Guth *et al.*, 2021). Guth and Geoffroy (2021) used point clouds collected from LiDAR, and concluded that Copernicus DEM GLO-30 has a consistently superior performance than digital elevation models such as SRTM, NASADEM, ASTER and ALOS for different relief, vegetation and terrain slope. The elevations and terrain slope were obtained from the Copernicus DEM data using the free Geographic Information System (GIS) software QGIS.

Sophocleous (2002) details topographic factors that can influence the mechanism of the river-aquifer interaction: (1) the channel width-depth ratio (W/WL)—and, therefore, the channel geometry; (2) the river slope and sinuosity; and (3) the valley lateral slope. Data (2) and (3) were obtained from the Copernicus DEM GLO-30, allowing the analysis of their relationship with the river-aquifer interaction in the Jaguaribe river. As for the information in (1), ANA provides the river bathymetry in the N3 gauge for different years. These factors were compared with the surface and groundwater flows between the river and the alluvium.

2.2.3 Hydrogeologic data

The CPRM provides the geological maps of the municipalities where the study site is located (CPRM, 2014; Palheta; Holanda; Gomes, 2019), including the estimation of the fractured rock and alluvium depths, besides the map of the hydrogeological units and the estimate of hydraulic conductivity for the different aquifers (CPRM, 2015) (Table 1). Moreover, as the difference in hydraulic conductivity of the riverbed and alluvium influences the flow rate (Woessner, 2000), the sediments hydraulic conductivity in the riverbed was estimated by the Hazen method, applicable to sands with effective grain size between 0.1 and 3.0 mm, considering the granulometric analysis of the sediments in the Jaguaribe River performed by Wiegand (2009), with grain sizes close to those obtained in other studies at this river (Cavalcante, 2001; Gama *et al.*, 2017; Ximenes Neto *et al.*, 2018).

The daily groundwater flow extracted to meet water demand was obtained from the database of water use permits maintained by COGERH (see http://outorgasvigentes.cogerh.com.br/), following the proposal of the Water Safety Plan for Watersheds of Ceará (COGERH, 2017). The location of the tubular wells used for pumping were obtained from the CPRM Groundwater Information System (see http://siagasweb.cprm.gov.br/layout/). Since there is no regional flow in the study site (Kreis *et al.*, 2020), the lateral groundwater flow to the alluvium was considered null.

Table 1 - Aquifers' hydraulic conductivity.

	Fractured Rocks	**Alluvium**	**Semi- and confined aquifer**
K (mm/d)†	0.860	8.640	0.860

Source: † Data from CPRM (2015) for the study area.

2.2.4 Hydrologic data

River stage levels were measured daily throughout the first half of 2022 at the N1, N2, N3 and N4 stream gauges. The measurements occurred at 07:00 am and 05:00 pm, defining the average value of the measurements as the water level in the gauges. An Acoustic Doppler Current Profiler (SonTek RiverSurveyor M9 ADCP) was used to measure river flow (Figure S2.1, supplementary material). SonTek M9 uses a 5 beam echo sounder for channel definition and generates a 2D velocity map of the river section to integrate and compute river discharge. The discharge and river stage were used to generate the rating curves at the stream gauges. The daily flowed volume was measured within a 24-hour interval, from 07:00 on the day before the analysis.

The runoff events in the river were identified and delimited by the first point of the ascension curve and the point between the end of the recession curve and the beginning of another hydrograph. The wave travel time was estimated empirically from the difference in days of peak flows at the N1 to N4 stream gauges. They were approximately equal to 1 day between contiguous stream gauges and 3 days between N1 and N4 gauges.

The location and daily rainfall data from the 14 rain gauges in the drainage basin (Figure 2) were obtained in the "Rainfall Calendar of the State of Ceará" from the FUNCEME (see http://www.funceme.br/app-calendario/). Average rainfall on the study site was compute through the Thiessen Polygons method, widely used in hydrology and meteorology (Akhter *et al.*, 2022), with FUNCEME's Hydrological Calculation and Water Allocation software "SIGA" (see http://www.funceme.br/siga/). The daily actual evapotranspiration (ETa) within the drainage basin was obtained from INMET's database at the Jaguaribe station, situated near the N3 gauge. ETa calculations were performed using the climatic water balance (CWB) method proposed by (Thornthwaite; Mather, 1995). The reference evapotranspiration (ETo) for the study area was determined using the Penman-Monteith FAO method (Allen *et al.*, 1998), with a standard crop chosen to accurately represent the surrounding land. Figure 3 shows the seasonal variability of rainfall and evapotranspiration in the study site, besides river stage and river flow in N3 gauge, which has the longest time series in the analysed area.

Figure 3 - Monthly average (red line) of (a) rainfall, (b) actual evapotranspiration, (c) river stage level, and (d) river flow in study site. The gray region shows the interval of the 90th percentile per month.

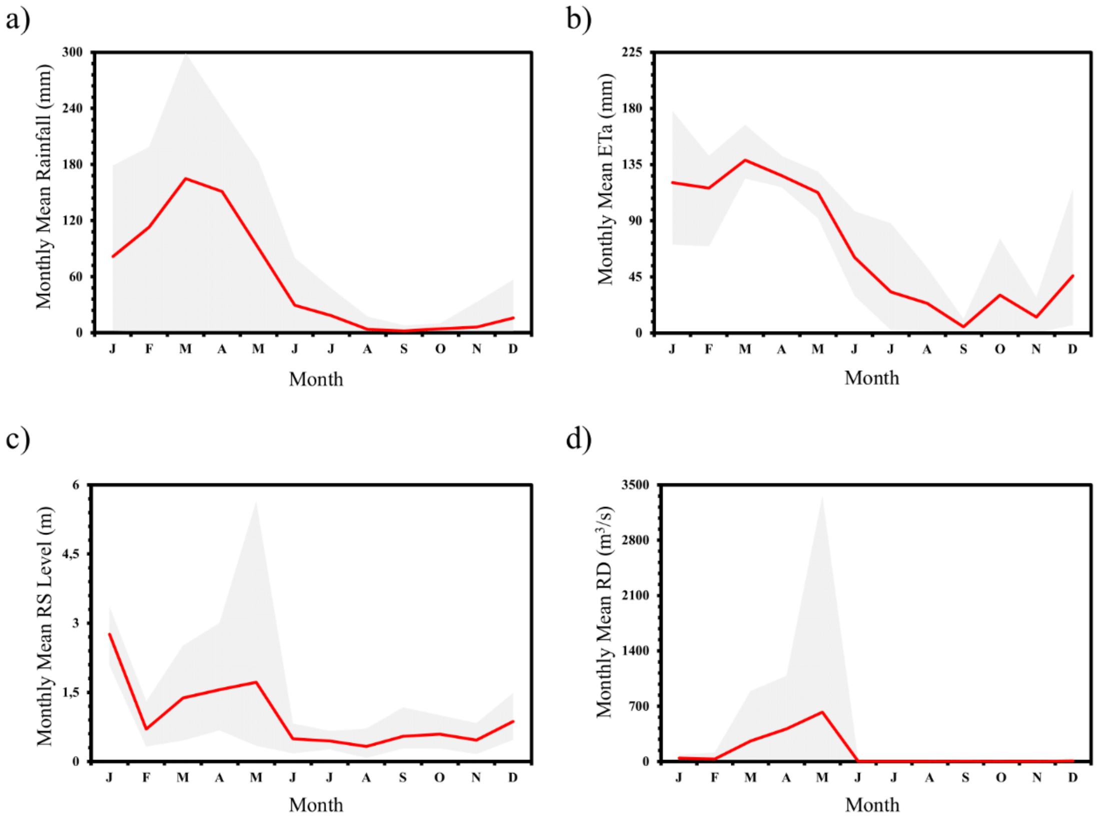

Source: prepared by the author.

2.2.5 Quantification of river-aquifer interaction

The natural river-aquifer interaction will be quantified in the river reaches (1, 2 and 3) between the stream gauges (N1, N2, N3 and N4) per runoff event. It will be computed as:

$$\Omega^i = (O^i_{t+\Delta t} - I^i_t) + \pi^i - \partial^i + \mu^i \qquad (2.1)$$

$$I^{i+1}_t = O^i_{t+\Delta t} \qquad (2.2)$$

Where Ω is the quantification of the natural river-aquifer interaction (10^6 m^3), positive for transmission gains and negative for transmission losses in the river reach; i is the indicator of the river reach (1 to 3); t is the time step and Δt is the duration of the runoff event in the river reach, corresponding to 1 day; I and O are the inflow and outflow in the reach, respectively (10^6 m^3) (Mengistu *et al.*, 2019).

The value of π results from the vertical water balance of the volumes over the river reach along the runoff event (10^6 m^3), i.e., rainfall and evapotranspiration. It will be computed through the equation of Kim *et al.* (2022) adapted:

$$\pi = a^i (P_{event} - ETa_{event}) \tag{2.3}$$

$$a^i = B^i L^i \tag{2.4}$$

Where a is the river area (m^2); B is the cross-section top width (m), obtained from the bathymetric data and remote sensing (section 2.6), assumed time-invariant if there is not discharge beyond river channel, for the sake of efficiency; L is the river length (m) (section 2.1). ETa_{event} (m) e P_{event} (m) are the data of actual evapotranspiration and rainfall, respectively, per runoff event.

The value of ∂ corresponds to the water volume for demand supply in each river reach (groundwater exploitation from operating wells and pumping from the river), since they influence the decrease in the river stage (10^6 m^3) (Gomez *et al.*, 2022; Peterson, 1988). The value of ∂ is equivalent to the sum of the daily induced discharge in the river reach multiplied by the pumping regime during the runoff event. Considering the analysis of the river-aquifer interaction for daily runoff events, the indicative of Costa *et al.* (2022) was followed for the pumping regime: for pumped flow up to 50 m^3/h, the operating time was estimated at 8 hours/day; for higher flows, a time of 20 hours/day was estimated.

The value of μ corresponds to the lateral contribution of surface runoff to the river reach (10^6 m^3) per runoff event. It was estimated from the SCS-CN method, whose method was described in detail by (Mishra; Singh, 2003), and was computed by:

$$\mu = A^i [(P_{event} - 0.2S^i)^2/(P_{event} + 0.8S^i)] \tag{2.5}$$

Where A is the area of the incremental basin of the river reach (m^2); S is the potential maximum soil retention in the incremental basin (m). There will be μ if $P_{event} \geq 0.20$ S, corresponding to the initial abstraction. This depends on the CN parameter (curve number) according to equation 2.6. Since each river reach drains an incremental basin area greater than 15 km^2 (Ramakrishnan; Durga Rao; Tiwari, 2008), the curve number will be computed from a weighted average of the CN values of the individual areas that compose each incremental basin (Rajasekhar *et al.*, 2020), according to equation 2.7.

$$S^i = 25400/CN^i_w - 254 \quad (2.6)$$

$$CN^i_w = \sum (CN_j\, A^i_j)/A^i \quad (2.7)$$

In which CN_w is the weighted curve number; A_j is the individual area (m^2) that composes the incremental basin drained by the river reach with a specific CN_j. ANA (2018) cross-located data on land use and soil occupation in Brazil with pedological data and hydrological classes (A, B, C and D) of Brazilian soils, and provided a vector base with the CN value for the Brazilian Hydrographic Base (see https://metadados.snirh.gov.br/geonetwork/), considering a type 02 precondition of soil moisture. Figure S2.2 (supplementary material) shows CN values for the study site; each CN value is related to an individual area in the river reach incremental basin (A_j). The identification of the actual precondition of soil moisture was performed from the daily rainfall data measured in the FUNCEME's rain gauges (see section 2.4). The correction of the CN value for the preconditions of humidity type 01 or 03 was carried out according to equations 2.8 and 2.9 (Mishra; Singh, 2003):

$$CN_1 = 4.2\, CN_2/(10\text{-}0.058CN_2) \quad (2.8)$$

$$CN_3 = 23\, CN_2/(10+0.13CN_2) \quad (2.9)$$

A form of direct global assessment of the relevance of transmission losses (natural and induced by pumping) in relation to the inflow and outflow in the river reach per runoff event (R) is shown in equation 2.10. Since the lateral contribution of surface runoff can influence the calculation of the transmission losses, R was not computed for μ_i values greater than 4% of the inflow in the river reach (I^i_t) (Costa *et al.*, 2013).

$$R^i = (O^i_{t+\Delta t} - I^i_t) / I^i_t \quad (2.10)$$

Where R ≥ 0 may indicate null, compensated or exceeded transmission losses by the runoff from the drainage basin between stream gauges, but also the recharging of the reach through the subsurface flow or baseflow (Musy; Higy, 2011). Negative R values show the loss of river flow to the aquifer (Izady *et al.*, 2014).

2.2.6 Spatial variability of water dynamics in Jaguaribe river

RapidEye satellite images were used to analyse the spatial variation of the water surface within the Jaguaribe River from the N1 stream gauge to the N4. The images have a spatial resolution of 5 m (blue, green, red, red and near-infrared border) and were obtained from the Geo Catalog of the Ministry of the Environment (see http://geocatalogo.mma.gov.br/). The Ministry offers the images in high resolution for four years of reference (2011-2014), with complementary images for the years 2012 and 2015.

In order to delimit the geometry of the river reaches, bathymetry data at the N3 gauge was used, and satellite images were discarded: (1) if captured in the rainy season (January to June); (2) with excessive cloud cover. The mapping of the extent of the water surface was done with images captured in the rainy season and through the analysis of the ratio between the red band and the near-infrared band. Both methods were successfully performed, in whole or in part, previously by Costa *et al.* (2013) and Pereira (2017) for the Jaguaribe River. The data obtained, i.e., bathymetric and remote sensing data, will allow to quantify the endmember π in equation 2.1.

2.3 Results

2.3.1. Riverscape geomorphology

The terrain elevation (Figure 4) and the river reaches slope characterize the study site as river plain (≤ 3%) (Table 2), but without regional flow, contrary to the trend present in flat reliefs (Kreis *et al.*, 2020). Longitudinal valley presented the same slope as the Jaguaribe river, and the lateral valley had a small slope. The hydraulic conductivity of riverbed sediments by Hazen's method can be seen in Table 3. The value is 10^4 times higher than the conductivity of the alluvial.

Table 2 - River reach slope.

Parameter	Reach 01	Reach 02	Reach 03
ΔH† (m)	20.53	0.39	19.61
Length (km)	37.72	15.23	20.96
Slope (m/km)	0.59	0.03	0.94

† Difference between stream gauges elevation heights.

Source: prepared by the author.

Table 3 - Hydraulic conductivity of riverbed sediments.

Mean Grain Size (mm)†	Shape Factor	Expoent	K (mm/d)
0.90	450	1.65	115,272.30

Source: † Data from Wiegand (2009) for the Jaguaribe River.

Figure 4 - Terrain elevation at the study site, with emphasis on the analyzed Jaguaribe River reach.

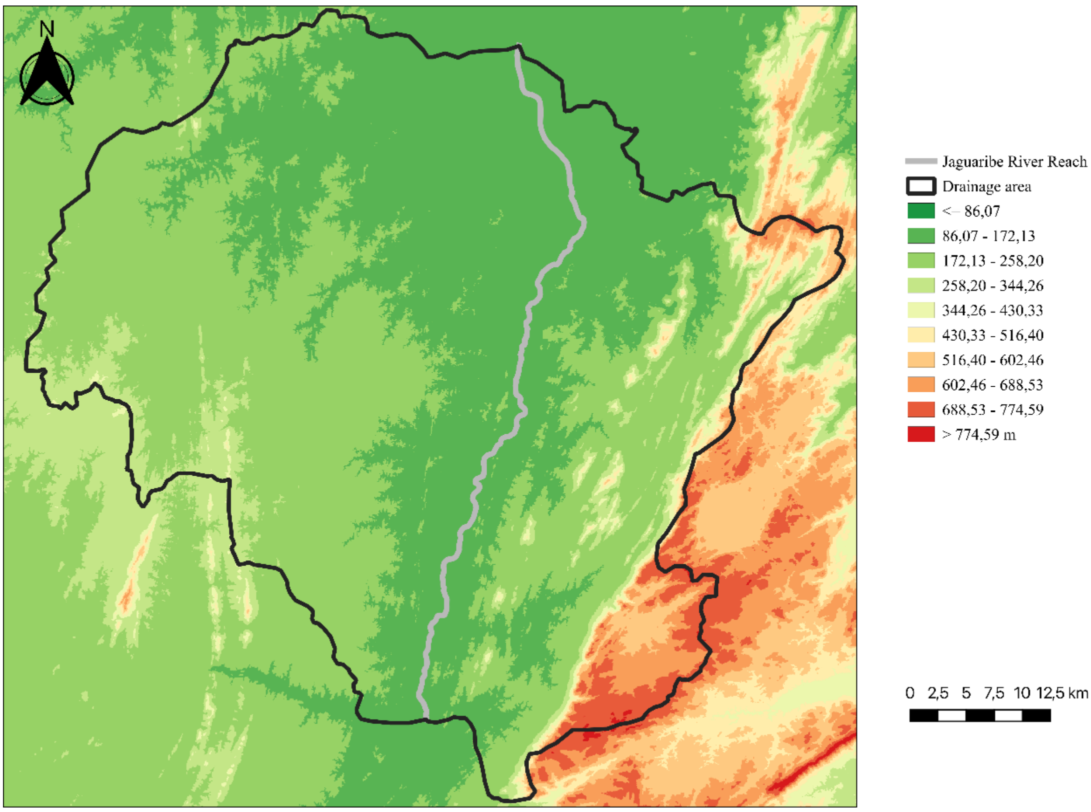

Source: prepared by the author.

The stability of the river cross-section at N3 stream gauge, made available by ANA for different years, can be seen in Figure 5, with a low width-depth ratio (W/WL) (< 20.50 m). The water surface within the Jaguaribe River, derived from the RapidEye images collected over a five-year period (2011-2015) (not shown here), was confined to the river's streambed (Figure 2.6). Since the water level did not exceed the main channel throughout the river, the W/WL ratio was considered the same for the Jaguaribe River, with a B = 344.65 m.

Figure 5 - The stability of the cross-section of the Jaguaribe River at the N3 stream gauge for different years.

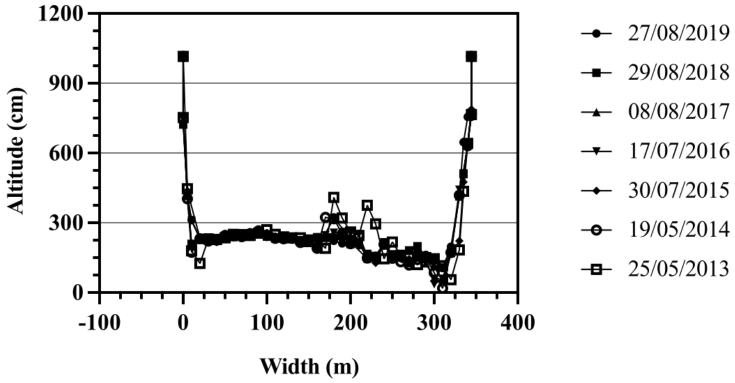

Source: prepared by the author.

Figure 6 - Water surface within the Jaguaribe river from satellite image collected exactly during a flood event in the rainy season. Image collected on 01 June 2014.

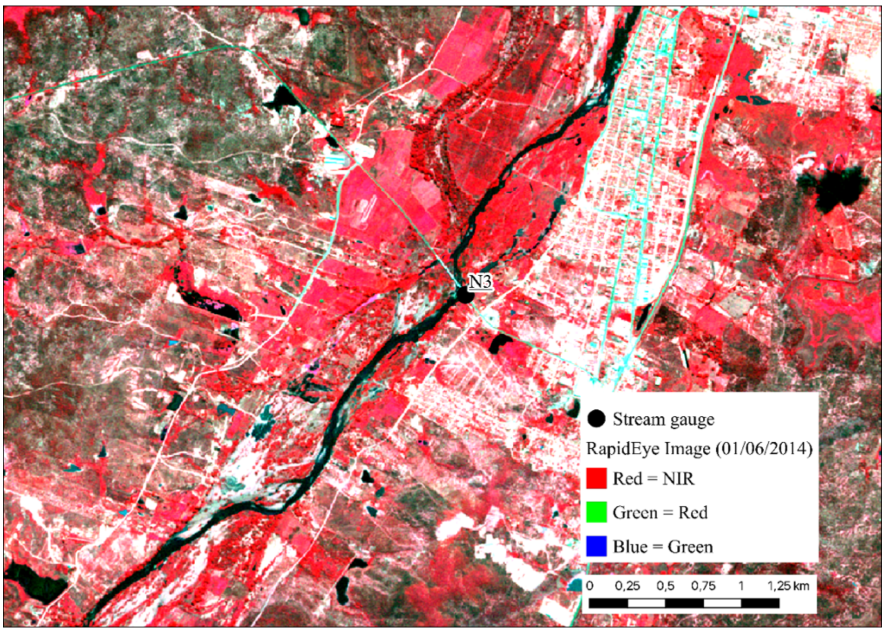

Source: prepared by the author.

2.3.2 River Hydrology

Figure S2.3 (supplementary material) and Table 4 show the rating curves of the river reaches at the study site, wherein water level is the difference measured in the rulers between streamflow and streambed levels in each stream gauge. During the 168 measurement days, between January 4 and June 14, 2022, there were no episodes of null river flow in the river reaches, because a reservoir releases water upstream from the study site (Figure 7). The median of the water levels and discharges decreased from the stream gauges N1 to N2 and from N3 to N4, and from N1 to N4, but grew between N2 and N3 (Figures 7a and 7b).There was a linear behaviour between the river flow monitored in N1 in relation to the river flow monitored in N2, N3 and N4 (Figure 8), however, with a significant decay of the coefficient of determination (R^2) from upstream to downstream, showing an increase in the process's nonlinearity along the river.

Table 4 - Rating curve equations for each stream gauge.

Stream gauge	**Rating curve†**
Cruzeirinho (N1)	$f(x) = 1.822x^{3.506}$
Mapuá (N2)	$f(x) = 33.252(x-0.42)^{1.844}$
Jaguaribe (N3)	$f(x) = 20.478(x-1.63)^{2.545}$
Monte Belizário (N4)	$f(x) = 21.039(x-0.64)^{2.076}$

† Where f(x) is the river discharge (m^3/s) and x is the water level (m) in the river.

Source: prepared by the author.

Figure 7 - Daily hydrological data from Jaguaribe river between 04/01/2022 and 21/06/2022: (a) boxplot of river discharge, (b) boxplot of river stage level, (c) river discharge, (d) river stage level.

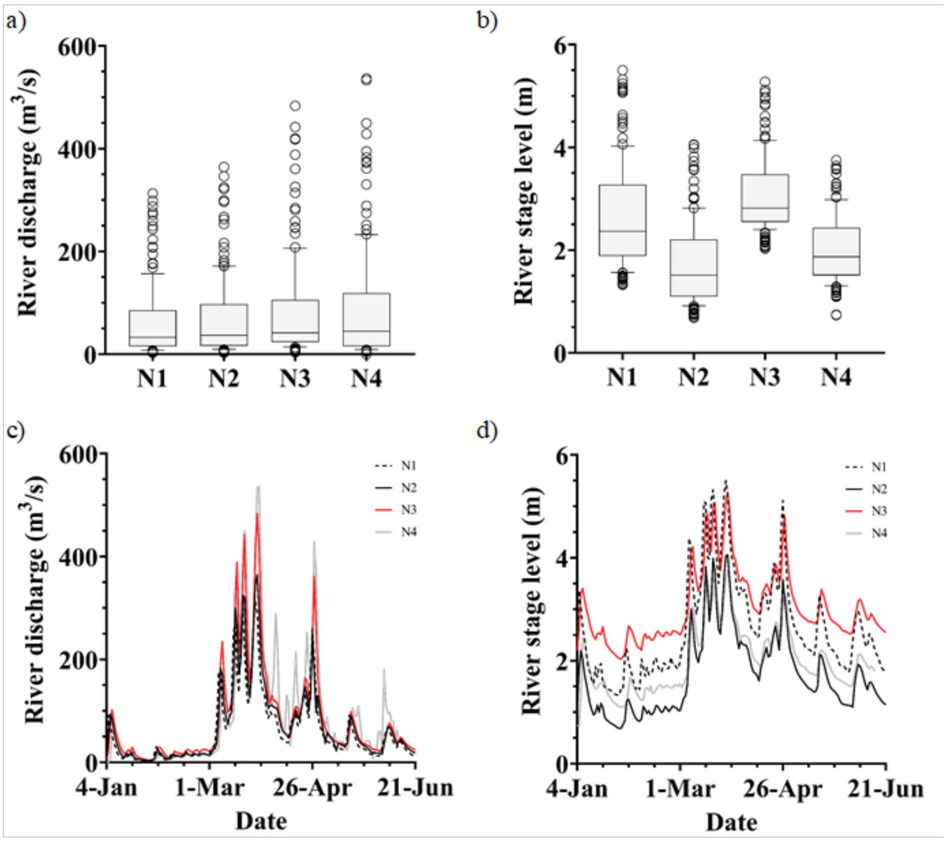

Source: prepared by the author.

Figure 8 - Linear regression between stream gauges.

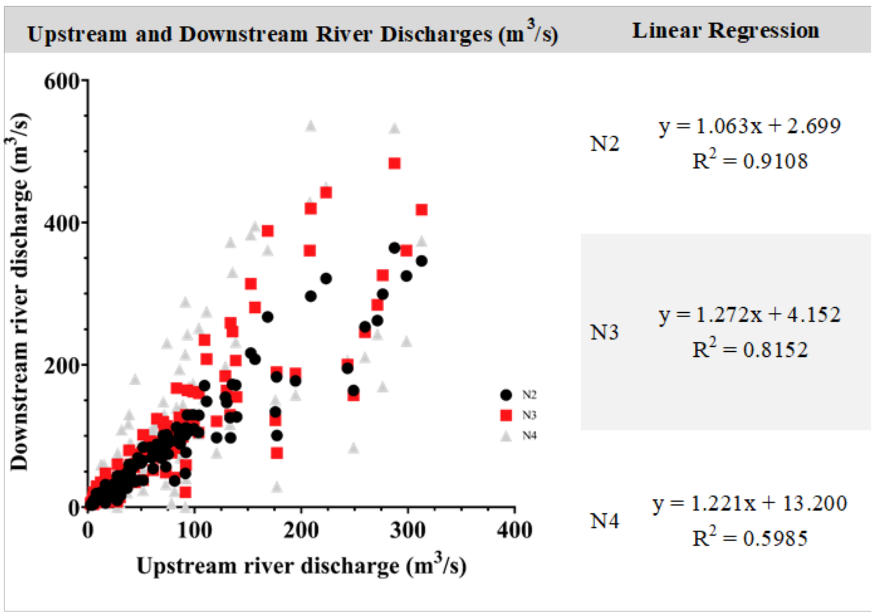

Source: prepared by the author.

The linear relationship between the associated flows was restricted to a threshold of approximately 100 m^3/s, above which there is hysteresis. In total, 19 runoff events were identified (refer to Table 5 for detailed information on the timing, precipitation, actual evapotranspiration, and water flux volumes associated with each event). Events 1, 7, 8, 13, 15, 16 and 18 presented a higher rainfall than the actual evapotranspiration, and only events 8 and 13 presented $P_{event} \geq 0.20$ S, which shows they had relevant surface flow in the incremental basin between the stream gauges (Figures 9a and 9b). Table 5 showed input flows greater than 10×10^6 m^3 mostly beside those seven events, with a maximum input flow of 41.8×10^6 m^3 in event 10, occurred in the middle of the rainy season. Event 10 also had the highest increase in flow volume between stream gauges for reaches 01 and 02 (16.67% and 32.70%, respectively), whereas event 11 had the maximum increase for reach 03. These increases in flow volume will be explained in the section below. River reaches 01 and 03 again showed a trend towards transmission losses throughout the events, while there was a trend towards gains in river reach 02 (Figure 9c). However, the 90th percentile interval has grown between adjacent stream gauges (Figure 9d).

Table 5 - Runoff events and hydrological data per river reach.

				Reach 1		Reach 2		Reach 3	
E†	Date (d/m)	P (mm)	ETa (mm)	I (10^6 m^3)	O (10^6 m^3)	I (10^6 m^3)	O (10^6 m^3)	I (10^6 m^3)	O (10^6 m^3)
1	5 – 8/1	16.4	11.7	7.9	8.1	8.1	8.8	8.8	5.3
2	17 – 19/1	0.8	7.8	1.8	1.7	1.7	2.5	2.5	1.7
3	31/1 – 2/2	0.0	8.0	2.6	2.2	2.2	2.5	2.5	1.8
4	8 – 11/2	1.1	12.4	1.4	1.3	1.3	1.9	1.9	1.3
5	16 – 18/2	1.6	8.3	1.9	1.5	1.5	2.2	2.2	1.4
6	24 – 27/2	0.3	12.4	1.8	1.5	1.5	2.2	2.2	1.4
7	6 – 8/3	17.0	8.9	15.3	15.8	15.8	20.3	20.3	13.2
8	15 – 16/3	52.0	4.5	23.9	25.9	25.9	33.5	33.5	31.2
9	19 – 20/3	0.8	4.5	25.8	28.1	28.1	38.2	38.2	38.8
10	26 – 28/3	2.5	8.9	27.0	31.5	31.5	41.8	41.8	46.4
11	3 – 6/4	4.1	12.6	8.6	9.6	9.6	11.2	11.2	24.9
12	17/4	3.9	4.2	7.9	8.7	8.7	9.3	9.3	18.5
13	21 – 23/4	38.0	8.4	11.5	12.7	12.7	14.2	14.2	21.7
14	26 – 27/4	2.4	4.2	22.4	21.9	21.9	31.2	31.2	37.0

15	16 – 18/5	11.5	7.3	7.9	7.8	7.8	8.5	8.5	9.2
16	4/6	25.7	2.0	3.8	3.1	3.1	3.0	3.0	15.6
17	6 – 7/6	1.4	2.0	6.0	6.0	6.0	6.6	6.6	8.4
18	11/6	19.2	2.0	2.5	3.0	3.0	3.6	3.6	5.4
19	12 – 14/6	4.3	4.0	3.5	3.9	3.9	4.2	4.2	3.9

Source: prepared by the author.

Figure 9 - Boxplot of hydrological data per event: (a) rainfall, (b) actual evapotranspiration, (c) river stage level, (d) river input volume.

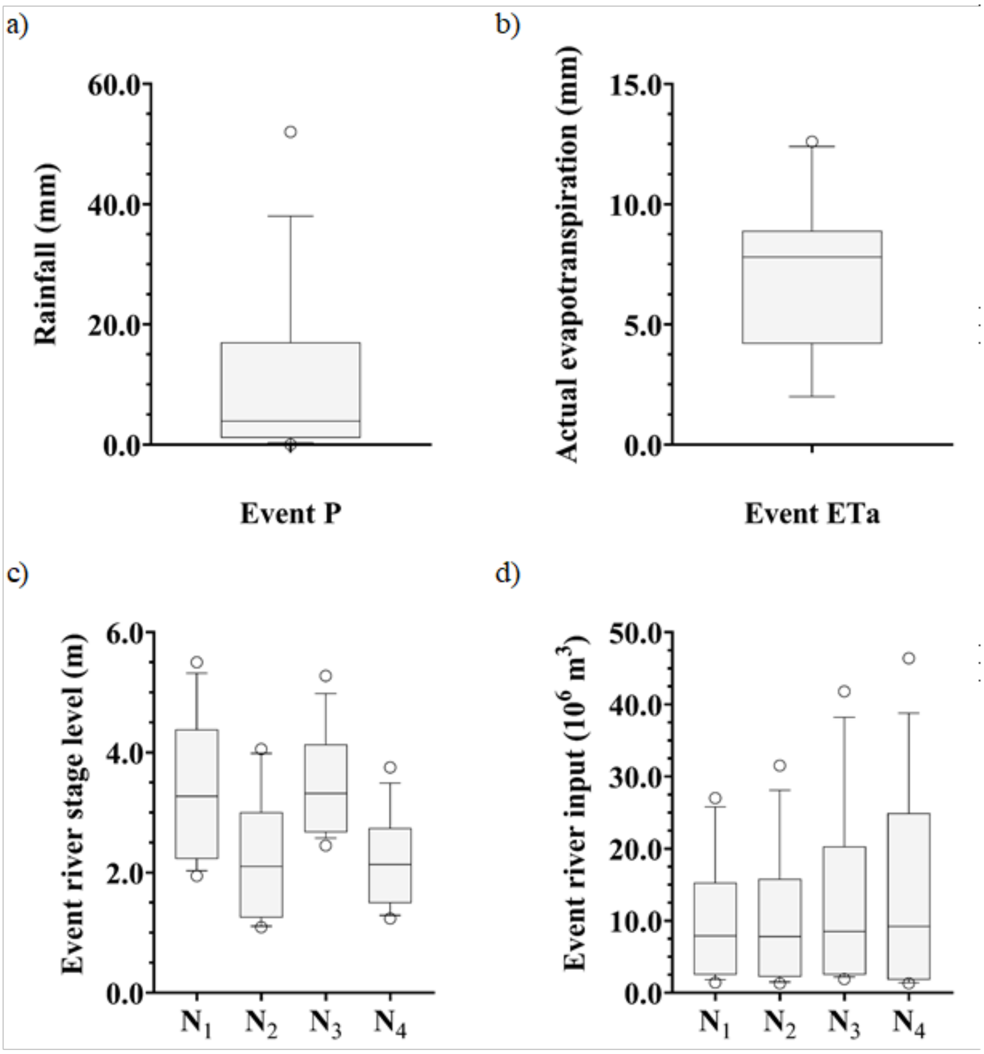

Source: prepared by the author.

Table 6 shows the quantification of the river-aquifer interaction for the 19 runoff events monitored in the Jaguaribe River during the rainy season of 2022. In most events, the values of π were below zero ($P_{event} < ETa_{event}$) (Figure 10a), showing reasonable water losses by evapotranspiration during the rainy season (between 4% and 22% of the water balance volume in the river reaches). Events with π greater than zero contributed 12% on average in the quantification of the river-aquifer interaction, but only events 8 and 13 generated sufficient surface flow in the direct drainage basin between stream gauges (μ > 0). The losses due to water extraction in the river or adjacent aquifer (∂) were significant only in river reach 01 (Table 6), with 25% on average of the water balance volume in it; on the other reaches, they are insignificant. Eight events with $\Omega \leq 0$ were identified in river reaches 01 and 03, mostly at the beginning of the rainy season, and had significant transmission losses ($-1.0 < R < 0.0$), losing 7.11 × to 10^6 m^3 of water volume throughout the river (event 7). No event in river reach 2 presented a negative water balance, with directional flow to the river up to 10.39×10^6 m^3 (event 10). Transmission gains in the other river reaches were 3.44×10^6 m^3 on average, with emphasis on events 11 and 16 in reach 03, where outflow in N4 gauge more than doubled in relation to inflow (close to events of intense rainfall or influence from river reach 02). Transmission gains will be discussed in the section below. Event 8 on reach 03 obtained a relevant superficial runoff in the incremental basin ($\mu > 6\%$ I^3_t), with R value not computed.

Although the median of R and Ω was above zero in all rivers reaches (2.10c and 2.10d, respectively), the gains in reaches 01 and 03 were not sufficient to compensate for the decrease in the river stage due to losses. The average water loss was 12% of inflow in reach 01 and 28% in reach 03 among the loss events. Reach 02 showed an average gain of 24.3% of the inflow among the gain events.

Table 6 - Transmission losses and gains for river reach.

	Reach 1‡						**Reach 2**						**Reach 3**					
E†	**O-I**	**π**	**∂**	**μ**	**Ω**	**R**	**O-I**	**π**	**∂**	**μ**	**Ω**	**R**	**O-I**	**π**	**∂**	**μ**	**Ω**	**R**
1	0.2	0.1	0.1	0.0	0.1	0.0	0.7	0.0	0.0	0.0	0.7	0.1	-3.5	0.0	0.0	0.0	-3.5	-0.4
2	-0.2	-0.1	0.0	0.0	-0.3	-0.1	0.9	0.0	0.0	0.0	0.8	0.5	-0.8	-0.1	0.0	0.0	-0.9	-0.3
3	-0.5	-0.1	0.0	0.0	-0.6	-0.2	0.4	0.0	0.0	0.0	0.3	0.2	-0.7	-0.1	0.0	0.0	-0.8	-0.3
4	-0.1	-0.1	0.1	0.0	-0.3	-0.1	0.6	-0.1	0.0	0.0	0.5	0.4	-0.6	-0.1	0.0	0.0	-0.7	-0.3
5	-0.4	-0.1	0.0	0.0	-0.5	-0.2	0.7	0.0	0.0	0.0	0.6	0.5	-0.7	0.0	0.0	0.0	-0.8	-0.3
6	-0.3	-0.1	0.1	0.0	-0.5	-0.2	0.7	-0.1	0.0	0.0	0.6	0.5	-0.8	-0.1	0.0	0.0	-0.9	-0.4
7	0.5	0.1	0.0	0.0	0.5	0.0	4.5	0.0	0.0	0.0	4.5	0.3	-7.1	0.1	0.0	0.0	-7.0	-0.4
8	2.0	0.6	0.0	1.4	4.0	0.1	7.7	0.2	0.0	1.0	9.0	0.3	-2.3	0.3	0.0	5.6	3.6	na§
9	2.3	0.0	0.0	0.0	2.2	0.1	10.1	0.0	0.0	0.0	10.1	0.4	0.6	0.0	0.0	0.0	0.6	0.0

10	4.5	-0.1	0.0	0.0	4.3	0.2	10.3	0.0	0.0	0.0	10.2	0.3	4.6	0.0	0.0	0.0	4.6	0.1
11	1.1	-0.1	0.1	0.0	0.9	0.1	1.6	0.0	0.0	0.0	1.5	0.2	13.7	-0.1	0.0	0.0	13.7	1.2
12	0.8	0.0	0.0	0.0	0.8	0.1	0.6	0.0	0.0	0.0	0.6	0.1	9.2	0.0	0.0	0.0	9.2	1.0
13	1.2	0.4	0.0	0.0	1.5	0.1	1.5	0.2	0.0	0.2	1.8	0.1	7.6	0.2	0.0	1.0	8.7	0.5
14	-0.5	0.0	0.0	0.0	-0.6	0.0	9.3	0.0	0.0	0.0	9.2	0.4	5.9	0.0	0.0	0.0	5.9	0.2
15	-0.2	0.1	0.0	0.0	-0.2	0.0	0.7	0.0	0.0	0.0	0.7	0.1	0.7	0.0	0.0	0.0	0.7	0.1
16	-0.7	0.3	0.0	0.0	-0.5	-0.2	-0.1	0.1	0.0	0.0	0.0	0.0	12.6	0.2	0.0	0.0	12.8	4.2
17	0.0	0.0	0.0	0.0	0.0	0.0	0.6	0.0	0.0	0.0	0.6	0.1	1.7	0.0	0.0	0.0	1.7	0.3
18	0.5	0.2	0.0	0.0	0.7	0.2	0.5	0.1	0.0	0.0	0.6	0.2	1.9	0.1	0.0	0.0	2.0	0.5
19	0.5	0.0	0.0	0.0	0.4	0.1	0.3	0.0	0.0	0.0	0.2	0.1	-0.3	0.0	0.0	0.0	-0.3	-0.1

† Event.

‡ Values for river reach in 10^6 m^3.

§ Not applicable.

Note: O-I is the difference between outflow and inflow, π is the vertical water balance between rainfall and actual evapotranspiration, ∂ is the water extraction volume for demand supply, μ is the lateral inflow in the drainage area between stream gauges, Ω is the river-aquifer water balance, R is the transmission loss rate.

Source: prepared by the author.

Figure 10 - Boxplot of: (a) river reach precipitation/evaporation, (b) outflow – inflow, (c) transmission loss rate, (d) river-aquifer water balance.

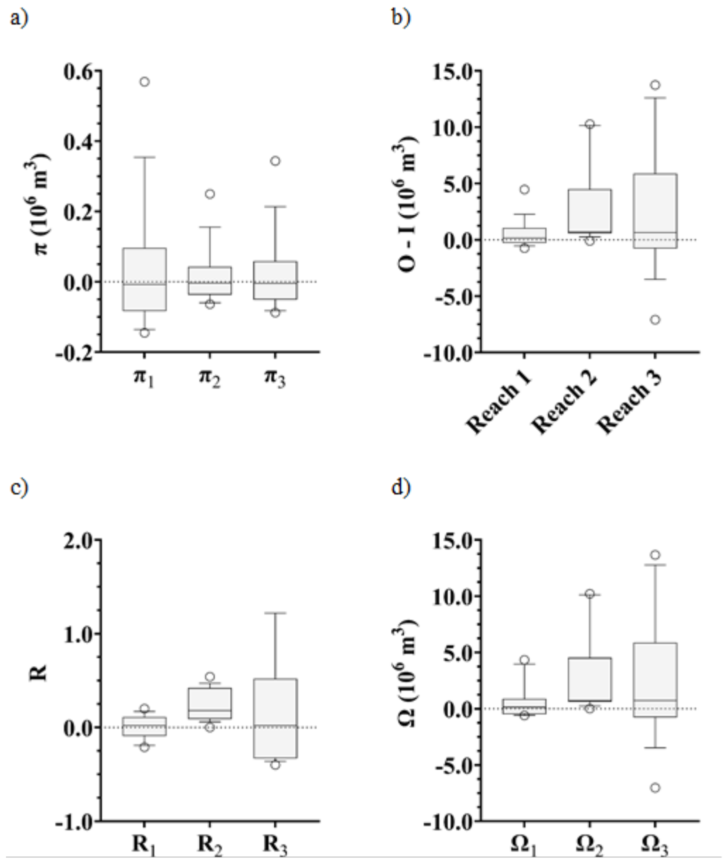

Source: prepared by the author.

Figures 11a and 11b show the occurrence of transmission losses and gains even at the beginning of the rainy season (rainfall ≤ 10 mm and ETa ≤ 12.5 mm). A trend was observed where higher river stage levels and flow rates in the reaches resulted in increased rates of transmission gains downstream (R > 0.0). This finding highlights the more significant influence of river flow on transmission losses compared to seasonality. Water loss was observed mainly for river stage levels greater than 2 meters and discharges smaller than 200 m^3/s. (Figures 11c and 11d).

Figure 11 - Transmission loss rate per event compared to: (a) rainfall, (b) actual evapotranspiration, (c) river stage level, (d) river discharge.

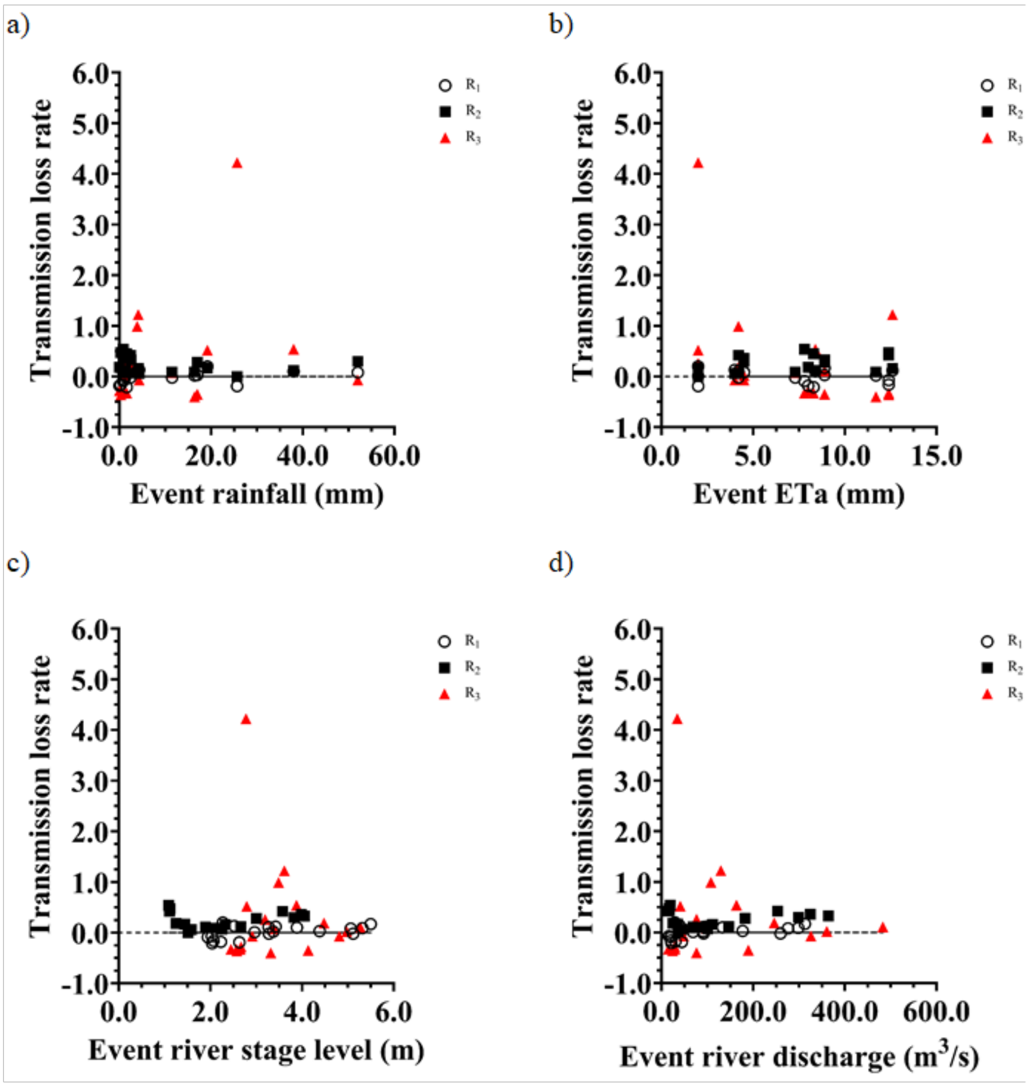

Source: prepared by the author.

2.4 Discussion

2.4.1 Hydrological analysis

The quantification of the river-aquifer interaction was determined through the analysis of extensive and daily hydrological measurements collected from four stream gauges along the 71 km stretch of the Jaguaribe River. The measured daily flows showed a linear behaviour (Figure 11), similar to that observed by (Zhou; Cartwright, 2021) in an intermittent river adjacent to an alluvium and in a semiarid region. Above 100 m^3/s, there is hysteresis and an increase in downstream nonlinearity in the study site. This complex hydrological phenomenon results from the nonlinear temporal response of river flow to the contributions of subsurface flow, which influence the water balance (Ω) itself upstream from the river reaches, and rainfall (Thoms; Sheldon, 2000). Satellite images showed that transmission losses did not occur in the floodplain, but mostly on the riverbed adjacent to the alluvial plain, as also observed by Costa *et al.* (2013) on another reach of the Middle Jaguaribe river. Since direct infiltration is small in the semi-arid region of Ceará (Kreis *et al.*, 2020), which does not favour a significant elevation of the groundwater adjacent to the river, an increase in transient flow from the aquifer to the river is not expected.

Here, it is likely that part of the transmission losses in the river by infiltration, the main source of aquifer recharge in dry regions (Izady *et al.*, 2014; Sophocleous, 2002), flows parallel to the Jaguaribe river (hyporheic flow), and returns as a contribution (baseflow) to the surface flow in downstream monitored gauges (N2 to N4) when there is an elevation of the adjacent groundwater because of rainfall in the region (Conant *et al.*, 2019; Kreis *et al.*, 2020). The surface flow will receive the contribution of the direct rainfall volume on the analysed river reaches (Zhou; Cartwright, 2021), although the daily ETa is higher than the rainfall in part of the first half of 2022.

The average water loss by infiltration in reaches 01 and 03 is in accordance with the values presented in the works of Araújo and Ribeiro (1996), Costa *et al.* (2013), Toledo *et al.* (2018), Rêgo (2021), and below the values estimated from the results of Knighton and Nanson (1994), Lange (2005), and Hughes (2019). Average water gain in the reaches is close to the 69.23% measured in another reach of the Jaguaribe River analysed by Costa *et al.* (2013). The losses due to infiltration and downstream gains by hyporheic flow confirm the results obtained by Toledo *et al.* (2018), which showed the influent/effluent character of the Jaguaribe River, something previously verified by Costa *et al.* (2013), and may explain the data measured in the monitored reaches. This characterization is in accordance with the approximately parallel arrangement between the river reaches and the alluvial plain (Figure 2), a geomorphological configuration that favours the occurrence of influent/effluent rivers.

Transmission losses and gains data showed linear behaviour (on a log-log scale), according to Figure 12, both increasing their values for higher inflow rates in the river reaches. This behaviour of transmission losses was also seen by Batlle-Aguilar and Cook (2012), Costa *et al.* (2013), Hughes (2019), Knighton and Nanson (1994), Lange (2005), Mujere *et al.* (2022), Schoener (2017), Schreiner-McGraw, Ajami and Vivoni (2019), and Toledo *et al.* (2018). According to Moriasi *et al.* (2015), R^2 and Nash Sutcliffe's efficiency values for the Transmission Loss x Inflow relation were very good ($R^2 > 0.85$ and NSE > 0.80), including a higher R^2 value than that presented by (Mujere *et al.*, 2022) in their linear regression (Transmission Losses x Inflow) ($R^2 = 0.726$), while the R^2 and NSE values for the Transmission Gains x Inflow relation were satisfactory ($R^2 > 0.60$ and NSE > 0.50).

The linear regression equations (log-log scale) for an estimate of the initial order of magnitude of the transmission losses and gains in the river-aquifer interaction in a dry region (event-based analysis) and on a basin-scale are:

$$V_{Losses} = 0.3709 \cdot V_{inflow} - 0.2718 \qquad (2.11)$$

$$V_{Gains} = 0.1664 \cdot V_{inflow} - 0.0045 \qquad (2.12)$$

Where: V_{Losses} - transmission losses volume (hm^3); V_{Gains} - transmission gains volume (hm^3); V_{inflow} - Inflow into the river reach (hm^3). The above equations are empirical and applicable to rivers in scenarios similar to that of the Middle Jaguaribe, with an inflow between 0.014 and 46.36 hm^3. Equation 2.11 preferably applies to the following conditions: rainfall < 20.0 mm; 5.0 < ETa ≤ 12.50 mm; 2.0 < River stage level ≤ 4.5 m; river discharge < 200 m^3/s. In these conditions, there are also transmission gains, and it is possible to use equation 2.12. Only this equation applies to the following conditions: rainfall ≥ 20 mm; ETa ≤ 5 mm; river stage level ≤ 2 m; river discharge ≥ 200 m^3/s.

An evaluation of equations 2.11 and 2.12 was performed with data collected in recent studies, according to Figure 13. The data on transmission losses were close to the perfect-fit of equation 2.11: R^2 value almost very good (≈ 0.85), according to Moriasi *et al.* (2015). On the other hand, the transmission gains showed significant variability, with equation 2.12 presenting a lower R^2 value (≈ 0.47). This variability can be partially explained by the dependence of hyporheic flow in relation to the transport and deposition of sediments in the river (Maia; Bezerra, 2020) and to the depth of the channel in the alluvial plain (Conant *et al.*, 2019; Goodrich *et al.*, 2018), which is related to evaporation in the river (Hughes, 2019). Nevertheless, equation 2.12 should not be ruled out as the first estimate of the order of magnitude of transmission gains in places without hydrological monitoring, a common case in dry regions (Costa *et al.*, 2013).

Figure 12 - Hydrological data compared: (a) input flow and transmission losses in linear regression with R^2 value, (b) measured losses and simulated losses with NSE value, (c) input flow and transmission gains in simple linear regression with R^2 value, (d) measured gains and simulated gains with NSE value.

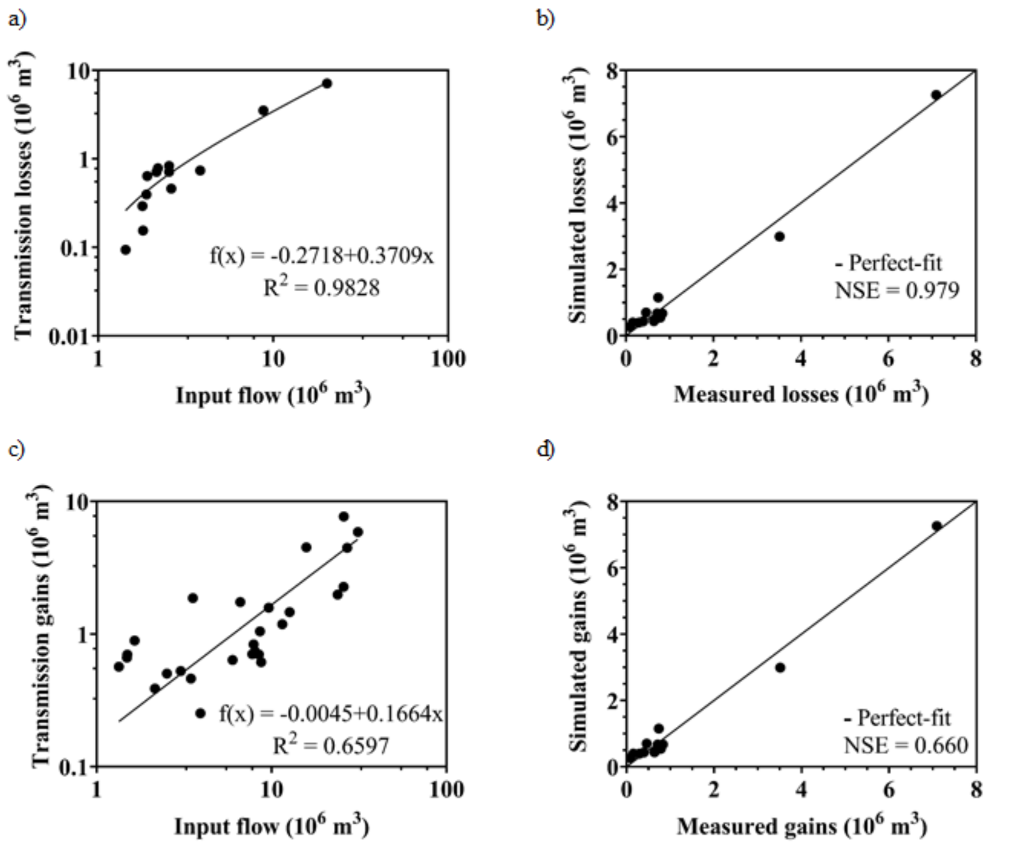

Source: prepared by the author.

Figure 13 - Relationship between the empirical equations proposed and data measured in the field or collected in recent research: (a) comparison of equation 2.10 with transmission losses data, (b) comparison of equation 2.11 with transmission gains data.

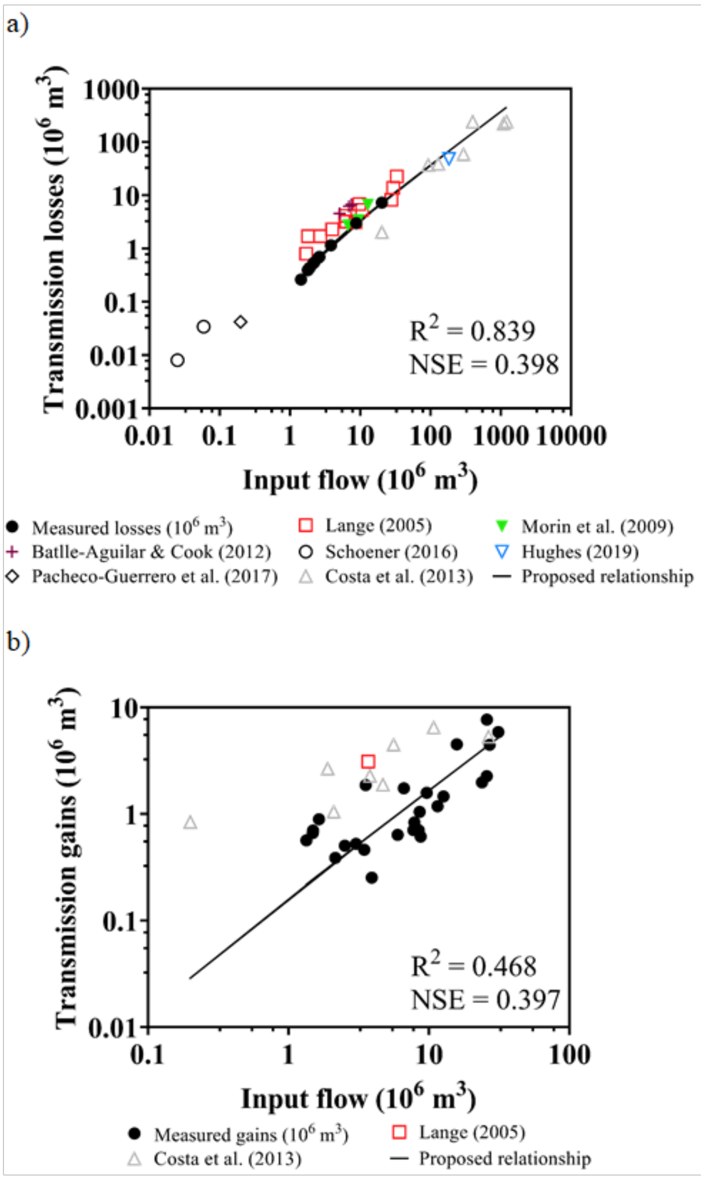

Source: prepared by the author.

2.4.2 Synthesis: Conceptual model of river-aquifer interaction

The structural lineaments and shear zones (Figure 2) are structural controls of the rectilinear path interspersed with few sinuous stretches in the Middle Jaguaribe, of the direction (NE-SW) of the flow in the river and in the drainage basin, and of the accumulation of Quaternary sediments in the river valley (Maia; Bezerra, 2020). The width-depth ratio of the studied river (<20.50m) is low (Ruben, 2021), with the longitudinal valley approximately with the same slope as the Jaguaribe river, and the lateral valley with a small slope. These characteristics classify the river as a mixed flow system, alternating the preponderance between the baseflow component (groundwater flow perpendicular to the river cross-section) and the hyporheic flow component (groundwater flow parallel to the river flow direction in the Middle Jaguaribe) (Sophocleous, 2002). This component is one cause for transmission gains and for the increase in nonlinearity downstream of the first stream gauge (N1).

The water flow direction and rate (volume/time) in the system depends on the difference in water level between the aquifer and the river (hydraulic gradient) and on the hydraulic conductivity between the riverbed and the associated alluvium. The hydraulic gradient becomes positive during the rainfall season (flow direction: aquifer to river), which is concentrated in the first six months of the year (refer to precipitation values during the 19 events in Table 5). This results in a rapid rise of the groundwater table, contributing to surface flow through both baseflow and hyporheic flow components. Additionally, there is infiltration of surface water into the aquifer. In this sense, the release of water flux from the Orós reservoir, measured at the N1 gauge, also enhanced river-aquifer connectivity. This is evidenced by the reduction in transmission losses over time during the 19 flood events, attributed to the rise in groundwater levels. In the absence of rainfall, more frequent in a semiarid region, the connectivity between the river and the aquifer is disrupted as the groundwater level declines below the river cross-section (Costa *et al.*, 2013), with vertical groundwater flow downward (vertical infiltration). Most of the water volume contributing to the fractured aquifer results from indirect infiltration, added to the rapidly vertically infiltrated volume, something already indicated by (Schreiner-McGraw; Ajami; Vivoni, 2019), and validated for the Ceará semi-arid region by (Kreis *et al.*, 2020).

In both periods (rainy and dry), in the presence of operating wells adjacent to the river, the groundwater flow is induced in their direction, with a preferential path through the fractures of the crystalline basement (Alves *et al.*, 2018; Beetle-Moorcroft; Shanafield; Singha, 2021; Lachassagne; Dewandel; Wyns, 2021). Since the hydraulic conductivity of the riverbed is 10^4 times greater than alluvium, there is a significant preferential flow in the river-aquifer direction under the influence of a negative hydraulic gradient (Conant *et al.*, 2019; Gnanachandrasamy *et al.*, 2019). Figure 14 shows the proposed conceptual model of groundwater flow for the study site in Middle

Jaguaribe.

According to the quantification of the river-aquifer interaction in the river reaches (Table 6), the average water balance in reach 01 was 0.6 hm^3, 2.8 hm^3 at reach 02 and 2.7 hm^3 at reach 03. These values are close to the values found in research conducted in dry regions: 29.3 hm^3 (Hughes, 2019), 2.41 hm^3 (Mengistu *et al.*, 2019), 3.96 hm^3 (Cetina *et al.*, 2020) and 62.4 hm^3 (Karlović *et al.*, 2021).

Transmission gains ($R > 0$) were influenced by intense rainfall events (>20 mm/d), contrary to what was verified by Schreiner-McGraw, Ajami and Vivoni (2019). They found that less frequent and more intense rainfall (>25 mm/d) is the main responsible for transmission losses in rivers, potentially contributing to the aquifer recharge. Here, it was found that at the beginning of the rainy season, with less intense rainfall (< 10 mm/d), there is a predominance of transmission losses. These seem to depend more specifically on the river volume and the water level in the main channel. A potential explanation for this phenomenon from the proposed conceptual model and the water balance of Table 6 is given as follows:

(1) A clogging layer is formed in the alluvial plain throughout the dry period in the Middle Jaguaribe (July to December).

(2) With the beginning of the rainy season (January to June), this layer is removed with the river flow (Lange, 2005). The first runoff event has precisely a higher rainfall than the others, surpassed only in March. Furthermore, in river reach 1, the initial runoff event exhibits small transmission losses (Table 6).

(3) The removal of the clogging layer enables vertical flow through infiltration from the riverbed into the vadose zone and the aquifer (Figure 14). Table 6 shows $R < 0$ in reach 01 from the second to the sixth events, while in reach 03 the values of $R < 0$ occur in the first eight events. Reach 02, on the other hand, has $R > 0$ throughout the rainy season. It can be assumed that the gain by hyporheic flow, from the loss in reach 01, and by the baseflow, from the increase of the groundwater level at the time of the rains, compensated the losses in the reach.

(4) After the losses in reaches 01 and 03 in the first events, the contribution to river flow by the elevation of the groundwater table (baseflow) and hyporheic flow

overlaps the transmission losses, besides the contribution of the directly rainfall volume on the reaches.

(5) In the events 14 to 16 (April and May) of reach 01, there are transmission losses. Since the peak of the actual evaporation in the region is from March to May, it is assumed that the rainfall and baseflow volumes are not sufficient to overlap the losses by infiltration from the river to the aquifer and the evapotranspiration in this reach. Hughes's work (2019) corroborates this assumption, having found transmission losses due to evapotranspiration between 0.8 and 19.1% of the river volume in different rivers in South Africa.

(6) In the other months, after the last runoff event in June, there will again be the formation of the clogging layer in the alluvial plain throughout the dry months, until the rainy season returns on the study site.

Figure 14 - Conceptual model for river-aquifer interaction in Middle Jaguaribe: (a) river basin, (b) dry season, (c) profile view in dry season, (d) rainy season, (e) rainy season with well in the adjacent alluvium.

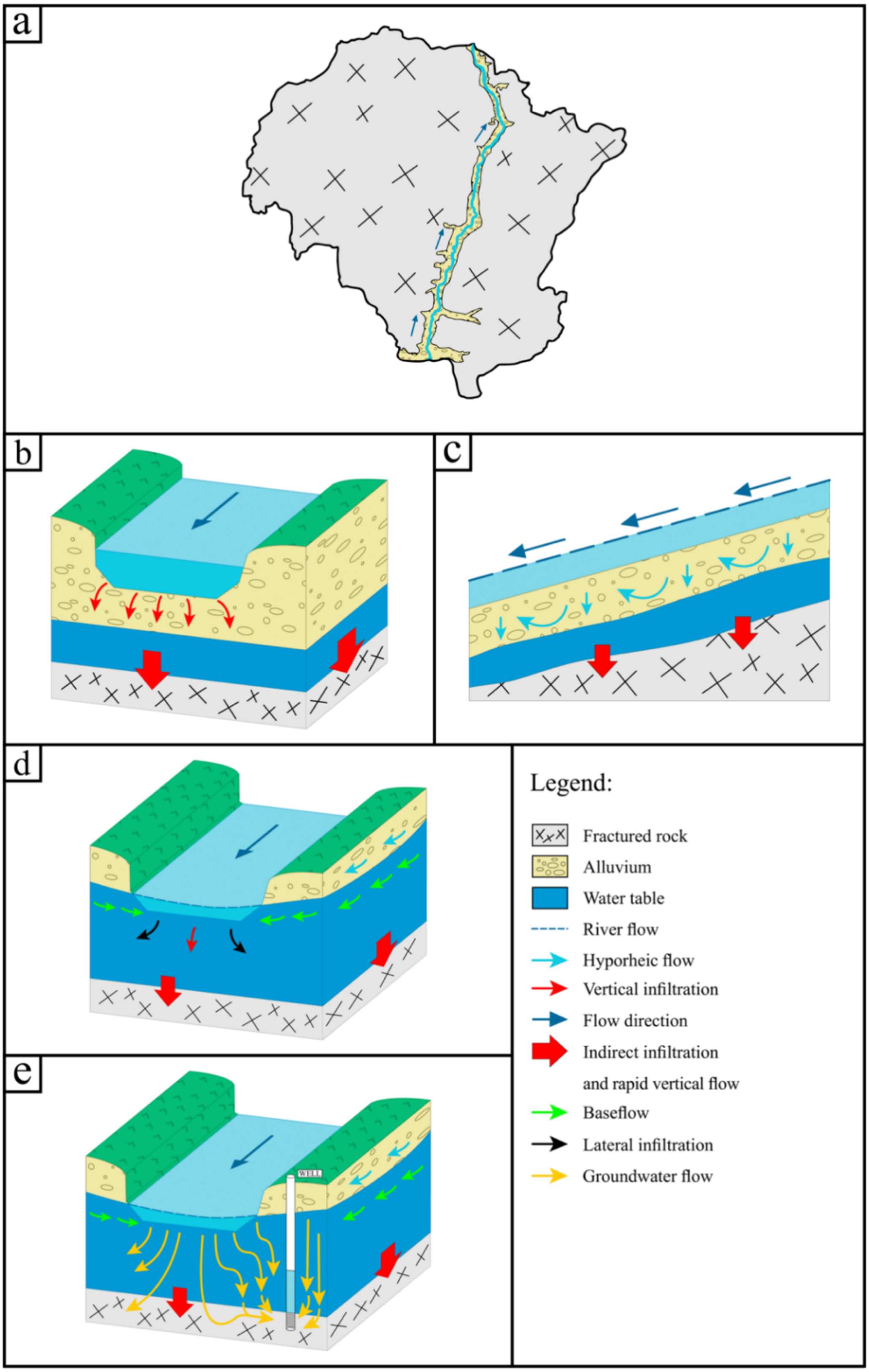

Source: prepared by the author.

2.5 Conclusions

This article developed a conceptual model of the river-aquifer interaction in a dry region on a basin-scale. The model combined daily data from hydrological monitoring in four stream gauges in three contiguous river reaches (71 km) with data from multispectral satellite images. The proposed description of the mechanisms of transmission losses and gains in the river can be used to improve water resources management and to further elaborate numerical models of the river-aquifer interactions on the same scale and in other dry regions, allowing to interpret more deeply the groundwater flows and the spatio-temporal availability of groundwater volume.

The hydrological monitoring in the field lasted 168 days, with no episodes of null flow in the reaches. No transmission losses were identified on the floodplain. However, there was an increasing linear behaviour (log-log scale) between the inflow and outflow in the reaches ($0.5985 \leq R^2 \leq 0.9108$) up to 100 m^3/s, with events with transmission gains occurring after rainfall events; above this threshold, there was an increase in downstream nonlinearity in the river. Increases in peak flow between the river reaches of 16.51% (N1-N2), 32.58% (N2-N3) and 11.05% (N3-N4) were also observed.

The quantification of the river-aquifer interaction was computed in 19 runoff events lasting 1 day on each river reach. In most events, the actual evapotranspiration was higher than rainfall, and losses for demand supply in the adjacent aquifer were most of the time insignificant. Eight transmission losses events were identified in reaches 01 and 03, while in reach 02 the water balance was greater than zero in all events. The average loss was 12% of inflow in reach 01 and 28% in reach 03. Reach 02 showed an average gain of 24.3% of inflow. The water gains in reach 01 and 03 were 10% and 34% of inflow, respectively. Transmission losses already occurred at the beginning of the rainy season (rainfall ≤ 10 mm/d), being mainly influenced by the river volume and its water level. Transmission gains were preponderant after intense rainfall events (> 20 mm/d). The increasing linear behaviour (log-log scale) was also identified between the transmission losses/gains data with river inflow. Simplified equations were calibrated to estimate the order of magnitude of transmission losses ($R^2 > 0.85$ and NSE > 0.80) and gains ($R^2 > 0.60$ and NSE > 0.50). The transmission loss equation was validated for rivers in similar regions ($R^2 \approx 0.85$) with hydrological data from recent research. The transmission gain equation presented a lower value ($R^2 \approx 0.47$), but can serve as a first estimation of the order of magnitude of the gains for rivers not monitored in drylands.

The conceptual model of the river-aquifer interactions suggests an explanation of the data obtained from the daily hydrological monitoring of runoff events. The dry period in the region extends from July to December, with the water table below the river channel, and with the formation of a clogging layer in the riverbed, removed with rains in January and February. These rains raise the groundwater level, so that the river flow receives a contribution of groundwater as hyporheic flow and baseflow, besides the rainfall volume over the river. The alluvial aquifer receives recharging by infiltration in the riverbed, while the fractured aquifer is supplied from indirect infiltration. Hydraulic conductivity of the riverbed was 10^4 times greater than alluvium, showing a significant water flow through infiltration under the influence of a negative hydraulic gradient. The average water balance at reach 01 was 0.6 hm^3, 2.8 hm^3 at reach 02 and 2.7 hm^3 at reach 03, similar to research data in dry regions.

However, uncertainty, which arises from experimental hydrological analysis, should always be considered prior to the use of these findings for water resources management. This uncertainty can be explored using numerical hydrological modelling by evaluating parameter variation or different model structures, having as start point the formulated conceptual model, for example. On the other hand, uncertainty can be reduced in later work through a comprehensive monitoring of the groundwater level in the region, similar to the daily measurements performed in the studied river. In addition, the understanding of the flow components will be further developed with a more detailed characterization of the geometry of the alluvial plain, and of the variation of its hydraulic parameters in the incremental basin of the river reaches.

2.6 Funding

The present study was supported through the National Council for Scientific and Technological Development – CNPq and the Ceará State Research Foundation – FUNCAP [Research Grants PNE-0112-00042.01.00/16].

3 PARSIMONIOUS MODELLING OF DRYLAND, DATA-SCARCE RIVER-AQUIFER DYNAMICS, CONSIDERING OVERLOOKED RIVER AND AQUIFER PROCESSES[2]

3.1 Introduction

A recent study on the frequency of drought days amidst climate change has identified that global land areas are projected to experience prolonged periods of abnormal water levels in both low-flow and high-flow seasons over the coming decades, in comparison to historical data from 1971 to 2005 (Satoh *et al.*, 2022). Warmer climate conditions are expected to reduce precipitation and water discharge in these regions, whereas evapotranspiration is predicted to increase (Boulton *et al.*, 2017). Hydrological alterations in streamflow, surface runoff, and human-induced activities, such as sectoral water use, may raise concerns about water security, particularly in dryland regions (Quichimbo *et al.*, 2023). In areas of low precipitation, surface water plays an important role in aquifer recharge through channel seepage and may be interconnected with groundwater, depending on climatological and hydrogeological circumstances (Liu *et al.*, 2022; Ntona *et al.*, 2022; Sophocleous, 2002). Evaluating the water interchange between surface water and groundwater is, therefore, critical for the efficiency of water resources management policies (Zhou *et al.*, 2022).

Various numerical models have been developed over the last few decades to simulate river-aquifer dynamics, as their behavior affects agricultural, industrial, and domestic purposes (Chen *et al.*, 2020). These models have limitations, such as the high quantity of data required, often unavailable in dryland regions, and uncertainty in the computed streamflow related to input data (Kumar *et al.*, 2024). In this sense, Pacheco-Guerrero *et al.* (2017) coupled hydrological and hydraulic models to compute river losses to the aquifer in the Walnut Gulch Watershed using LiDAR data to estimate channel geometry. They used several programs to execute the model (4-5 hours to complete), which required much data besides the DEM, such as Manning's roughness

---

[2] A paper based on the content of this chapter has been published in *Modeling Earth Systems and Environment* as Toné, A. J. A., Costa, A. C., Gonçalves Barros, M. U. & Lima Neto, I. E. (2025). Streamflow prediction based on data-scarce river-aquifer dynamics estimated by a simplified modelling framework in a dryland catchment. *Modeling Earth Systems and Environment*, *11*(282).

and vegetation cover. Kim *et al.* (2022) developed a riverbed/bank storage model to compute river-aquifer dynamics over a 1,116 km reach of Cooper Creek in Australia, with a daily time step, considering processes such as river loss/gain to the aquifer, river rainfall/evaporation, and rainfall to surface runoff transformation. However, the model struggled to simulate river behavior under dry conditions, probably due to the absence of river gauges at the entrance of tributaries to the main channel, which is common in long reaches.

Di Ciacca *et al.* (2023) proposed an approach to compute hourly surface water losses in the Selwyn River aquifer, New Zealand, which only requires a river gauge station to develop a discharge stage rating curve and high-resolution satellite imagery. They derived the average river loss by dividing the river discharge by the wetted river length (from the river gauging station to the drying front site). However, it may be difficult in dryland regions to find a stable cross-section to be monitored continuously to develop a rating curve because processes such as flashy streamflow and sediment deposition affecting channel geometry (Grabowski *et al.*, 2022). Regarding machine learning models, De Sousa *et al.* (2024) aimed to predict daily streamflow in a Brazilian catchment spanning the Savanna and Amazon biomes, characterized by a limited river gauge network. The non-stationarity of hydrological processes in these regions is particularly complex because of human exploitation of groundwater and electricity generation in hydroelectric plants. When accurate rainfall data were available, the k-nearest neighbor, support vector machine, and artificial neural network models demonstrated good predictive performances. Nevertheless, these models are more challenging to interpret and may yield results that lack consistency. Moreover, they often require large datasets for training, which may not be available in data-scarce catchments (Xu; Liang, 2021).

Although numerical models constitute reliable approaches to understanding river-aquifer water fluxes, current state-of-the-art challenges still require reliable answers. Two of them are particularly important for dryland regions: (a) high dependency on and frequency of field measurements, and (b) a parsimonious approach to favor calibration on a daily time step, which is critical for efficient management policies and river operations (Kim *et al.*, 2022; Ntona *et al.*, 2022). Moreover, water security depends on an adequate representation of the hydrological processes involved in river-aquifer dynamics, such as the behavior of groundwater levels in response to rainfall, hyporheic flow to the river, and lateral tributary inflow (sub-catchment runoff to the river). These processes represent a research gap, as they are often neglected in river-aquifer studies (Hussain; Wu; Shih, 2022; Mujere *et al.*, 2022).

The present study proposes a numerical model to estimate the streamflow in dryland regions. This model can mimic river-aquifer dynamics by addressing the above-mentioned challenges, i.e., modelling data-scarce environments and representing the often-overlooked processes involved in groundwater flow response to rainfall. Additionally, this study contributes to improving the understanding of the processes involved in river-aquifer dynamics, as it offers a more accurate water balance at the river-aquifer scale, which is crucial for adequate daily water management of dryland-based communities.

The study's research objectives are

(1) To develop a parsimonious numerical model capable of simulating the processes involved in river-aquifer dynamics in data-scarce regions at temporal and spatial scales that are important for water management.

(2) To provide insight into the overlooked processes related to river losses and gains in large dryland rivers, such as lateral tributary inflow and hyporheic flow.

(3) To compute groundwater levels in an unconfined aquifer using daily rainfall and streamflow data measurements.

3.2 Methods

3.2.1 Study site

The study site is a mixed flow system, losing/gaining reach of the Middle Jaguaribe River in Ceará, NE-Brazil (Figure 1). The Köppen classification system characterizes the region as having a hot, semi-arid climate with a distinct contrast between the dry and rainy seasons. The rainy season (January to May) accounts for up to 80% of the annual rainfall, ranging from 500 to 1,000 mm (De Araújo; Medeiros, 2013). On the other hand, the dry season is characterized by a high atmospheric water deficit, with evaporation rates exceeding rainfall by up to four times throughout the year. These climatic conditions, with rainfall concentrated over a few days, reaching up to 150 mm/day, result in periodic, intense dry periods, and occasional floods (De Araújo; Medeiros, 2013; Rabelo *et al.*, 2021; Raulino; Silveira; Lima Neto, 2021).

The rainfall regime, combined with soils over crystalline rock formations, generates intermittent rivers, with most river discharge occurring within three months. To mitigate the water vulnerability caused by limited groundwater availability in the crystalline basement and the temporal variability of river flow, reservoirs were constructed to store water during the rainy season, ensuring water supply during dry periods (Campos, 2015; Kreis *et al.*, 2020). In this context, the Jaguaribe River plays a crucial role in water resource management and serves as a key component of the integration system with major reservoirs in Ceará, including the Castanhão Reservoir, which is the largest non-hydropower dam in Latin America. This integration significantly enhances the water availability and supports regional economic development (Medeiros et al. 2022).

The study river drains an area of 2,898 km² and extends for a total length of 70.91 km, divided into three river reaches between gauging stations (N1, N2, N3, and N4): N1 to N2 (34.72 km), N2 to N3 (15.23 km), and N3 to N4 (20.96 km). The river slopes range from 0.03 m/km between N2 and N3 to 0.94 m/km between N3 and N4, with the reach between N1 and N2 exhibiting an intermediate value of 0.59 m/km (CPRM 2014, 2015). The studied river primarily relies on contributions at its entrance (N1 gauge) from the Salgado River and water release from the Orós Reservoir, which has a total drainage area of 38,000 km².

Unconfined aquifers predominantly underlie the simulated river reaches, which are part of an alluvial system with a maximum depth of 30 m and a mean grain size of 0.90 mm. These aquifers connect hydraulically to the underlying crystalline rock formations, which do not support significant regional groundwater flow (Kreis *et al.*, 2020; Pinheiro *et al.*, 2023; Wiegand, 2009). Preferential flow from the river to the aquifer occurs in the occurrence of a negative hydraulic gradient, as the hydraulic conductivity of the riverbed is approximately 10^4 times greater than that of the surrounding alluvium (8.64 mm/d) (Palheta et al. 2019).

3.2.2 Datasets

A preliminary description of the proposed numerical model must first be made such that all the data used can be clearly described. A detailed description of its parts is provided in the next section. A numerical model for the river reach was developed based on the conceptual model presented in the Supplementary Material (Figure S3.1).

To ensure a parsimonious model, two preliminary steps were undertaken: (1) the study site was divided into three sub-catchments (Figure S3.2); and (2) a triangular cross-sectional area was assumed for the Jaguaribe River, consistent with previous approaches in the river (Costa *et al.*, 2012).

Subsequently, to calculate the streamflow, the first step involved estimating (a) rainfall and evaporation fluxes within the riverscape. Next, (b) the lateral contributions from sub-catchments to the river were determined using the Soil Conservation Service (SCS) Curve Number (CN) method, which has demonstrated a low level of uncertainty in watershed modelling (Deshpande; Dhorde, 2024; Sahu; Shwetha; Dwarakish, 2023). Then, (c) stream-aquifer interaction fluxes were computed using Darcy's law and a sub-model to estimate river losses through seepage. These predicted values are then summed with those from Steps (a) and (b). Finally, streamflow routing was applied using a nonlinear Muskingum-Cunge method to predict the discharge at the downstream end of the river (Figure S3.3).

Because stream-aquifer fluxes depend on the water table, step (c) estimates it using a Dupuit flow system. If the head difference is positive, the river and groundwater are hydraulically connected, and the saturated zone beneath the stream may recharge from or discharge to the river. Conversely, if the head difference is negative, river losses occur in unsaturated or saturated zones.

In light of the scarcity of data, which can significantly increase prediction uncertainty (Cirilo *et al.*, 2020), the nonlinear Muskingum-Cunge river routing model requires a small number of parameters to be applied (Table S3.1), all of which are relatively easy to obtain in poorly gauged catchments. The initial conditions for the streamflow model included (a) river inflow and water level, as measured at the study site, and (b) hydraulic conductivity of the riverbed and alluvium, as well as aquifer width and top cross-sectional width, which were assumed to be constant values for the sake of model parsimony, as outlined below.

As mentioned above, the geometric shape of the river cross section is triangular for practical purposes. Once the river stage head was measured (see below), geometric parameters (area, perimeter, top width, and hydraulic radius) were derived from this shape. The top width of cross section was assumed to be constant when no flow was beyond the main channel. The Copernicus GLO-30 digital elevation model was used in the QGIS raster analysis tool to determine the channel length, slope, and sub-catchment area. The curve number of the sub-catchments was derived from raster data type of land use in Brazil provided by ANA (2018), incorporating a type 2 precondition concerning soil moisture. The hydraulic conductivity of the riverbed was estimated using Hazen's method and the riverbed grain size in the study area provided by Wiegand (2009). The hydraulic conductivity of the alluvium and aquifer width were collected from hydrogeological surveys provided by CPRM.

The inflow and river stages were measured daily using an Acoustic Doppler Current Profiler (SonTek RiverSurveyor M9 ADCP) throughout the first semester of 2022 (from 04 January 2022 to 21 June 2022) at N1, N2, N3, and N4 to generate their rating curves (Table S3.2). Subsequently, the water level (m) was measured daily at N1, N2, and N3 during the first semester of 2023 (from 01 January 2023 to 09 May 2023), and the rating curves were used to compute the inflow (m^3/s). Daily measurements at the N4 gauge in 2023 were unavailable owing to technical difficulties. We also encountered similar technical issues at the N2 gauge starting 10 May 2023. The daily volume, however, was measured during the first half of 2022 and 2023 within a 24-hour interval, starting at 07:00 on the day before the measurement.

Daily rainfall data for the study site were accessible through FUNCEME (see http://www.funceme.br/app-calendario/). We computed average rainfall using the Thiessen Polygons method (Akhter *et al.*, 2022) with FUNCEME's Hydrological Calculation software, "SIGA" (see http://www.siga.funceme.br). Daily evaporation data were obtained from INMET at the Jaguaribe station (see https://bdmep.inmet.gov.br/), near the N3 gauge. All data and their sources are listed in Table 7.

Table 7 - Outline of input data sources

Input data	**Data source**
For the numerical model	
Triangular shape of the river cross-section	Estimated
Area, perimeter, top width, and hydraulic radius	Derived from river stage data and triangular cross-section
DEM	Copernicus GLO-30, ESA (https://sentinels.copernicus.eu/web/sentinel/copernicus)
Channel length, slope, and sub-catchment area	Derived from the Copernicus GLO-30 using the QGIS raster analysis tool
Curve Number	National Water and Sanitation Agency of Brazil (ANA) (https://metadados.snirh.gov.br/geonetwork/srv/

	api/records/d1c36d85-a9d5-4f6a-85f7-71c2dc801a67)
Hydraulic conductivity of the riverbed	Hazen's method with data provided by Wiegand (2009)
Hydraulic conductivity of the alluvium and aquifer width	Brazilian Geological Service (CPRM) (https://rigeo.sgb.gov.br/)
Daily rainfall	Ceará Foundation of Meteorology and Water Resources (FUNCEME) (http://www.funceme.br/app-calendario/)
Daily evaporation	National Institute of Meteorology (INMET) (https://bdmep.inmet.gov.br/)
Observed	
Inflow, river stage, and volume	Daily measurements using an Acoustic Doppler Current Profiler (SonTek RiverSurveyor M9 ADCP) and rating curves

Source: prepared by the author.

3.2.3 River routing

We developed an original river routing model based on a nonlinear variation of the Muskingum-Cunge method proposed by (Lu *et al.*, 2021). According to Toné *et al.* (2023), the flow velocity demonstrates a nonlinear temporal response to an increase in river stage across the study site. The original model proposed is a semi-distributed flow routing approach that takes into account this intricate phenomenon (El-Nasr *et al.*, 2005; Fread, 1993), as well as sub-catchment runoff, river-aquifer interaction, and river rainfall/evaporation fluxes.

For each of the three reaches, streamflow along the Δx river length at each Δt time step—accounting for a one-day lag between river gauges (Costa *et al.*, 2013)—is calculated as follows:

$$Q_{t+\Delta t} = \frac{1}{1-X}\left(\frac{S_t}{K}\right)^{\frac{1}{\gamma m}} - \frac{X \cdot I_t + \pi + \mu + \Omega + \partial}{1-X} \tag{3.1}$$

Where $Q_{t+\Delta t}$ represents the outflow (m^3/s), S_t denotes the storage volume (m^3), K is the storage constant (s), X is the weighting factor, γ and m are the calibrated exponents that relate storage and weighted flow, and I_t is the inflow (m^3/s). Gauged flow and volume data were used for all S_t and I_t values for each reach. Additionally, π represents the direct flux within the river (m^3/s), μ denotes the sub-catchment runoff (m^3/s), and Ω represents the river-aquifer interaction (m^3/s). δ is the volume of water used to meet the demand within each river reach, including groundwater extraction from operational wells and direct pumping from the river (m^3/s), which were considered insignificant at the study site (Toné e*t al.* 2023). We propose the following rules for the γ value.

$$\begin{cases} \text{if } h_{\text{river}} \leq h_{r,m}, \text{ then } \gamma = \gamma^{+} \\ \text{if } h_{\text{river}} > h_{r,m}, \text{ then } \gamma = \gamma^{-} \end{cases} \tag{3.2}$$

Where h_{river} represents the river head (m), $h_{r,m}$ represents the mean river head at the river's entrance boundary (m), and γ+ and γ- represent the γ values that increase or decrease the relationship between storage and weighted flow. In this context, the calibration process requires only three parameters for computing the numerical model: m, γ+, and γ−. To calculate K, it is necessary to compute the kinematic wave celerity (c) (m/s) beforehand as follows (Fread, 1993):

$$c = k'v = k' \frac{I_t}{A} \tag{3.3}$$

Where k' is the kinematic ratio, v is the flow velocity (m/s), and A is the wetted area (m^2). Assuming a triangular cross-sectional area for the river channel, with 45-degree angles on both sides, k' can be estimated using the following equation:

$$k' = \frac{5}{3} - \frac{2}{3} \cdot \frac{A}{BP} \cdot \frac{dP}{dy} = \frac{5}{3} - \frac{4\sqrt{2}}{3} \cdot \frac{A}{BP} \tag{3.4}$$

Where B represents the top width of the cross-section (m), assumed to remain constant since there is no flow beyond the main channel (344.65 m), and P represents the perimeter of the wetted cross-section (m). The parameters K and X can then be calculated as follows:

$$K = \frac{\Delta x}{c} \tag{3.5}$$

$$X = \frac{1}{2} - \frac{I_t}{2 \cdot c \cdot B \cdot s \cdot \Delta x} \tag{3.6}$$

Where s is the river slope (m/m). We compute the π component using the equation of Kim *et al.* (2022) modified:

$$\pi = a_{riv} \cdot (e - p) \tag{3.7}$$

$$a_{riv} \; = \; B \cdot \Delta x \tag{3.8}$$

Where a_{riv} represents the river area (m^2), and e (mm) and p (mm) denote evaporation and rainfall, respectively. We calculate the μ component using the SCS-CN method, which involves the following equations (Mishra; Singh, 2003):

$$\mu \; = \; A_{sc} \cdot \frac{(p-0.2S)^2}{(p+0.8S)} \tag{3.9}$$

$$S \; = \frac{25{,}400}{CN_w} - 254 \tag{3.10}$$

$$CN_w \; = \sum \frac{CN_j A_j}{A_{sc}} \tag{3.11}$$

Where A_{sc} is the area of the sub-catchment (m^2), S is the potential maximum soil retention in the sub-catchment (mm), CN_w is the weighted average curve number parameter, and Aj is the individual area (m^2) comprising the sub-catchment with a specific CN_j (Rajasekhar *et al.*, 2020; Ramakrishnan; Durga Rao; Tiwari, 2008). The maximum value of μ for each river reach was defined as the average daily inflow measured during the first half of 2022 and 2023 (see the Study Area). The ANA (2018) raster data type (see Datasets) determines CNj. Subsequently, if required, CNj is adjusted based on the actual moisture precondition (type 1 or 3) in response to the previous daily rainfall (p), as outlined in equations 3.12 and 3.13 (Mishra; Singh, 2003).

$$CN_1 = 4.2 \cdot \frac{CN_2}{(10\text{-}0.058CN_2)} \tag{3.12}$$

$$CN_3 = 23 \cdot \frac{CN_2}{(10+0.13CN_2)} \tag{3.13}$$

Equation 3.14 is the physical hydraulic filter governing the states of $Q_{t+\Delta t}$. This equation applies to river reaches and stream stretches within sub-catchments.

$$\begin{cases} Q_{t+\Delta t} \geq 0 \\ \text{if } Q_{t+\Delta t} < I_t, \text{ then } A_{t+\Delta t} < A_t \\ \text{if } Q_{t+\Delta t} > I_t, \text{ then } A_{t+\Delta t} > A_t \end{cases} \tag{3.14}$$

3.2.4 Groundwater flow

The aquifer stage head must first be estimated to calculate the river-aquifer interaction term (**Ω**). The scarcity of field measurements of groundwater in the semi-arid region of Brazil (Cirilo *et al.*, 2020; Costa *et al.*, 2023; Kim *et al.*, 2022) led us to utilize the analytical solution for aquifer heads proposed by (Chesnaux; Molson; Chapuis, 2005) for unconfined aquifers (equation 3.15) owing to its versatility and accuracy. This solution is based on Darcy's law and the Dupuit theory. It considers an impermeable boundary surrounding the aquifer, with a fixed-head boundary on the side adjacent to the river. As mentioned above, the river cross-section was assumed triangular (Figure S3.4).

$$h_{aq} = \sqrt{\frac{WL'^2}{K_{aq}} + h_{river}^2} \tag{3.15}$$

Where h_{aq} represents the aquifer head (m), which is fixed prior to river routing, W represents the recharge rate (mm), L' means the aquifer width of 25 m (CPRM 2014, 2015; Palheta et al. 2019), and K_{aq} represents the hydraulic conductivity of the aquifer (mm/d). Nevertheless, considering the conceptual model in Figures 14 and S3.1, the aquifer head is below the river bottom during the dry season ($p \leq 10$ mm/day). During rainy seasons ($p > 10$ mm/day), the aquifer head is above the river head (refer to Datasets for daily rainfall data in both seasons), and the following rules are proposed for the h_{aq} (m):

$$\begin{cases} \text{if } p \leq 0.01p_m \text{ mm, then } h_{aq} < 0 \\ \text{if } p > 0.01p_m \text{ mm, then } h_{aq} > 0 \end{cases} \tag{3.16}$$

Negative values of h_{aq} (m) correspond to an aquifer stage below the river bottom, and p_m represents the mean annual precipitation depth at the study site (1,000 mm). Previous research has demonstrated that groundwater levels in the alluvial aquifer of the semi-arid region of Ceará, Brazil, for Figure S3.1b cases (dry season), range from -1 to -20 meters below the surface (Costa *et al.*, 2013; Alves *et al.*, 2024). Accordingly, the h_{aq} value is the reverse of equation 3.15 for previous non-intense rainfall events ($p < 10$ mm/day), as the values would fall within that interval. The recharge rate (W) was estimated as 20% of the rainfall for alluvial areas within dryland regions (equation 3.17) (Andualem *et al.*, 2021).

$$W = 0.20 \cdot p \tag{3.17}$$

The difference between h_{aq} and h_{river} results in the head difference (Δh). By applying Darcy's law, the flow between the aquifer and the river can be calculated (Equation 3.18), where the negative sign indicates that water moves towards the decreasing hydraulic head (Sophocleous, 2002).

$$q_{head} = -K_{aq} \cdot A_{lk} \cdot \frac{\Delta h}{L'} \tag{3.18}$$

Where A_{lk} represents the cross-sectional area available for flow (m^2), and positive values in equation 3.18 indicate a contribution from the aquifer to the river as baseflow. In contrast, negative values indicate the opposite direction, contributing to the aquifer recharge. However, hyporheic flow originating from upstream infiltration is considered an important process for river-aquifer interaction downstream of the study site (Toné *et al.*, 2023). Equation 19, adapted from (Watson *et al.*, 2021) by incorporating a negative sign, calculates the seepage volume in the river reach, contributing downstream as a hyporheic flow.

$$q_{sp} = -min\;(I_t; K_{rb} \cdot sink_a \cdot R_h^2 \cdot \Delta x) \tag{3.19}$$

In equation 3.19, K_{rb} represents the hydraulic conductivity of the riverbed (m/d), R_h is the hydraulic radius of the river cross-section (m), and $sink_a$ is a scaling parameter, which is assumed to be equal to the hydraulic radius. Finally, the sum of q_{head} (m^3/s)

and q_{sp} (m^3/s) yields the total groundwater flow (equation 3.20) for the river-aquifer interaction estimation (Ω). After computing **Ω**, flood wave routing was applied using the previously mentioned nonlinear Muskingum-Cunge equation (eq. 3.1) to determine the outflow at each river reach.

$$\Omega = q_{head} + q_{sp} \tag{3.20}$$

3.2.5 Parameter analysis and performance criteria

We subsequently performed an individual parameter analysis to facilitate data acquisition and the calibration process in future research. We selected the following parameters for sensitivity analysis: a) hydraulic conductivity of the riverbed and (b) the alluvium, as these parameters influence the calculation of the water table and groundwater fluxes (eqs. 3.15, 3.18, and 3.19); (c) aquifer width and (d) top cross-sectional width, both of which are associated with streamflow routing and stream-aquifer interactions (eqs. 3.1 and 3.20). Furthermore, the contributions of lateral tributary inflow (sub-catchment runoff), baseflow, and hyporheic flow were analysed to assess their influence on streamflow. Equation (3.21) was used as the standard formulation:

$$\varphi = \frac{y(P) - y_{obs}}{y_{obs}} \tag{3.21}$$

Where φ represents the sensitivity coefficient, y represents the predicted variable (streamflow), and P represents the model parameter, or one of the previously overlooked flow components. The events with the highest simulated inflow peaks in each river reach were selected for sensitivity analysis. Subsequently, to estimate the streamflow sensitivity coefficients (equation 3.21), the original parameter values or overlooked flow components were multiplied by a variable factor, and the original numerical model (eq. 3.1) was re-run.

Finally, the calibration period was divided into two intervals: period 1, from 04 January 2022 to 21 June 2022 (169 daily streamflow measurements); period 2, from 04 January 2023 to 09 May 2023 (126 daily streamflow measurements). Then, the model calibrated with period 1 was cross-validated using data from period 2 and vice versa.

During the calibration process, our objective was to match the simulated streamflow with daily measurements obtained from the river gauges in the Middle Jaguaribe River. Three commonly used statistical measures in hydrological modelling were employed as performance criteria (Rabelo *et al.*, 2021): the Kling-Gupta Efficiency (KGE), the Nash-Sutcliffe Efficiency (NSE), and the percent bias (PBIAS).

3.3 Results

These results were derived from each stream gauge's daily streamflow and river stage measurements during Periods 1 and 2 (Figure 15). Subsequently, these measurements were used to validate the original model and ensure its accuracy. In particular, there was a trend toward river losses between N1-N2 and N3-N4 and river gains between N2-N3 in both periods. This trend shows a certain degree of stationarity between the study periods, which may enhance predictive performance of the model in the study area. However, extreme weather events driven by global climate change may increase the complexity of streamflow forecasting under low- and high-flow conditions (Mamudu *et al.*, 2025; Zhang *et al.*, 2022).

The maximum observed streamflow values for each river gauge in Period 1 were 312.81 m^3/s (N1), 364.44 m^3/s (N2), 438.19 m^3/s (N3), and 536.72 m^3/s (N4). In contrast, the values in period 2 were 512.34 m^3/s (N1), 762.74 m^3/s (N2), and 651.60 m^3/s (N3). These values fall within the range of the daily observed values reported in previous studies for the Middle Jaguaribe River during the dry season (Costa et al. 2012). Notably, N2 revealed a more than 50% increase in streamflow in period 2 compared to that in period 1 (see Discussion below). The average river stage values measured for each reach were 2.64 m, 1.71 m, and 3.05 m during Period 1, and 2.34 m, 1.77 m, and 2.80 m during Period 2.

We collected streamflow and river stage measurements during the rainy season. Nevertheless, daily evaporation exceeded precipitation on 68.45% of the days in Period 1, while precipitation exceeded evaporation on 54.69% of the days in Period 2. In this sense, the average catchment daily recharge (W) was higher in Period 2 (2.26 mm) than in Period 1 (0.79 mm). During Period 1, average groundwater levels remained below the riverbed across all three reaches, reaching a minimum of -3.79 m in Reach 3. In Period 2, average groundwater levels ranged from -3.50 m to 9.16 m relative to the riverbed, encompassing negative and positive values. The highest daily groundwater levels occurred during Period 2, when positive direct fluxes to the river (rainfall minus evaporation) were more frequent.

The average sub-catchment surface runoff (μ) in the three sub-catchments was 16.92 m^3/s, 4.15 m^3/s, and 23.55 m^3/s during Period 1, and 25.45 m^3/s, 11.13 m^3/s, and 30.00 m^3/s during Period 2. Higher runoff values in Sub-catchments 1 and 3 were expected, as the area of sub-catchment 2 was 56.13% smaller than that of sub-catchment 1 and 27.31% smaller than that of sub-catchment 3. The positive and negative daily flux values between the aquifer and river (q_{head}) were calculated for both periods. The highest value was recorded in Reach 1 during Period 1 (197.62 m^3/s), and the lowest in Reach 3 during Period 2 (–312.66 m^3/s). These values depend on the head difference on a given day and on the measured river stage. Hyporheic flow values (qsp) were consistently negative, with average values ranging from –2.65 m^3/s to –82.27 m^3/s, as they depend on the hydraulic radius, which is also influenced by the river stage.

Figure 15 - Observed streamflow (a) and river stage head (b) series during calibration periods: Period 1 (2022) and Period 2 (2023).

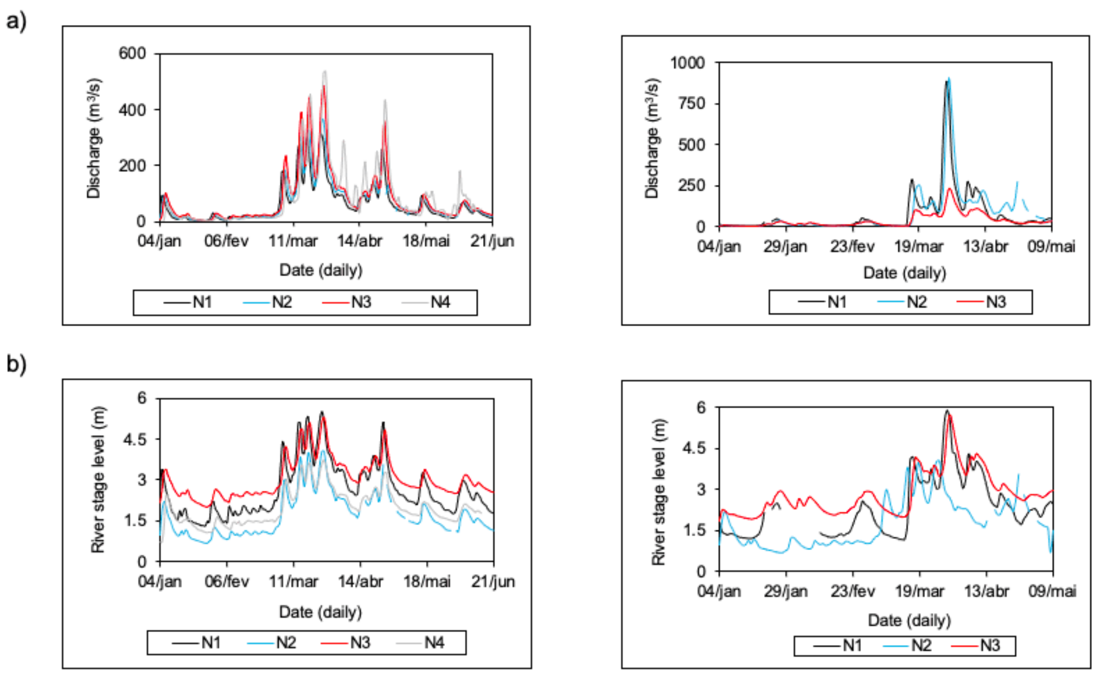

Source: prepared by the author.

3.3.1 Calibration and validation

Three parameters are required to calibrate the original model (see Table S3.3). Table 8 presents the calibration and validation performance metrics, with threshold values for satisfactory and unsatisfactory performances. The PBIAS values for Period 1 indicated satisfactory calibration performance for Reach 1, good performance for Reach 3, and unsatisfactory performance for Reach 2. In contrast, the NSE values demonstrated satisfactory performance for Reaches 1 and 3, whereas Reach 2 remained unsatisfactory. The analysis of KGE values also confirmed a good overall fit between the observed and simulated flows at the four river gauges during Period 1. The validation metrics for Period 2 met the desired standards for Reaches 1 and 2, indicating satisfactory accuracy (Moriasi; Gitau; Daggupati, 2015).

Table 8 - Evaluation of the model performance metrics for streamflow at the three river reaches during calibration periods 1 and 2 using two-fold cross-validation of the dataset, where KGE is the Kling-Gupta Efficiency, NSE is the Nash-Sutcliffe Efficiency, and PBIAS is the percent bias.

Periods	**Process**	**Statistical criteria**	**Satisfactory performance***	**Reach 1**	**Reach 2**	**Reach 3**
1	Calibration	KGE	0.51< KGE	0.60	0.01	0.78
		NSE	0.50 < NSE < 0.70	0.63	0.42	0.69
		PBIAS (%)	±15 ≤ PBIAS ≤ ±45	36.91	60.67	13.47
2	Validation	KGE	0.51< KGE	0.56	0.32	
		NSE	0.50 < NSE < 0.70	0.54	0.50	
		PBIAS (%)	±15 ≤ PBIAS ≤ ±45	18.58	22.13	
2	Calibration	KGE	0.51< KGE	0.48	0.51	
		NSE	0.50 < NSE < 0.70	0.51	0.56	

		PBIAS (%)	±15 ≤ PBIAS ≤ ±45	17.22	27.45
1	Validation	KGE	0.51< KGE	0.54	0.67
		NSE	0.50 < NSE < 0.70	0.58	0.89
		PBIAS (%)	±15 ≤ PBIAS ≤ ±45	42.59	26.76

* Threshold values from Moriasi *et al.* (2015) and Lamontagne *et al.* (2020)

Source: prepared by the author.

The performance metrics (PBIAS, KGE, and NSE) for period 2 indicated a satisfactory accuracy level for calibration in both reaches. Through the validation process with period 1, satisfactory accuracy was found for reach 1 and a significantly good accuracy for reach 2 (Moriasi *et al.*, 2015). Figures 16 (a, b, c) and 17 (a, b) depict the calibration and validation processes for periods 1-2, respectively, while Figures S3.5 (a, b) and S3.6 (a, b) depict them for period 2-1.

The graphs reveal that the outflow was accurately simulated over the 70 km stretch of the Jaguaribe River, even though no groundwater level data were measured during calibration periods 1 and 2. The analysis revealed that the recession curve in Figure 16 approached zero on specific days following discharge peaks. In contrast, the observed data indicated that the streamflow persists for a few days. The constant values of hydraulic conductivity and the simplified approach used to simulate groundwater flow at the study site may have influenced the recession flow by neglecting factors, such as unsaturated subsurface water redistribution within the alluvium (Costa *et al.*, 2012; Rabelo *et al.*, 2021).

Figure 16 - Observed and estimated daily streamflow at reaches 1 (N1-N2), 2 (N2-N3), and 3 (N3-N4) during the calibration period 1 (from 04 January 2022 to 21 June 2022).

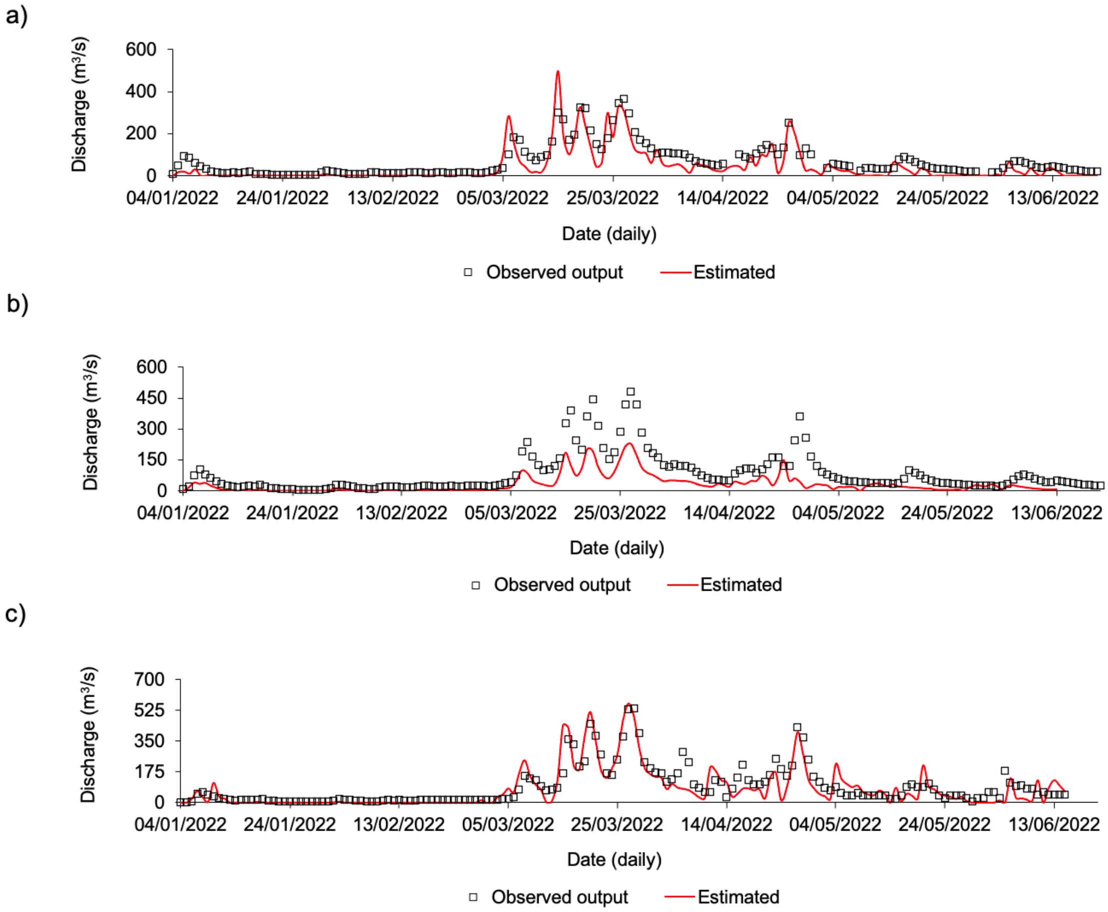

Source: prepared by the author.

Figure 17 - Observed and estimated daily streamflow at reaches 1 (N1-N2) and 2 (N2-N3) during the validation period 2 (from 04 January 2022 to 21 June 2022).

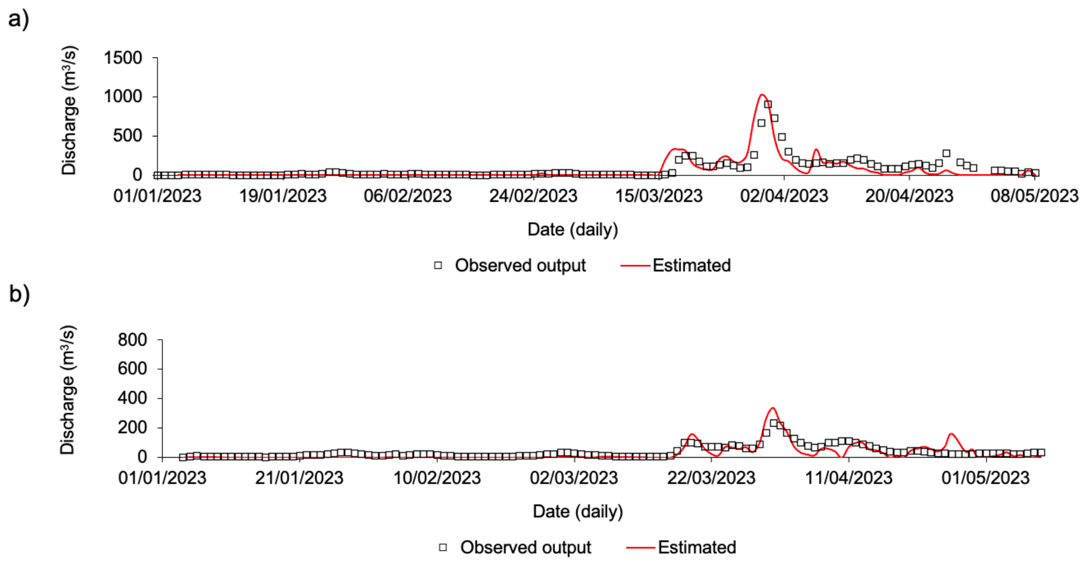

Source: prepared by the author.

Once the original model demonstrated satisfactory accuracy in streamflow estimation, a sensitivity analysis of the parameters a-d outlined in the Data and Methods was conducted. The sensitivity coefficients for the variations in the hydraulic conductivity of the riverbed and alluvium were high (Figures 18a-b), indicating substantial and rapid variability in the results with changes in these parameters. Nevertheless, the sensitivity of hydraulic conductivity in the alluvium was negligible for values exceeding the original value. The sensitivity of aquifer width revealed that values lower than the original significantly affected the results (Figure 18c), whereas higher values produced variations of up to 20%. Additionally, the cross-sectional width demonstrated a high sensitivity coefficient for changes ranging from 0.01% to 1% of the original value, with negligible sensitivity to larger variations (Figure 18d). The results indicate that riverbed hydraulic conductivity and aquifer width are more critical for applying the stream-aquifer model in data-scarce environments.

The following flow components were selected for the sensitivity analysis: (1) baseflow and (2) hyporheic flow, both of which influence the calculation of stream-aquifer fluxes (eqs. 3.18–3.20); and (3) lateral tributary flow (sub-catchment surface runoff), associated with streamflow routing (eq. 3.1). The sensitivity coefficients for the variations in these flow components were high (Figure 19), indicating significant and rapid changes in the results as the parameters varied. However, the hyporheic and lateral tributary flow sensitivities were negligible at values below the original value. The analysis revealed that only values significantly higher than the original for hyporheic flow affected the results (Figure 19b). In contrast, the lateral tributary flow required changes of ten times the original value to produce noticeable variations. Baseflow exhibited high sensitivity to minimal changes in its original value (Figure 19a).

Figure 18 - Sensitivity analysis of (a) hydraulic conductivity of the riverbed, (b) hydraulic conductivity of the alluvium, (c) aquifer width, and (d) cross-section top width, where φ is the sensitivity coefficient (eq. 3.21) and the x-axis represents the scaling factors applied to the original parameter values in each re-run of the numerical model.

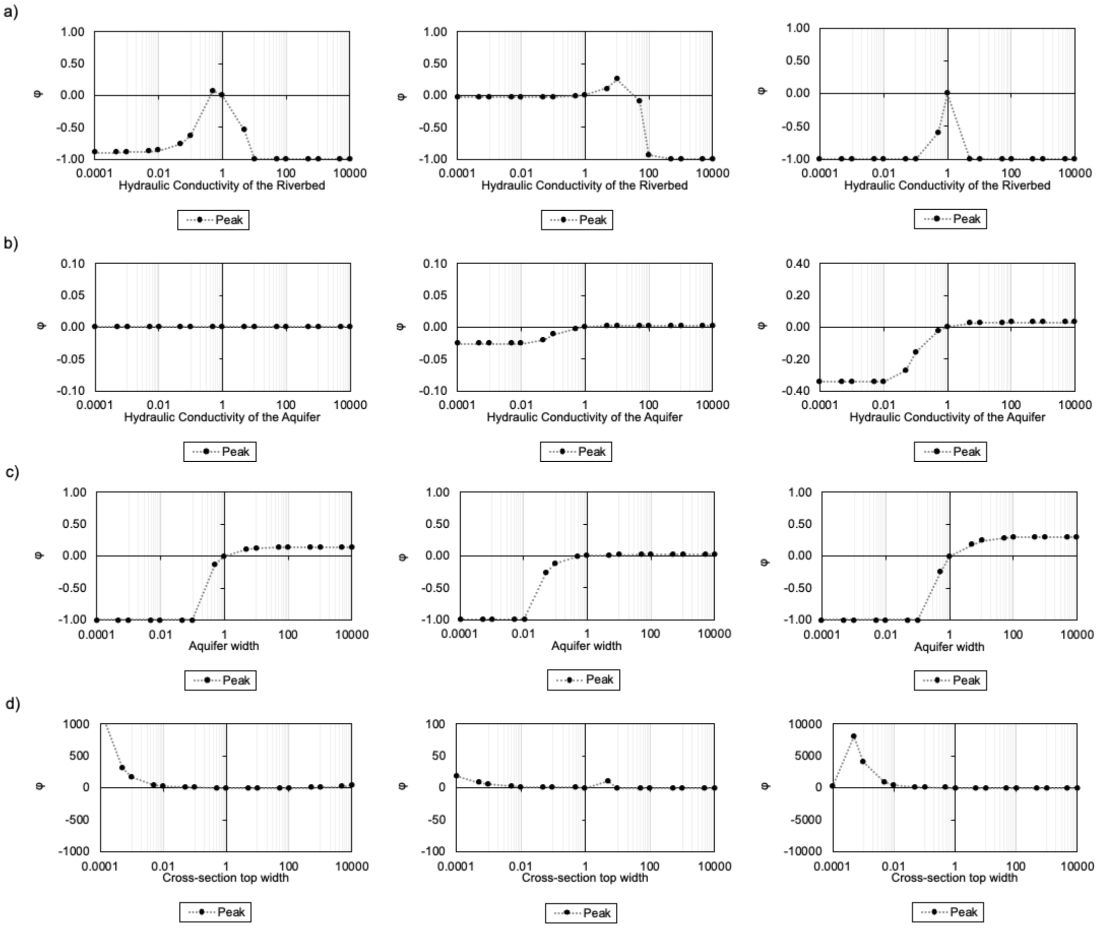

Source: prepared by the author.

Figure 19 - Sensitivity analysis of (a) baseflow, (b) hyporheic flow, and (c) lateral tributary inflow, where φ is the sensitivity coefficient (eq. 3.21) and the x-axis represents the scaling factors applied to the original parameter values in each re-run of the numerical model.

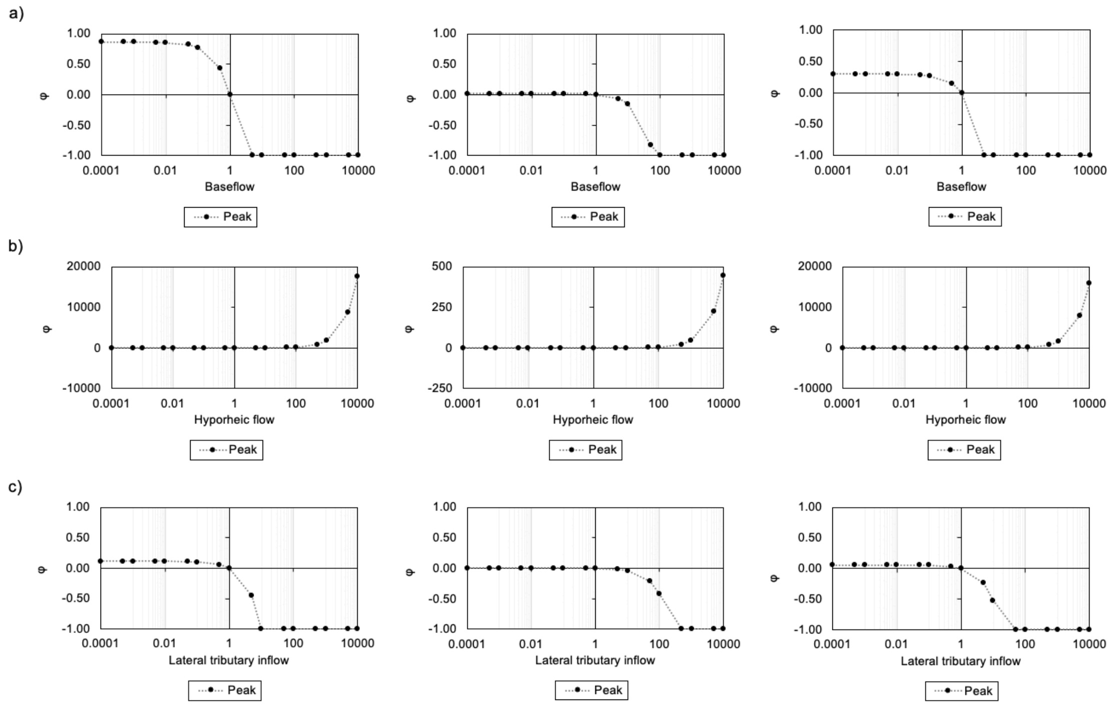

Source: prepared by the author.

3.3.2 River-aquifer interaction

During the calibration-validation processes, the numerical model calculated outflow magnitudes exceeding the peak inflows, except for reach 2 (Figure S3.8). The analysis was limited when low inflows were observed, although a trend of lower outflows was apparent. On average, the numerical model (eq. 3.1) estimated river losses of 79% in reach 1, 66% in reach 2, and 69% in reach 3, during the calibration validation process. Conversely, the numerical model computed river gains of 43%, 1%, and 79% in reaches 1, 2, and 3, respectively.

It is also possible to compare the individual values of inflow (I), river rainfall/evaporation flow (π), sub-catchment runoff (μ), and river-aquifer interaction (Ω), which are some of the parameters used to calculate the outflow (equation 3.1). This comparison can be observed in Figure 20, as exemplified by the first calibration-validation process. It is apparent that, except for reach 2 in both cases (see Discussion below), high inflow values result in high river loss values as the hydraulic head increases. We also observed the parameters π and μ had a relatively minor influence on calculating the outflow in the Middle Jaguaribe River compared to the inflow volumes.

Figure 20 - Comparison between values of inflow (I), river rainfall/evaporation flow (π), sub-catchment runoff (μ), and river-aquifer interaction (Ω) in river reaches 1, 2, and 3 during calibration period 1 (a, b, c) and validation period 2 (d, e), respectively.

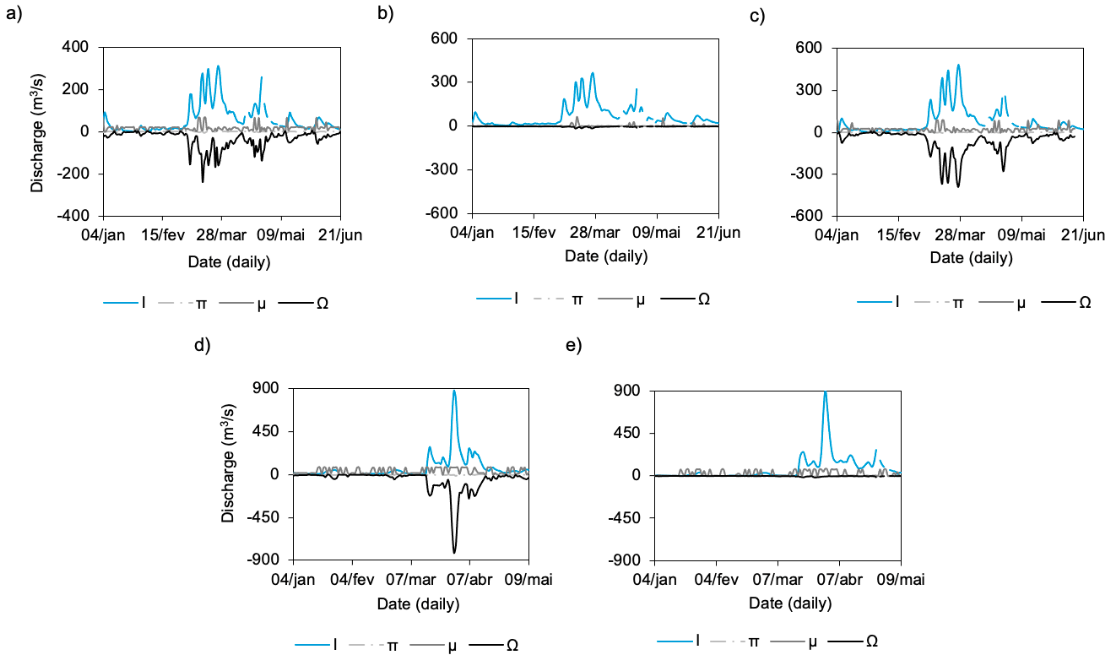

Source: prepared by the author.

The influence of the sub-catchment runoff and groundwater fluxes can be evaluated by comparing different model structures using the same parameter set. As shown in Figure S3.3, the original model employs a river routing equation (eq. 3.1), which accounts for three key hydrological processes: baseflow, hyporheic flow, and subcatchment runoff (lateral tributary inflow). We tested four model structures using exact spatial discretization and parameter values to assess which combination yielded the most accurate simulation, that is, the best performance metrics. These structures were defined as follows: (1) lateral tributary inflow with both baseflow and hyporheic flow (i.e., the proposed model described in equation 3.1) (LTI+BF+HF), (2) lateral tributary inflow with hyporheic flow but without baseflow (LTI+HF), (3) lateral tributary inflow with baseflow but without hyporheic flow (LTI+BF), and (4) baseflow with hyporheic flow but without lateral tributary inflow (BF+HF). Figure 21 shows the observed and simulated streamflow series for each configuration.

Figure 21 - Observed and estimated daily streamflow at reaches 1 (a), 2 (b), and 3 (c) in 2022. The four model structures tested were (1) lateral tributary inflow with both baseflow and hyporheic flow (i.e., the numerical model described in equation 3.1) (LTI+BF+HF); (2) lateral tributary inflow with hyporheic flow but without baseflow (LTI+HF); (3) lateral tributary inflow with baseflow but without hyporheic flow (LTI+BF); and (4) baseflow with hyporheic flow but without lateral tributary inflow (BF+HF).

a)

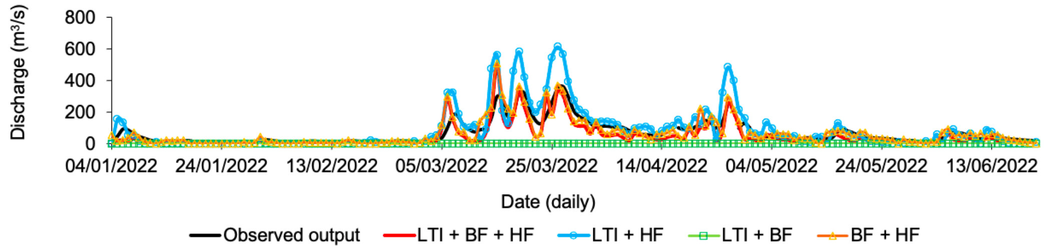

b)

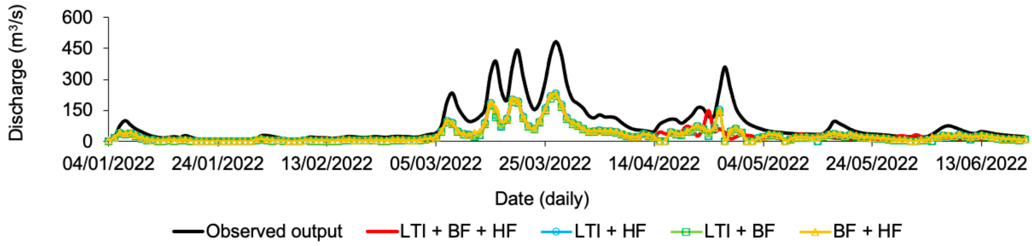

c)

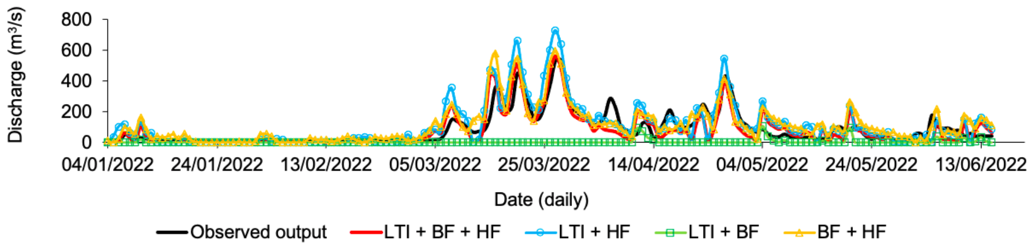

Source: prepared by the author.

3.4 Discussion

3.4.1 Numerical model

The performance metrics (see Table 8) demonstrated the effectiveness of the model in estimating outflow and capturing peak flow events, despite data scarcity, the calibration requirement of only three parameters, and the arid conditions of the study site. The original model (eq. 3.1) successfully captured the behavior of the observed streamflow curve. Nevertheless, the streamflow model has limitations: (a) it assumes an isotropic, unconfined aquifer with a single layer, and (b) it does not account for flow beyond the river's main channel. The same trend of river losses and gains was identified between river gauges (Figure 15), which improved the predictive performance of the numerical model (Gibbs *et al.*, 2018). Nevertheless, the discrepancies between the estimated and observed data in reach 2 (see Results), such as in the magnitude of peak flows (Figure 16), although small, may be partly explained by the simple equations used to represent groundwater flow, as well as the constant value of the hydraulic conductivity of the river and alluvium. These factors also affect the drops in the recession flow indicated in Figures 16-17, as they are used to calculate the river-aquifer interaction. Numerical models of dryland rivers have revealed similar behavior regarding the decrease in recession flow and the magnitude of peak flows (Kim *et al.*, 2022; Rabelo *et al.*, 2021).

Rainfall data were uncertain during modeling owing to gaps in rain monitoring days, despite the 14 available stations providing a broad range of rainfall records. Human errors or interpolation procedures used to compensate for gaps with the SIGA software could also impact numerical modeling, although no significant errors were found. During low rainfall events (<10 mm/day), the estimated aquifer head (equation 3.15) was lower than the river stage, indicating a hydraulic disconnection between the aquifer and the river. This results in vertical groundwater flow (Sophocleous, 2002), as the conceptual model proposed for the Middle Jaguaribe River and used in this study previously indicated (Figure S3.1). Negative hydraulic head values are more frequent in the dryland regions and are consistent with previous studies at the study site (Costa *et al.*, 2013; Toledo *et al.*, 2018).

The parameters to which the model demonstrated high sensitivity (conductivity parameters) were related to soil storage and groundwater fluxes (refer to equations 3.15-3.20), whose effects on streamflow are more pronounced in dryland catchments (Gosling; Arnell, 2011), such as the study site. Nevertheless, this aligns with the significance of baseflow in streamflow during the rapid rise in the water table. Based on the quantile-quantile plot (Figure S3.7) of the streamflow data measured in periods 1 and 2, the original model did not assume normality when computing the outflow in each river reach. In addition to the outflow, the model also estimates other fluxes, such as river rainfall/evaporation flow, hyporheic flow, and lateral tributary flow, which are sources of groundwater recharge and are essential for a more accurate account of the river water balance (see Figure 20). Although these fluxes cause fluctuations in the assumed one-day lag discharge (e.g., after consecutive rainfall and rapid river discharge decrease), introducing uncertainties in the computed outflow, the daily time-step has been demonstrated to be reasonably appropriate to estimate it. This temporal scaling aligns with several river-aquifer interaction models under similar conditions (McMahon; Nathan, 2021). Moreover, these computed flows do not require large amounts of data, which is difficult to find in dryland regions (Kim *et al.*, 2022; Kumar *et al.*, 2024; Mujere *et al.*, 2022). This simplicity and data efficiency represent key advantages of the original model (eq. 3.1), particularly for applications in data-scarce dryland regions.

3.4.2 River-aquifer interaction processes

Several important parameters affect river-aquifer interactions in dryland rivers, including the (a) infiltration rate of the riverbed, (b) overland velocity, and (c) lateral tributary inflow (Wolstenholme *et al.*, 2020). Figure 20 illustrates that sub-catchment runoff had a low impact on river loss or gain calculations, as indicated by previous river-aquifer interaction studies (Mujere *et al.*, 2022). Figure 21 illustrates this surface runoff behavior by comparing the four possible model structures (see Results section). The LTI+HF-based model overestimated the streamflow peaks in reaches 1 and 3, although the difference between the observed and estimated values was not significant. By contrast, the LTI+BF-based model failed to provide accurate streamflow estimates for these reaches. No significant difference was observed between the BF+HF and the LTI+BF+HF-based models (eq. 3.1) in reaches 1 and 3, respectively. These results suggest a predominant influence of hyporheic flow in these reaches compared to lateral tributary flow and baseflow. However, all four model structures produced similar results for reach 2 (see Figure 21), indicating that inflow dominates in this reach. Among the fluxes, only the baseflow exhibited high sensitivity coefficients for lower and higher values relative to the original (see Figure 19). In contrast, hyporheic flow and lateral tributary inflow displayed negligible sensitivity, even for values up to ten times the original (Figure 19). Considering the three reaches, the results suggest that hyporheic flow, an often-overlooked component of stream-aquifer fluxes, may be crucial for informing water resource management in dryland rivers.

Based on the assumption of a constant triangular river cross-sectional area (refer to Datasets), higher streamflow values observed between contiguous river gauges in both calibration periods resulted in shorter seepage times. This may partially explain the higher estimated outflow values compared with the observed inflow during peak flow events in the two-fold calibration-validation processes, even though there is a preferential flow from the river to the aquifer.

Based on the conceptual framework upon which the numerical model is founded (refer to Supplementary Material), both baseflow and hyporheic flow contribute to river volume, and their estimated discharges exceed river losses most of the time in reach 2 (refer to Figure S3.8). These computed losses occurred at the beginning of the rainy season (<10 mm/day), corroborating a higher dependence on the river inflow volume and stage rather than intraseasonal rainfall. This approach improves the model accuracy by relying on surface inflow and outflow measurements over several days for each river reach. Although groundwater flow or bed infiltration measurements would more accurately compute river losses (McMahon; Nathan, 2021), they could compromise the parsimony of the model. These may be difficult to obtain because of the sparse network of monitoring gauges in dryland rivers.

Figure 20 also shows that high inflow values result in high river loss values, as previously indicated by Costa *et al.* (2013), Mujere *et al.* (2022), and Toledo *et al.* (2018), with the exception of the reach 2. The formation of a clogging layer during the dry season (second half of the year) may explain these river losses; the first streamflow events in Reach 1 removed this layer. Additionally, vertical infiltration in this reach (indicated by a negative hydraulic head at the beginning of the rainy season) may favor downstream river gains. We compared the estimated values of river loss and river gain with those reported in other river–aquifer studies, including Batlle-Aguilar and Cook (2012), Hughes (2019), Lange (2005), and Morin *et al.* (2009). The numerical model computed daily values close to the values in these studies. It is worth noting that the original model (refer to equation 3.1) could compute daily river-aquifer interactions with values close to those found in other dryland regions, even in the absence of groundwater flow measurements due to data scarcity.

3.5 Conclusion

This study developed a simple original model for river-aquifer interactions in dryland rivers. It was designed to address data scarcity and does not require extensive data, such as aquifer head measurements. Because the model also computes other fluxes that influence river-aquifer interactions, such as hyporheic flow, despite its simplicity, it can also contribute to a more accurate water balance between river reaches. In addition, future work will involve integrating the proposed numerical model into the existing management operation model used in Brazilian semi-arid reservoirs for hydrological drought events. This may enhance the estimation of key hydrological processes that influence the water balance of reservoirs in semi-arid regions.

The principal findings of this study are summarized as follows.

- A simplified model framework can represent river-aquifer interactions and outflow in dryland rivers at a watershed scale, even without groundwater flow measurements.
- Hyporheic flow, an often-overlooked component of stream aquifer fluxes, may be crucial for water resource management in dryland rivers.
- The parameters necessary for the numerical model are often available despite a sparse network of river gauges.
- Riverbed hydraulic conductivity and aquifer width are critical for applying the original model to data-scarce environments.
- River loss occurred at the beginning of the rainy season (<10 mm/day), highlighting a greater dependence on river inflow volume and stage rather than intraseasonal rainfall.
- Sub-catchment runoff had a minimal influence on river-aquifer interactions compared with inflow and groundwater fluxes.

3.6 Funding

The present study was supported by the National Council for Scientific and Technological Development – CNPq (#307680/2023-1) and the Brazilian Federal Agency for Support and Evaluation of Graduate Education – CAPES (#88887.007807/2024-00).

4 ADAPTIVE HEDGING RULES FOR A DATA-SCARCE DRYLAND RESERVOIR: INTEGRATING SIMPLE DROUGHT INDEX, WATER USER PARTICIPATION, AND SHORT-TERM HYDROLOGICAL MONITORING[3]

4.1 Introduction

Recent climate changes in dryland regions have shown higher warming rates and declining precipitation, extending the duration of dry periods (Daramola; Xu, 2022). The rapid negative impacts of meteorological droughts on subsurface and surface water supplies in drylands shorten early warning times, highlighting the need for adaptive management to reduce the effects of climate variability on water scarcity in the region (Ahana *et al.*, 2025). An effective drought management framework requires risk reduction strategies and tools. Two common strategies for long- and short-term water vulnerability mitigation are the construction of reservoirs and the implementation of demand restrictions through the regulation of river and groundwater exploitation (Akram, 2025; Cid *et al.*, 2023). Drought indices serve as decision support tools, and there is extensive literature on their use in drought monitoring and triggering mitigation measures based on onsite conditions. While the utility of any single index can be limited depending on the type of drought being analyzed, their primary advantages are the straightforward interpretation of their values and their role in drought contingency planning (Zargar et al. 2011, Zaniolo et al. 2018, Gonçalves et al. 2023).

As reservoirs are typically the only water source available in drylands (Lopes; Freitas, 2007), effective reservoir operation during periods of drought can mitigate the imbalance between planned demand and water availability through reasonable allocation. Known as hedging, this policy is driven by the idea of accepting minor present shortages to prevent critical future shortages and is implemented through rationing factors and rule curves (Luo *et al.*, 2023; Tu Ming-Yen *et al.*, 2008). Numerical approaches have been used to define optimal hedging rules, as the decision

[3] A paper based on the content of this chapter has been submitted to the *Water Resources Management* as Toné, A. J. de A., Cid, D. A. C., Costa, A. C., Toné, C. J. P. A., Barros, M. U. G. & Lima Neto, I. E. Adaptive hedging rules for a data-scarce dryland reservoir: integrating simple drought index, water user participation, and short-term hydrological monitoring, 2026.

to ration water must account for the complexity of water allocation in data-scarce regions. Optimization models proposed in the literature for drylands seek to identify optimal solutions by optimizing an objective function that either diminishes the maximum extent of a single-period deficit in the system or enhances the economic benefits. These solutions are normally hedging triggers or indicators of when and by how much to hedge. They are selected by comparing and ranking the system performance (i.e., reducing failures in satisfying demand) against the metrics of vulnerability, reliability, and resilience (Ashrafi; Dariane, 2017; Hong *et al.*, 2022; Neelakantan; Sasireka, 2015; Shih; ReVelle, 1995).

In this context, Cid *et al.* (2023) proposed a collaborative model that optimizes hedging rules to meet the rationing frequencies defined by water allocation agents. The numerical approach is based on the discrete hedging rule for a monthly reservoir proposed by Shih and ReVelle (1995) and does not assess monthly drought conditions using a drought index. Tributary flow series were obtained using a soil moisture accounting procedure that was adjusted via regionalization. This approach relies on the implicit assumption that catchments with similar characteristics exhibit similar hydrological behaviors. However, this assumption can be problematic because these catchments, although similar, are not identical (Guo *et al.*, 2021).

Chang *et al.* (2019) developed a numerical framework to determine the minimal reservoir water level required to satisfy water users during different drought events. This hedging trigger is useful for drought mitigation because future operating policies can be made suitable for specific emergence conditions. The model requires long-term meteorological and hydrological information for its applicability, particularly for inflow and drought assessments, as it integrates three drought indices (the streamflow drought index (SDI), standardized precipitation index (SPI), and relative moisture index (RMI)). This extensive data requirement can limit its use in data-scarce drylands (Kumar *et al.*, 2024). Similar to the framework of Cid e*t al.* (2023), in which water users define temporal allocation values based on reservoir storage conditions, the model also depends on previous optimal operation decisions to define the hedging policy.

Beshavard *et al.* (2022), on the other hand, proposed a numerical hedging model that calculates rationing ratios and rule curves linked to a warning storage based on a drought index (SDI). The model advances the state of the art by allowing earlier rationing responses to identified drought periods, and its application is simple in data-scarce areas. Notwithstanding, hedging policies are not only numerical issues, and they are more likely to be effective when the numerical model is united with a collaborative approach, where rationing ratios and acceptable risks are built together with water users (Sandoval-Solis *et al.*, 2013).

Numerous studies have employed multi-objective genetic algorithms, specifically the NSGA-II, to propose optimal operation rules. Ahmadianfar *et al.* (2017) utilized this method to define a hedging rule capable of gradually changing the rationing factors across operation zones in a dryland reservoir in southern Iran. In the Brazilian semi-arid region, Gomes *et al.* (2022) applied NSGA-II to design an operation rule that balances the stakeholder water supply with acceptable water quality standards. In another study, Karnatapu *et al.* (2020) derived optimal rules for a generic dryland reservoir in India, addressing both water supply and hydropower generation, and found better performance metrics with the proposed rules than with the standard operating policy. Based on these results, the authors suggested that NSGA-II is suitable for optimizing the operation rules in any reservoir with limited water availability.

Nevertheless, few studies have proposed an adaptive operational policy for a multi-use dryland reservoir that can deal with the rapid impacts of climate change on streamflow (Mujere *et al.*, 2022; Coulibaly *et al.*, 2025). Furthermore, existing operation policies rarely integrate water user participation, short-term field-measured hydrological monitoring, and early rationing based on a simple drought index simultaneously. Moreover, few approaches have proposed a hedging rule based on a water balance that considers river-aquifer dynamics, an important feature of dryland hydrology, coupled with a multi-objective genetic algorithm (NSGA-II) to find optimal decision variables. Thus, the objectives of this study are as follows: (1) to develop a hedging rule for a data-scarce dryland reservoir that seeks to balance the complexity of water allocation, drought assessment, and dryland hydrological processes while maintaining operational simplicity; (2) to evaluate the performance of the proposed hedging rules using simulated and measured inflow data; and (3) to provide insight into the requirements for the development of hedging rules in dryland reservoirs.

4.2 Methods

4.2.1 Study site

The study site is a multi-use reservoir in the Middle Jaguaribe sub-basin in the Brazilian semiarid region (Figure 22). The Castanhão Reservoir has a surface area of 325 km^2

and a storage capacity of 6.7 billion m^3, with depths exceeding 60 m in certain areas (Arantes *et al.*, 2025; Lima Neto, 2025). The catchment area is 45,309 km^2, and the rainfall regime is concentrated from January to May and only for a few days, ranging from 500 to 900 mm/year. During the dry season, potential evaporation rates throughout the year may exceed rainfall values by up to four times. These meteorological conditions, combined with shallow soils over crystalline geological formations, have resulted in extensive dry periods with minimal baseflow and streamflow within a few months (De Araújo; Medeiros, 2013; Raulino; Silveira; Lima Neto, 2021).

The Castanhão Reservoir experiences high variability in storage and inflow. For instance, following occasional floods in 2008, it reached 96% of its total storage capacity. However, during the subsequent severe drought (2012–2018), its volume plummeted to just 2%, significantly increasing water treatment costs. In recent years, the reservoir has recovered to more than 30% of its capacity (Lima Neto, 2025). No significant inflow, on the other hand, is observed during the dry season, such that reservoir management policies to satisfy human supply and other demands are defined during the rainy season (Molisani *et al.*, 2010).

Figure 22 - Location of the study site in the Brazilian semi-arid region. The river reach simulated by the river-aquifer model is indicated in red.

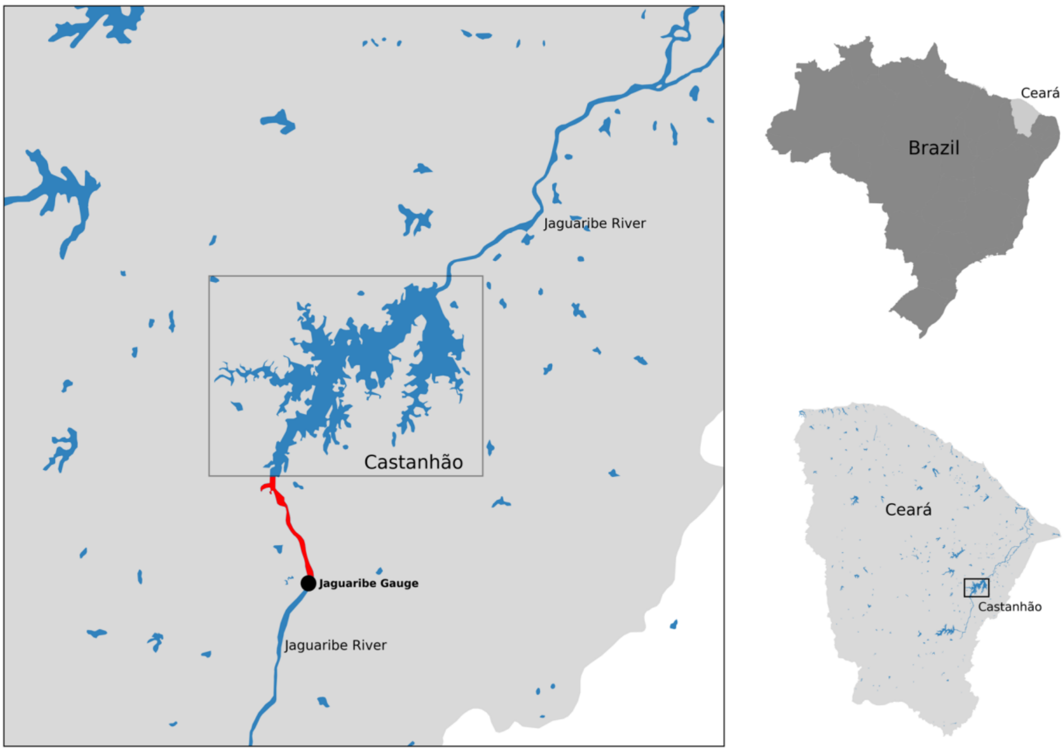

Source: prepared by the author.

4.2.2 Dataset

For the study site, monthly rainfall data were obtained from the National Hydrometeorological Network of ANA, and evaporation data were sourced from a regional study by ANA (2016) on dryland reservoirs in Brazil. This study also provides the total demand used in the operation model (D = 18.85 m^3/s).

The elevation-area-volume curve of the Castanhão Reservoir was obtained from the Ceará Hydrological Portal of FUNCEME. Recognizing that improved inflow data can enhance hedging rules (Neelakantan; Sasireka, 2015), we conducted field measurements to obtain these data. In the first half of 2021, the inflow at the entrance of the Castanhão Reservoir was measured using a SonTek RiverSurveyor M9 ADCP. Because of technical difficulties at this site, we could not perform daily measurements. Consequently, in 2022, monitoring was relocated to a gauge approximately 21 km upstream of the Jaguaribe River. At this new location, the ANA provided daily inflow and river stage data, which were used to forecast the inflow at the Castanhão Reservoir entrance. The daily flow volume was defined as the total 24-hour discharge derived from the ANA records. We also used monthly inflow data generated for the study site using a soil moisture accounting procedure (SMAP) and later adjusted via regionalization by UFC and COGERH (2013) to propose the hedging policies. This inflow series data spans the period from January 1912 to December 2012.

We estimated the streamflow into the study site during the first semester of 2022 using the river routing equation proposed by Toné *et al.* (2025) for dryland and data-scarce catchments. This numerical model requires few parameters and estimates river-aquifer dynamics, such as aquifer recharge and hyporheic flow. The outflow from a river reach is calculated as follows:

$$O_{t+\Delta t} = \frac{1}{1-X}\left(\frac{V_t}{K}\right)^{\frac{1}{\gamma m}} - \frac{X \cdot Q_t + \pi + \mu + \Omega + \delta}{1-X} \quad (4.1)$$

Where $O_{t+\Delta t}$ is the outflow (m^3/s), V_t is the volume (m^3), X is a weighting factor, K is the storage constant (s), and γ and m are calibrated exponents. According to Toné *et al.* (2025), for the 21 km river reach between the Jaguaribe gauge and the study site, exponent m is set to 1.6. Exponent γ is set to 0.9 when the river stage is equal to or below the mean river head at the measurement location, and 0.5 when it is higher.

Additionally, the model accounts for direct in-river flux (π), sub-catchment runoff (μ), and river-aquifer interaction (Ω), with all terms expressed in m^3/s. A detailed description of the steps required to calculate each term in equation 4.1 are provided in Chapter 3.

In addition to the previously described data, equation 4.1 requires the determination of geometric, sub-catchment, and hydrogeological parameters. The geometric parameters were derived as follows: the channel length, river slope, and sub-catchment area were obtained from the Copernicus GLO-30 digital elevation model (DEM) using the QGIS raster analysis tool. The other parameters (perimeter, area, hydraulic radius, and top width) were derived from river stage measurements, assuming a triangular cross-section of the river. We assumed a constant top width because no flow beyond the main channel was considered in this study. The sub-catchment curve number (assuming type 2 soil moisture) was provided by ANA (2018). The hydrogeological parameters were obtained separately. The aquifer width and hydraulic conductivity of the alluvium were obtained from surveys conducted by CPRM (2014, 2015). The hydraulic conductivity of the riverbed was calculated using Hazen's method, which was applied to the riverbed grain size data from Wiegand (2009) for the Jaguaribe River.

4.2.3 Drought index

This study used the SPI, which is commonly adopted in operational models in drylands. The SPI is calculated by dividing the difference between precipitation and its long-term mean by the standard deviation (Faye, 2022). The criteria for identifying drought events are SPI values that are continuously negative and equal to or below - 1.0 for any time scale (McKee; Doesken; Kleist, 1993). A major advantage of the index is that it relies only on precipitation data and can be calculated for different timescales, allowing for adaptable drought analysis and hydrological monitoring (Zargar *et al.*, 2011).

To implement adaptive reservoir operations on short time scales, it is necessary to address the rapid and significant impact of climate change on streamflow in drylands (Saedi *et al.*, 2022; Swain *et al.*, 2020; Werede *et al.*, 2024). Since intermittent streamflow patterns are best characterized by SPI values at the 2–6-month scale (Mishra; Desai, 2005), this study calculated the SPI on a 3-month time scale (SPI3) using historical precipitation records from the study site, as described in the Dataset section. Although evaporation driven by higher temperatures plays an important role in trends toward drier conditions, suggesting the utility of drought indices that consider potential evapotranspiration, such as the Standardized Precipitation Evapotranspiration Index (SPEI), the SPI3 and SPEI3 showed significant agreement at the study site based on historical data from 1980 to 2019 (Tomasella *et al.*, 2023).

However, De Araújo Júnior *et al.* 2020 observed that the SPI failed to capture reservoir storage fluctuations in another reservoir in the Brazilian semiarid region because of the time lag between precipitation and water volume variations. Nevertheless, other studies have suggested its utility in this region. Recently, Gonçalves *et al.* (2023) evaluated several drought indices for the Castanhão Reservoir based on six criteria: treatability, robustness, transparency, sophistication, dimensionality, and extensibility. Their findings indicated that the SPI outperformed other indices by identifying more drought events. Given the rapid impact of meteorological droughts on surface water in drylands (Ahana *et al.*, 2025), we selected the SPI to identify these events. The rationale is to start rationing earlier, owing to the application of a drought index, than conventional operation rules that rely solely on the actual reservoir storage. The SPI classification adapted to the study site is presented in Table 9.

Table 9 - SPI classification for water management at the study site.

SPI values	Classification
≥ 2.00	Extreme rainfall
1.49 to 1.99	Severe rainfall
0.99 to 1.49	Moderate rainfall
0.49 to 0.99	Weak rainfall
-0.49 to 0.49	Almost normal
-0.99 to -0.49	Mild drought
-1.49 to -1.00	Moderate drought
-1.99 to -1.50	Severe drought
≤ -2.00	Extreme drought

Source: Santos (2020); Gonçalves *et al.* (2023).

4.2.4 Operation rules

The operating rules are defined based on the reservoir storage and rationing ratios established by the water allocation agents. These ratios were established through a stakeholder consultation process conducted by Cid *et al.* (2023), wherein participants defined the values for the Castanhão Reservoir corresponding to various drought scenarios. The resulting consensus values are listed in Table 10. In this study, each drought condition will be assessed using SPI values (Table 9). One of the conditions to be optimized is that the operation rules must meet the consensus rationing ratios for each drought state (Table 10); otherwise, there will be a failure in the system performance.

Table 10 - Stakeholder consensus on rationing ratios at the study site under different drought conditions.

Castanhão	**Drought state**				
	Almost normal	Mild drought	Moderate drought	Severe drought	Extreme drought
SPI3	> -0.49	-0.99 to -0.49	-1.49 to -1.00	-1.99 to -1.50	≤ -2.00
Rationing ratios	0.00	0.05	0.15	0.50	0.95

Source: prepared by the author.

Reservoir storage is divided into three zones defined by monthly upper (S1) and lower (S2) trigger volumes. Typically, these thresholds determine the water allocation ratio based on the storage and inflow at the beginning of each operational period. To address the impacts of climate change in drylands, we adopted a monthly dynamic warning storage (WS_t) proposed by Beshavard *et al.* (2022). In this study, this parameter integrates the 3-month SPI to enable earlier rationing measures. Specifically, this mechanism ensures that rationing is triggered if the SPI3 indicates a drought condition, even when the observed reservoir storage (S_t) remains high.

$$WS_t = S_t \cdot (1 + \alpha_3 \cdot SPI3) \quad (4.2)$$

In other words, when the SPI3 is positive, the warning storage remains equal to the current monthly storage. However, when SPI3 is negative, the warning storage is effectively reduced by a factor derived from the product of the SPI3 value and an optimized monthly coefficient α_3 ranging from 0 to 1 (see next section). Consequently, even if the actual reservoir storage is near or above the upper S1 trigger, the reduced warning storage forces early rationing to mitigate the impact of future droughts on the water supply.

In this study, we compare two water allocation rules. For both, the total demand considered encompasses priority demands (human and livestock consumption) and non-priority demands (irrigation). This total demand is adjusted using stakeholder ratios depending on the drought conditions identified by SPI3 values (D'= Table 10 factors • D). Rule 1 is a standard three-zone policy. If the WS (equation 4.2) and inflow are above the upper trigger (S1), no rationing is applied to the demand. If it is between the S1 and S2 triggers, the demand is rationed using a fixed coefficient, α_1. If it is below the lower trigger (S2), demand is rationed by a fixed coefficient α_2 (eqs. 4.3-4.5), as follows:

$$\text{If } S_1 \leq WS_t + Q_t \text{ then } R_t = D' \tag{4.3}$$

$$\text{If } S_2 \leq WS_t + Q_t < S_1 \text{ then } R_t = \alpha_1 \bullet D' \tag{4.4}$$

$$\text{If } WS_t + Q_t < S_2 \text{ then } R_t = \alpha_2 \bullet D' \tag{4.5}$$

Rule 2 is similar to Rule 1 and was adapted from Cid *et al.* (2023) to consider WS (equation 4.2). It also releases D' when the warning storage (equation 1) and inflow exceed S1 (equation 4.6). However, in the other two zones, both rationing coefficients (α_1 and α_2) can be used to calculate water allocation, and coefficient β is considered to reduce R_t when the SPI3 value is above -0.49 (from "almost normal" to "extreme rainfall" conditions) (equation 4.7).

$$\text{If } S_1 \leq WS_t + Q_t \text{ then } R_t = D' \tag{4.6}$$

$$\text{If } S_1 > WS_t + Q_t \text{ then } R_t = \min(D'; D \bullet (1+\beta) \bullet (1 - y_{1,t} \bullet \alpha_1 - y_{2,t} \bullet (\alpha_2 - \alpha_1))) \tag{4.7}$$

Where Q_t is the monthly inflow (m^3), R_t is the monthly water release (m^3), and β is a monthly coefficient, respectively. The variable $y_{1,t}$ is a binary indicator equal to 1 if the warning storage (WS_t) is below trigger S1 during month t, and 0 otherwise; similarly, $y_{2,t}$ is equal to 1 if WS_t is below trigger S2, and 0 otherwise.

To propose an operating curve that divides the reservoir storage into three zones, we used a multiobjective genetic algorithm, NSGA-II, to calculate the decision variables (Deb *et al.*, 2002) (see next section). This tool was selected based on its demonstrated effectiveness in estimating optimal monthly operational rules in previous studies (Aboutalebi Mahyar; Bozorg Haddad Omid; Loáiciga Hugo A., 2015; Chang; Chen; Chang, 2005; Gomes; Maia; Medeiros, 2022). These variables were calculated using an inflow dataset that included the historical period from the start of the Castanhão Reservoir's operation until 2012 (SMAP-estimated) and inflow data from the rainy seasons in the first halves of 2021 and 2022 (see Dataset section). The genetic algorithm estimated two sets of optimized decision values: the first, considering equations 4.3-4.5 for monthly water release (R1), and the second, considering equations 4.6-4.7 for monthly water release (R2).

The necessary restrictions for the operation rules are as follows: for reservoir storage, the condition is $Smin \leq S2 < S1 \leq Smax$, where Smax is the maximum storage volume of the Castanhão reservoir (6700 hm^3) and Smin is the minimum volume required to meet priority demand (58.1 hm^3) (ANA, 2016); for the rationing coefficients, the constraints are $0 < \alpha_2 < \alpha_1 < 1$ and $0 < \beta < 1$. An additional constraint is introduced to prevent the S1 and S2 trigger values from being too close, which is necessary for effective rule operation. This constraint is defined as $S1 \geq (1+\gamma) \cdot S2$, with the coefficient γ restricted to the range [0.3, 1.0].

4.2.5 Operation simulation

To determine the reservoir storage (S_t) at the end of each monthly time step (t), we applied the following water balance equation:

$$S_{t+1} = S_t - E_t + Q_t - Spill_t - Inf_t - R_t \qquad (4.8)$$

The variables E_t, Inf_t, and $Spill_t$ represent the monthly evaporation, monthly infiltration, and spill volumes (m^3), respectively. The spill volume is determined as follows: if the storage at the end of the month, S_{t+1}, is greater than the maximum capacity, Smax, then the spill is the excess volume ($Spill_t = S_{t+1} - Smax$). Otherwise, $Spill_t = 0$. Monthly infiltration was considered zero in the study site.

With the rationing ratios already established in consultation with water agents ("how much to hedge"), the focus now shifts to optimizing the operating rules. This optimization must provide simple rules for operators to implement, but these rules must also be robust enough to handle the impacts of climate change on water supply deficits (Neelakantan; Sasireka, 2015; Raulino; Silveira; Lima Neto, 2022; Şen, 2021). The first goal, robustness against climate change, is achieved using storage triggers and warning storage linked to the SPI3 drought index, as described previously. This mechanism determines "when to hedge" to conserve water and reduce socioeconomic impacts. The second goal, simplicity, is intended to facilitate the development and execution of drought preparedness plans.

In seeking to optimize the operating rules, we aimed to minimize the total water supply deficit. This was achieved by minimizing the modified shortage index (MSI) (equation 4.9), proposed by Hsu and Cheng (2002) for a region experiencing extreme hydrological variability. For this optimization, we employed NSGA-II to determine the optimal values for 39 decision variables, encoded as a single chromosome string. These variables were the 24 monthly reservoir triggers (S1 and S2), 12 monthly α_3 coefficients for the warning storage calculation, and three rationing coefficients (α_1, α_2, and β).

NSGA-II generates a random population of size N. Following the selection, crossover, and mutation processes, the algorithm categorizes different individuals according to their level of non-domination within the population. The operation is repeated until a defined stopping criterion is met. To minimize the computational time required for simulation, we set this criterion to 100 generations. Although this implies that the calculated decision variables may not guarantee the global optimum, they provide satisfactory solutions that meet the objectives and restrictions defined in this study. In each generation, the objective function for each individual was calculated, and the decision variables were evaluated against the restrictions and performance metrics (see the next section). This iterative process continued until the final generation, which determined the optimal values for the decision variables.

$$\mathrm{OBJ} = \mathrm{MSI} = \frac{100}{\mathrm{n}} \cdot \sum_{\mathrm{t}=1}^{\mathrm{n}} \left(\frac{\mathrm{TS_t}}{\mathrm{TD_t}}\right)^2 \quad (4.9)$$

Where n is the total number of simulated months, TS_t is the shortage during month t (the difference between D’ and monthly water release), and TD_t is the D’ demand during month t.

4.2.6 Evaluation of operation rules

We evaluated the effectiveness of the hedging rules using the following performance measures: time-based reliability, volumetric reliability, resilience, and vulnerability. These indicators are described in detail by McMahon *et al.* (2006) and are presented as follows.

(7) Time-based reliability (REL_t): For a monthly simulation, it is the number of months in which the total demand is fully satisfied (N_s) divided by the total amount of months (n). The REL_t value is restricted to the range |0.0,1.0].

$$\mathrm{REL_t} = \frac{\mathrm{N_s}}{\mathrm{n}} \tag{4.10}$$

(8) Volumetric reliability (REL_v): Similarly, this is the volume of water transferred to meet demand, divided by the amount of volume of water demanded over the simulation period. The REL_v value is also restricted to the range |0.0,1.0].

$$\mathrm{REL_v} = 1 - \frac{\sum_{i=1}^{n}(\mathrm{TS_i})}{\sum_{i=1}^{n}\mathrm{D_i}} \tag{4.11}$$

(9) Resilience (RES): This indicates the speed at which a reservoir system recovers from a failure state. It is calculated as the number of consecutive failure events (f_s) divided by the total number of months in which the system was in a state of failure (f_d). The RES value is restricted to the range [0.0,1.0].

$$\mathrm{RES} = \frac{\mathrm{f_s}}{\mathrm{f_d}} \tag{4.12}$$

(10) Vulnerability (VUL): It is an indicator of the severity of failure in volumetric terms during its occurrence. The VUL value is also restricted to the range |0.0,1.0].

$$\mathrm{VUL} = \frac{\sum_{i=1}^{f_d}\frac{\mathrm{TS_i}}{\mathrm{D_i}}}{\mathrm{f_d}} \tag{4.13}$$

The genetic algorithm was constrained to find solutions (decision variables) that satisfy the following performance criteria: $REL_{t,v} \geq 0.95$ and $VUL \leq 0.1$, as the RES value requires careful interpretation. Figure 23 illustrates the methodological flowchart of this study, which is valid for each water allocation rule.

Figure 23 - Methodological flowchart applied in the definition of the hedging rules for the Castanhão Reservoir.

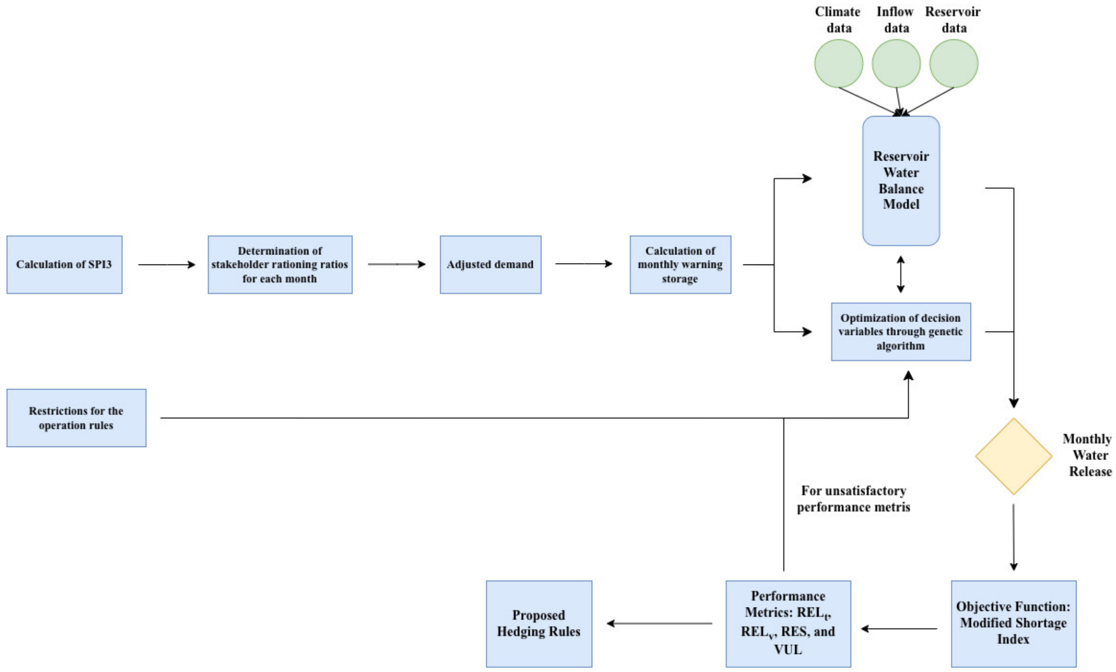

Source: prepared by the author.

4.3 Results

The SPI3 values required to calculate the warning storage were compiled for the 228-month period from the start of the Castanhão Reservoir's operation (January 2004) to the measurements at the Jaguaribe River gauge (2022) (Figure 24). In this timeframe, while annual rainfall varied widely (366.2 to 2438.1 mm), SPI3 values were predominantly negative (67% of the time), with 47% of values falling below -0.5 (mild to extreme drought). This was most evident during the 2012–2016 drought, the region's most severe in the last century, when reservoir storage experienced declines of up to 80% (FUNCEME, 2026), and 68% of SPI3 values were below -0.5. Critically, the SPI3 values in our study period showed a significant decreasing trend (P-value < 0.009) compared to the two earlier periods (1985–2003 and 1966–1984), which is consistent with the global trend of increasing drought frequency in drylands (Hazbavi *et al.*, 2018; Satoh *et al.*, 2022).

Figure 24 - Monthly SPI3 from the beginning of Castanhão reservoir operation until 2022.

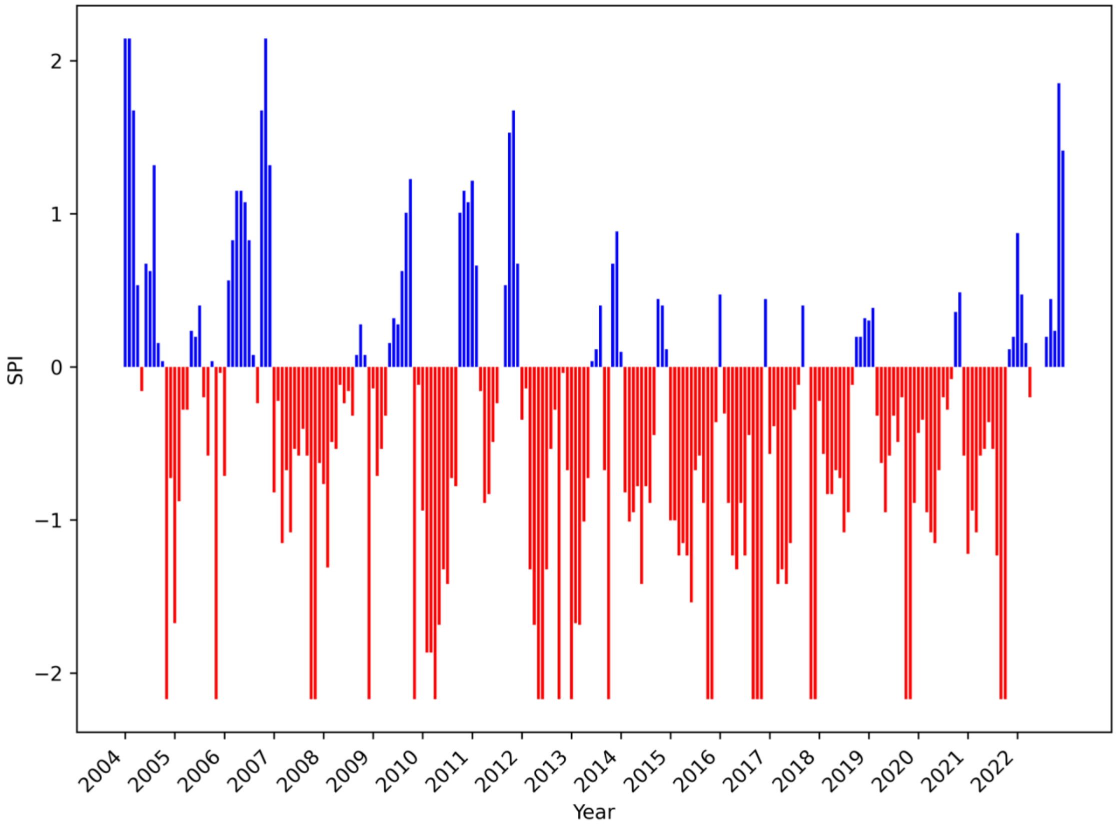

Source: prepared by the author.

Regarding streamflow, the maximum observed value in 2021 was 31.81 m³/s at the entrance of the Castanhão reservoir and 483.19 m³/s at the Jaguaribe gauge in 2022. The inflow values estimated with SMAP (2004-2012) varied from 0 to 475 m³/s, whereas those from equation 4.1 (2022) varied from 0 to 561.77 m³/s. These four series are shown in Figure 25, and their values are similar to those observed in previous studies on the Jaguaribe River (Costa; Bronstert; De Araújo, 2012). Figure 25b indicates greater peak flows at the end of the 21 km river reach compared with the observed streamflow at its beginning. This suggests that groundwater fluxes (such as hyporheic flow) and sub-catchment runoff contribute to the water balance of the Castanhão Reservoir.

Figure 25 - Inflow data for optimizing hedging rules in 2021 (a), 2022 (b) and 2004-2012 (c).

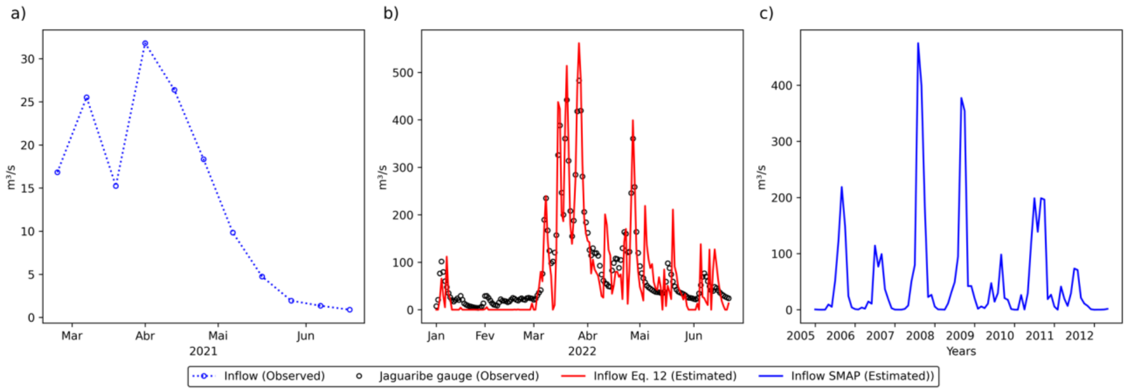

Source: prepared by the author.

Table 11 shows the optimized α_3 values for decision variable sets 1 and 2, respectively. This coefficient is used to calculate the warning storage, which determines the monthly water release.

Table 11 - Optimized α_3 values for warning storage estimation in each set of decision variables.

	Months											
Sets	Jan	Feb	Mar	Apr	May	Jun	Jul	Aug	Sep	Oct	Nov	Dec
1	0.20	0.66	0.53	0.84	0.31	0.99	0.32	0.52	0.52	0.91	0.95	0.45
2	0.29	0.36	0.45	0.35	0.29	0.30	0.56	0.02	0.31	0.42	0.23	0.32

Source: prepared by the author.

Throughout the simulation, the monthly warning storage was calculated using α_3, SPI3, and S_t (equation 4.8) and then compared against the optimized triggers S1 and S2. This SPI3-based mechanism enabled early rationing to mitigate the impacts of future droughts. This effect is visualized in Figure 26, which plots the mean monthly WS against the S1 and S2 triggers for the 2004–2012 SMAP inflow period. Figures 26a-b illustrate WS values falling below the S1 trigger, even during the rainy season. The water rationing coefficients derived from the optimization were $\alpha_1 = 0.96$ and $\alpha_2 = 0.61$ for set 1, and $\alpha_1 = 0.13$, $\alpha_2 = 0.12$, and $\beta = 0.14$ for set 2, respectively.

Four performance parameters (REL_t, REL_v, RES, and VUL) were used to evaluate the drought-informed operating rules (set 1 and set 2) for the reservoir. Using the SMAP inflow data, the simulation indicated satisfactory performance for both rules, which was attributed to the water transfer volumes (R1 and R2) based on the optimized S1/S2 triggers and monthly WS variation. Specifically, set 1 experienced four months of failure, yielding REL_t = 0.96, REL_v = 0.99, RES = 0, and VUL = 0.10; set 2 performed with only one failure, resulting in REL_t = 0.98, REL_v = 0.99, RES = 0, and VUL = 0.08. In the first set, the objective function (equation 4.9) was 0.096; for the second set, it was 0.008. Figure 27 compares the water releases from R1 and R2 with the total demand, alongside the resulting variation in the storage volume for each set. The monthly variations in water demand (also shown in the figure) result from the application of the stakeholder rationing ratios (Table 10), which are selected based on the SPI3 value for each month (D'). There was no significant variation between the storage volumes in either set, as these values were significantly greater than the water release.

Figure 26 - Comparison between warning storage (WS) and hedging triggers (S1 and S2) for decision variables sets 1 (a) and 2 (b).

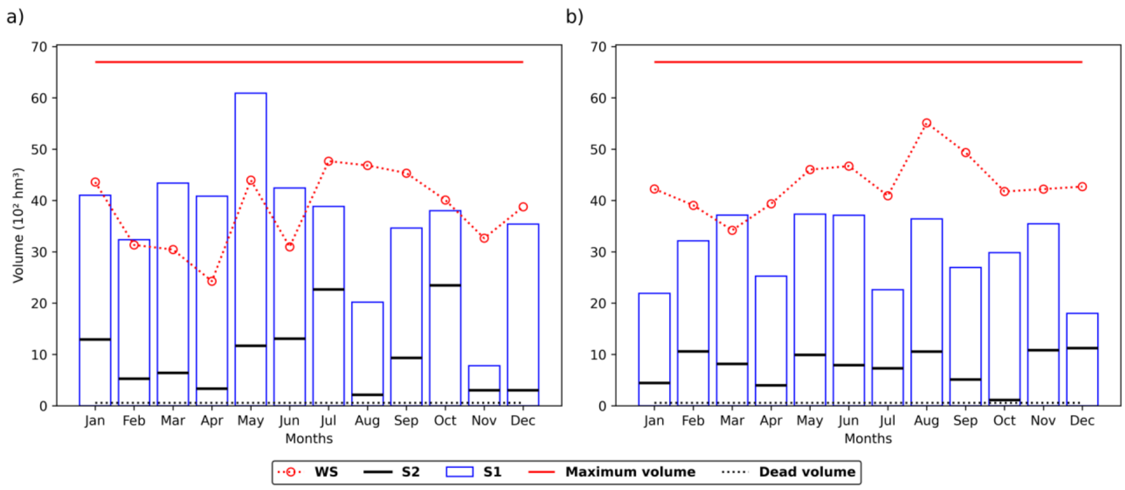

Source: prepared by the author.

Figure 27 - Comparison of water transfers for decision sets 1 (R1) and 2 (R2) with the adjusted total demand (D') (a) and the resulting storage volume variation for both sets (b).

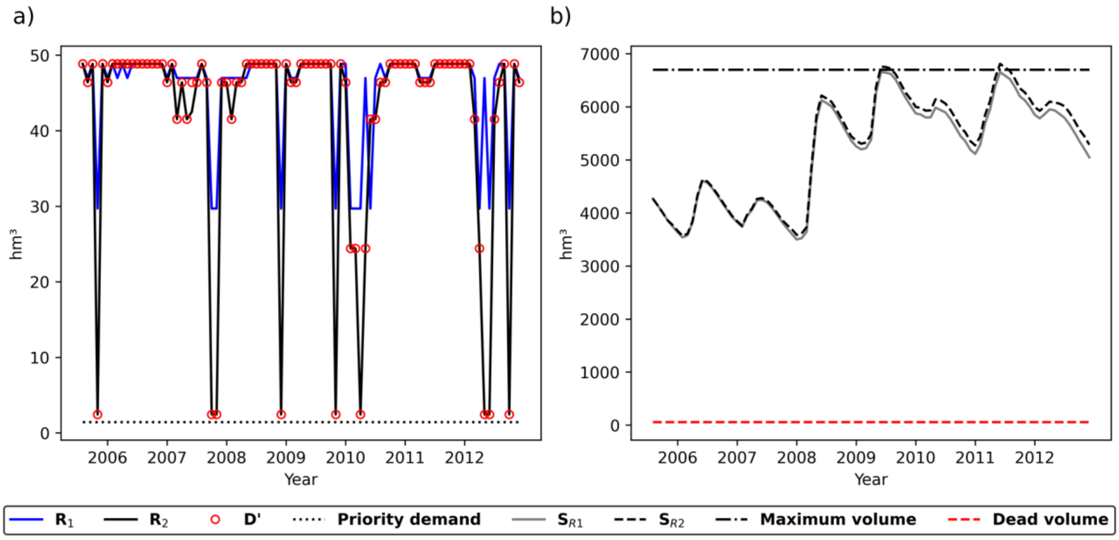

Source: prepared by the author.

When applied to the measured inflow data, the operating rules produced performance metrics that differed significantly based on the water transfer equation (R1 and R2) and drought index. The SPI3 values between March and June of 2021 were consistently negative (-1.08, -0.58, -0.54, and -0.36, respectively), corresponding to moderate to mild drought (Table 9), whereas they were positive in almost all the first half of 2022 and negative only in April (-0.20). In 2021 (Figure 28a-b), the continuous drought pushed the warning storage below the S2 trigger, which significantly reduced the R1 value, whereas the R2 transfer was able to maintain itself above the required demand in March and June (Figure 29a). Consequently, R1 experienced system failures in all months except April, even when the rationing ratios were applied to the total demand, whereas R2 experienced two failures. This exception was possible because the warning storage was slightly higher than the S2 trigger. The performance metrics for set 1 were $REL_t = 0.25$, $REL_v = 0.74$, $RES = 0.67$, and $VUL = 0.35$. Set 2 yielded $REL_t = 0.50$, $REL_v = 0.96$, $RES = 0.5$, and $VUL = 0.08$. The objective function was 9.109 for set 1 and 0.310 for set 2.

In 2022, the consistently positive SPI3 values maintained a constant monthly demand throughout the first half of the year (Figure 29b). These precipitation conditions kept the warning storage above the S2 trigger during the simulation, except in January for R1 and February for R2 (Figure 28c-d). The system operation with set 1 decision variables (R1) failed during the entire simulation period, even though R1 values were close to the demand required, whereas there was no failure with set 2 parameters (R2). This condition improved the performance metrics for set 2 compared to those in 2021. For set 2, REL_t = 1.0 and REL_v = 1.0, and it was not possible to calculate RES and VUL. For set 1, failure in all months dropped REL_t to zero; the other metrics were REL_v = 0.90, RES = 0.83, and VUL = 0.10. The objective function was 2.684 for set 1 and 0.002 for set 2.

Figure 28 - Comparison of warning storage (WS) against hedging triggers (S1 and S2) for both decision variable sets. Subplots show: (a) set 1 in 2021; (b) set 2 in 2021; (c) set 1 in 2022; and (d) set 2 in 2022.

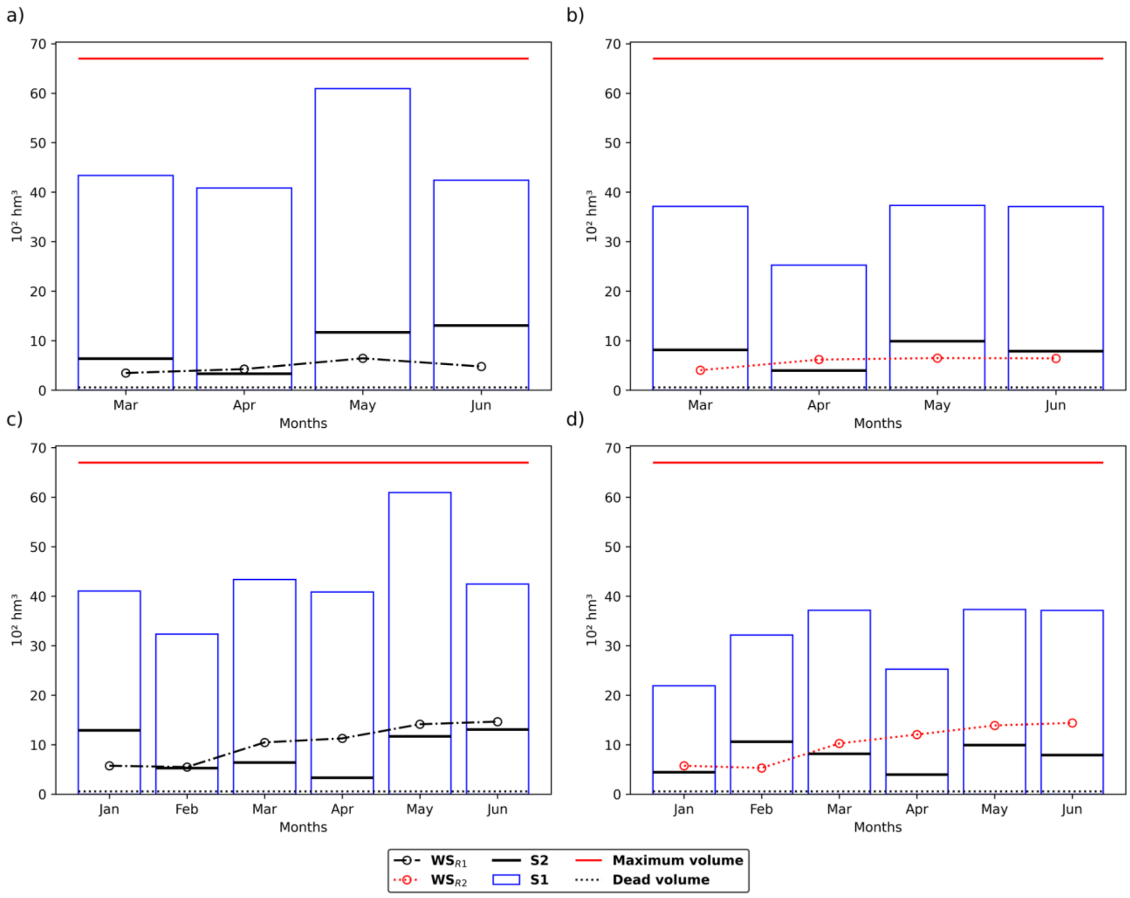

Source: prepared by the author.

Figure 29 - Comparison of water transfers for decision sets 1 (R1) and 2 (R2) with the adjusted total demand (D') in 2021 (a) and 2022 (b).

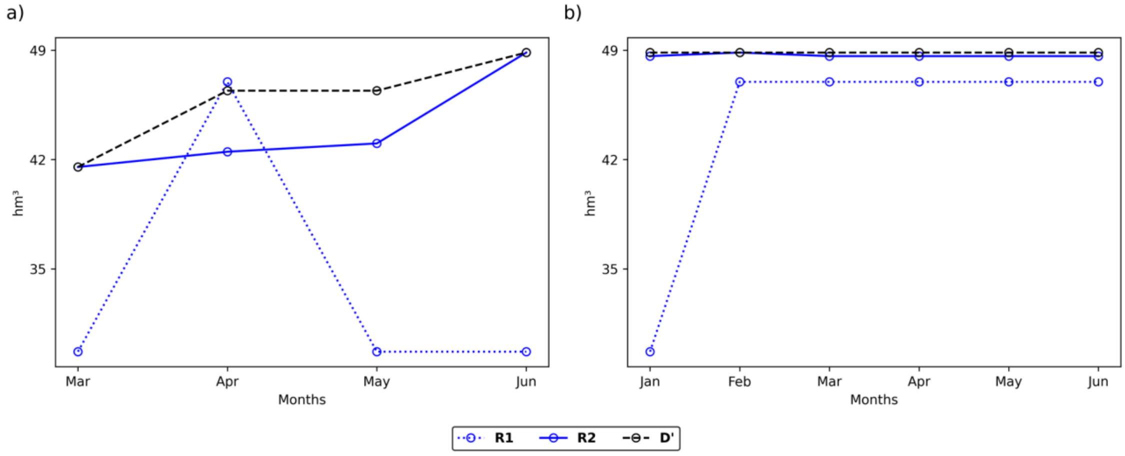

Source: prepared by the author.

4.4 Discussion

The performance metrics of the reservoir operation demonstrated the effectiveness of the proposed hedging rules from the start of the Castanhão operation to 2012. They successfully satisfied the water demand while adhering to the stakeholders' rationing ratio requirements (Table 10). This effectiveness was achieved despite the model simplicity and the prevalence of drought conditions (Figure 24), which ranged from mild to extreme during most of the study period (Table 9). Nevertheless, the hedging policies obtained have certain limitations. First, they were defined using estimated inflow data, which were adjusted via regionalization. Second, water balance calculations (equation 4.8) suffer from uncertainties due to data scarcity and technical difficulties with on-site measurements, although we did not observe any significant errors.

During the entire simulation period, both water transfer proposals, using their respective optimized decision variables, satisfied the priority demand (human and livestock consumption) (Figure 27). Decreasing the total demand (which encompasses agricultural uses) at the study site will not impose failures in the proposed hedging rules. Thus, the recent decision from COGERH and water users to allocate 17 m³/s from the Castanhão reservoir during the second half of 2025 would not be seen as a risk for the proposed rules (COGERH, 2025), as they would inherently protect this supply. The analysis of set 1 revealed a paradoxical behavior. Warning storage remained below the S1 trigger for almost the entire rainy season (Figure 26), which is a conservative stance that may improve assurance during severe droughts (Gomes; Maia; Medeiros, 2022). Despite this, in 45% of the simulations (SMAP inflow), the R1 transfers were greater than the stakeholder-adjusted total demand (D'), indicating an inefficiency. Thus, the rules (equations 4.4-4.5) require adjustments. They must be modified to enforce the maximum water transfer at the adjusted demand to prevent over-delivery, similar to equation 4.7.

In contrast, the decision variables for set 2 produced a warning storage that was consistently higher than that of set 1, remaining above the S1 and S2 triggers for most of the simulations (Figure 26). This can be explained by two factors: first, for SPI3 values above -0.49, R2 transfers are constrained to the minimum of D' and the total demand multiplied by a reduction factor (Figure 27). This resulted in smaller monthly water releases, thus conserving reservoir storage and increasing WS. Furthermore, the α_3 values for set 2 were consistently lower than those for set 1 (Table 11). Because α_3 is applied when SPI3 is negative, a lower α_3 value reduces the drought penalty. This resulted in an increase in the $(1 + \alpha_3 \bullet \text{SPI3})$ factor, leading to a higher WS estimation.

In contrast, when evaluated using the on-site (measured) inflow data, the proposed hedging rules failed to satisfy water demand under one set of decision variables during the simulated months in 2021 and 2022. A key limitation is that the SMAP inflow data presupposes hydrological similarities between catchments (Gui *et al.*, 2019). This assumption is problematic because similarity does not ensure identical behavior, potentially leading to overestimated inflows. This may be evident in 2021, where Figure 25a shows that the measured inflows were significantly lower than the SMAP estimated inflows (Figure 25c). This overestimation by SMAP likely explains why the WS values in 2021 were so low (often below the S2 trigger) (Figure 28a-b). In 2022, however, the measured inflow and inflow estimated by equation 4.1 were in strong agreement (Figure 25b) and were similar to the SMAP values (Figure 25c). This improved alignment in 2022 may be attributed to favorable hydrological conditions (consistently positive SPI3 values) during that period, which contributed to higher WS values (above the S2 trigger) (Figure 28c-d) (Hazbavi *et al.*, 2018).

In 2021, the warning storage dropping below the S2 trigger pushed R1 to significantly low values (due to the α_2 factor), although these values were still above the priority demand requirements (Figure 29). Mild to extreme drought conditions also pushed R2 values below the D' requirements, but for 50% of the simulated period. In 2022, even with higher WS values (between S1 and S2) and better precipitation conditions, R1 failed to satisfy water demand because of its simplicity and sole dependence on the α_1 factor. With R2 transfers, on the other hand, there was no failure during the entire simulation. This finding suggests that for adaptive hedging in data-scarce drylands, the calculation method (i.e., the rule itself) is more critical than the disposal of on-site inflow measurements. Hence, operating rules optimized using simulated data (e.g., regionalization or equation 4.1) may be effective in satisfying water demands and stakeholder requirements, even when integrated with a simple drought index and in the presence of data uncertainties.

Previous hydrological modeling supports these conclusions. For instance, Rottler *et al.* (2024), when developing a hydrological forecasting system for the study site based on satellite monitoring and hydrological modeling, observed that it was possible to estimate storage volumes for all reservoirs in Ceará. This was achievable even for reservoirs with no prior information, despite uncertainties arising from the model components. Similarly, Karamouz and Araghinejad (2008) proposed hedging rules for long-term decisions in a dryland reservoir in Iran based on estimated water availability, drought indices, and inflow forecasts. They demonstrated that this operational framework significantly mitigated drought damage in the study area.

4.5 Conclusions

This study proposed a simple hedging rule for a data-scarce dryland that is adaptive to drought conditions and incorporates the rationing ratio requirements defined by stakeholders. By developing optimized rules using estimated inflow and testing them against on-site measurements, this study suggests that hedging rules can be effectively applied even in the face of data uncertainty. The principal findings are summarized as follows:

- Drought impacts can be mitigated by triggering early water shortages using a dynamic warning storage that considers both reservoir storage and a drought index (SPI3).
- For adaptive hedging in data-scarce drylands, the method used to define the operating rule is more critical than the disposal of on-site inflow data.

- The SPI3 index proved to be an effective input for the operating rules, demonstrating its effectiveness in guiding water transfers to satisfy the demands.

4.6 Funding

The present study was supported through the National Council for Scientific and Technological Development – CNPq (#307680/2023-1) and the Brazilian Federal Agency for Support and Evaluation of Graduate Education – CAPES (#88887.007807/2024-00).

5 GENERAL CONCLUSIONS AND FUTURE WORK

This thesis contributes to a more accurate quantification of the water balance for key hydrological processes in data-scarce drylands, providing valuable tools for regions that require viable management solutions. This study demonstrated that, grounded in a conceptual framework of river–aquifer interactions in large dryland rivers, the proposed numerical model creates accurate estimates of river and groundwater flow. Crucially, it achieves this using a parsimonious modeling approach that requires minimal calibration. Furthermore, it also demonstrated that a hedging model integrating river-aquifer modeling and drought assessment, despite data uncertainties, is capable of maintaining system vulnerability below 10% with both simulated and measured inflow data.

Three objectives were pursued: (1) to develop a conceptual model of the dominant river-aquifer dynamics at the basin scale for a dryland river; (2) to construct a parsimonious numerical model for simulating these hydrological processes; and (3) to establish a hedging rule for data-scarce dryland reservoirs that balances allocation complexity, drought assessment, and hydrological dynamics while maintaining operational simplicity. Chapters 2 to 4 address these objectives as independent papers, structured sequentially, so that each study builds upon the findings of the preceding one.

In Chapter 2, the spatiotemporal river–aquifer interactions in a large dryland river with high anthropogenic intervention were analyzed. Water level and flow rate measurements were performed and analyzed together with secondary data on hydrogeology, water use, and satellite images. The average transmission losses ranged from approximately 12 to 28% of the river inflow, while the transmission gains ranged from 10 to 34%. Transmission losses occurred at the beginning of the rainy season (rainfall $\leq$ 10 mm/d), whereas transmission gains were preponderant after intense rainfall events (> 20 mm/d). A direct relationship between the transmission losses/gains and river inflow was also observed. Linear equations were adjusted to estimate the order of magnitude of the transmission losses ($R^2 > 0.85$) and gains ($R^2 > 0.60$). The transmission loss equation was validated for rivers in similar regions ($R^2 \approx 0.85$). A conceptual model was proposed to describe river–aquifer interactions in large dryland rivers.

In Chapter 3, considering that water security relies on accurately representing hydrological processes in river-aquifer dynamics, including aquifer recharge driven by rainfall, hyporheic flow, and lateral tributary inflow, and that river–aquifer studies often overlook these processes, this paper accurately calculated these processes in a data-scarce region at scales relevant to water management using a parsimonious numerical model. The model performance measures (Kling-Gupta efficiency, Nash–Sutcliffe efficiency, and percent bias) showed that it effectively estimated river and groundwater flow using a simple modeling approach, requiring only minimal calibration (three parameters). Notably, the data required for the model are often available in regions with scarce data. Sensitivity analysis of the simplified model parameters showed that riverbed hydraulic conductivity and aquifer width significantly affected outflow in data-scarce environments. Hyporheic flow is crucial for the water balance in dryland rivers. In contrast, subcatchment runoff demonstrated minimal influence compared to inflow and groundwater fluxes, suggesting a greater dependence on river volume and stage than on intraseasonal rainfall.

In Chapter 4, this paper developed a numerical hedging model for a dryland reservoir featuring an early rationing system based on the identification of drought events is presented. Key advantages include the optimization of decision variables (trigger volumes and rationing coefficients) using a genetic algorithm (NSGA-II), integration of water user participation, water allocation connected with drought assessments through a simple drought index, streamflow prediction based on river-aquifer dynamics (Chapter 3), and the use of short-term field-measured hydrological data. The results show that the proposed hedging rule maintained system vulnerability below 10% using both simulated and measured inflow data, and the objective function (the modified shortage index) was successfully optimized, even when early rationing occurred during the rainy season. The quantitative analysis suggests that for adaptive hedging in data-scarce drylands, the calculation method (the rule itself) is more critical than the availability of on-site inflow measurements. Consequently, operating rules for a dryland reservoir optimized using simulated data may be effective in satisfying water demands and stakeholder requirements, even when integrated with a simple drought index and in the presence of data uncertainties.

Recommendations for future work are presented below in each chapter.

For Chapter 2, long-term field monitoring of groundwater levels in the region could reduce data uncertainties, similar to the daily measurements performed in the river studied. In addition, the understanding of flow components can be improved by a more detailed characterization of the alluvial plain geometry and the variation of hydraulic parameters in the incremental basins of the river reaches.

In Chapters 3 and 4, future work will involve integrating the proposed numerical model and hedging rules into the existing management operation models used in Brazilian semi-arid reservoirs for hydrological drought events. On one hand, this may enhance the estimation of key hydrological processes that influence the water balance of reservoirs in semi-arid regions; on the other hand, it may contribute to evaluating the capability of the hedging model to handle different stakeholder requirements and drought conditions.

In summary, this thesis provides important insights into the complex hydrology of semiarid regions. Based on these findings and the valuable tools developed, water management policies may be enhanced with strategies that are more accurately adjusted to these data-scarce regions.

REFERENCES

ABOUTALEBI MAHYAR; BOZORG HADDAD OMID; LOÁICIGA HUGO A. Optimal monthly reservoir operation rules for hydropower generation derived with SVR-NSGAII. **Journal of Water Resources Planning and Management**, [*s. l.*], vol. 141, n. 11, p. 04015029, 2015.

ADDOR, N.; MELSEN, L. A. Legacy, rather than adequacy, drives the selection of hydrological models. **Water Resources Research**, [*s. l.*], vol. 55, n. 1, p. 378–390, 2019.

ADS. **TerraSAR-X/TanDEM-X**. [*S. l.*], 2023. Disponível em: https://www.intelligence-airbusds.com/en/ 8694-terrasar-x-tandem-x. Acesso em: 24 jan. 2023.

AGÊNCIA NACIONAL DE ÁGUAS E SANEAMENTO BÁSICO (BRASIL). **Curve number da base hidrográfica ottocodificada**. [*S. l.*], 2018. Disponível em: https://metadados.snirh.gov.br/geonetwork/srv/api/records/d1c36d85-a9d5-4f6a-85f7-71c2dc801a67. Acesso em: 4 maio 2024.

AGÊNCIA NACIONAL DE ÁGUAS E SANEAMENTO BÁSICO (BRASIL). **Reservatórios do semiárido brasileiro:** hidrologia, balanço hídrico e operação**.** Brasília: ANA, 2016.

AHANA, Bayongwa Samuel *et al.* Influence of existing reservoirs on the propagation from meteorological to hydrological extremes under climate change in the Ruzizi river basin: historical assessment and future projection. **International Journal of River Basin Management**, [*s. l.*], p. 1–25, 2025.

AHMADIANFAR, Iman; ADIB, Arash; TAGHIAN, Mehrdad. Optimization of multi-reservoir operation with a new hedging rule: application of fuzzy set theory and NSGA-II. **Applied Water Science**, [*s. l.*], vol. 7, n. 6, p. 3075–3086, 2017.

AKHTER, Gulraiz *et al.* Estimation of hydrogeological parameters by using pumping, laboratory data, surface resistivity and thiessen technique in lower Bari Doab (Indus basin), Pakistan. **Applied Sciences**, [*s. l.*], vol. 12, n. 6, p. 3055, 2022.

AKRAM, Muhammad Rizwan. Transboundary flood and drought challenges: a case study of the Sutlej River in Pakistan. **International Journal of River Basin Management**, [*s. l.*], p. 1–20, 2025.

ALLEN, Richard G. *et al.* **Crop evaporation – guidelines for computing crop water requirements. FAO-56 Irrigation and drainage.** Rome: FAO - Food and Agriculture Organization of the United Nations, 1998.

ALVES, Everton John Camelo *et al.* Limits and conditions for the exploitation of alluvial aquifers in the Brazilian semi-arid region. **RBRH**, [*s. l.*], vol. 23, nº 0, 2018. Disponível em: http://www.scielo.br/scielo.php?script=sci_arttext&pid=S2318-03312018000100232&lng=en&tlng=en. Acesso em: 10 jan. 2025.

ALVES, M. *et al.* On the performance of the Canadian land surface scheme driven by the ERA5 reanalysis over the Canadian boreal forest. **Journal of Hydrometeorology**, [*s. l.*], vol. 21, n. 6, p. 1383–1404, 2020.

ANDUALEM, Tesfa Gebrie *et al.* Groundwater recharge estimation using empirical methods from rainfall and streamflow records. **Journal of Hydrology: Regional**

Studies, [*s. l.*], vol. 37, p. 100917, 2021.

ARANTES, Arielle Elias *et al.* Satellite-based water quality assessment of Castanhão reservoir using machine learning and genetic algorithms. **Next Research**, [*s. l.*], vol. 2, n. 2, p. 100340, 2025.

ARAÚJO, J. C.; RIBEIRO, A. L. Avaliação de perda d'água em rios no Semi-Árido. *In*: SIMPÓSIO DE RECURSOS HÍDRICOS DO NORDESTE, 3., 1996, Salvador. **Anais** [...]. Salvador: Associação Brasileira de Recursos Hídricos, 1996. p. 1-16.

ASHRAFI, Seyed Mohammad; DARIANE, Alireza Borhani. Coupled operating rules for optimal operation of multi-reservoir systems. **Water Resources Management**, [*s. l.*], vol. 31, n. 14, p. 4505–4520, 2017.

BATLLE-AGUILAR, Jordi; COOK, Peter G. Transient infiltration from ephemeral streams: a field experiment at the reach scale. **Water Resources Research**, [*s. l.*], vol. 48, n. 11, p. 2012WR012009, 2012.

BEETLE-MOORCROFT, Fern; SHANAFIELD, Margaret; SINGHA, Kamini. Exploring conceptual models of infiltration and groundwater recharge on an intermittent river: the role of geologic controls. **Journal of Hydrology: Regional Studies**, [*s. l.*], vol. 35, p. 100814, 2021.

BESHAVARD, Mahdi *et al.* Establishing effective warning storage to derive optimal reservoir operation policy based on the drought condition. **Agricultural Water Management**, [*s. l.*], vol. 274, p. 107948, 2022.

BOANO, F. *et al.* Hyporheic flow and transport processes: mechanisms, models, and biogeochemical implications: hyporheic flow and transport processes. **Reviews of Geophysics**, [*s. l.*], vol. 52, n. 4, p. 603–679, 2014.

BOULTON, Andrew J. *et al.* Hydrological connectivity in intermittent rivers and ephemeral streams. *In*: DATRY, Thibault; BONADA, Núria; BOULTON, Andrew (orgs.). **Intermittent Rivers and Ephemeral Streams**. [*S. l.*]: Academic Press, 2017. p. 79–108. Disponível em: https://www.sciencedirect.com/science/article/pii/B9780128038352000048. Acesso em: 15 jul. 2026.

BRUNNER, Philip *et al.* Advances in understanding river-groundwater interactions. **Reviews of Geophysics**, [*s. l.*], vol. 55, n. 3, p. 818–854, 2017.

BULL, L. J.; KIRKBY, M. J. Dryland river characteristics and concepts. *In*: BULL, L. J.; KIRKBY, M. J. **Dryland Rivers:** hydrology and geomorphology of semi-arid channels. Chichester: John Wiley & Sons, 2002. p. 3–16.

CAMPOS, José Nilson B. Paradigms and public policies on drought in northeast Brazil: a historical perspective. **Environmental Management**, [*s. l.*], vol. 55, n. 5, p. 1052–1063, 2015.

CARVALHO, Ailton A. De *et al.* Trends of rainfall and temperature in Northeast Brazil. **Revista Brasileira de Engenharia Agrícola e Ambiental**, [*s. l.*], vol. 24, n. 1, p. 15–23, 2020.

CAVALCANTE, A. A. **Aspectos da produção de sedimentos e seus efeitos na gestão dos recursos hídricos no baixo vale do rio Jaguaribe-CE.** 2001. Dissertação (Mestrado em Recursos Hídricos) - Centro de Tecnologia, Universidade Federal do Ceará, Fortaleza, 2001.

CAVALCANTE, Andrea Almeida. Distribuição temporal de descargas e alterações morfológicas em rios semiáridos: o rio Jaguaribe no Ceará, Brasil. **Geography Department University of Sao Paulo**, [*s. l.*], vol. 35, p. 28–36, 2018.

CETINA, M. *et al.* Hydrodynamic conceptual model of groundwater in the headwater of the Rio de Oro, Santander (Colombia) by geochemical and isotope tools. **Water Supply**, [*s. l.*], vol. 20, n. 4, p. 1567–1579, 2020.

CHANG, Jianxia *et al.* Reservoir operations to mitigate drought effects with a hedging policy triggered by the drought prevention limiting water level. **Water Resources Research**, [*s. l.*], vol. 55, n. 2, p. 904–922, 2019.

CHANG, Fi-John; CHEN, Li; CHANG, Li-Chiu. Optimizing the reservoir operating rule curves by genetic algorithms. **Hydrological Processes**, [*s. l.*], vol. 19, n. 11, p. 2277–2289, 2005.

CHEN, Chong *et al.* A comparative study among machine learning and numerical models for simulating groundwater dynamics in the Heihe River Basin, northwestern China. **Scientific Reports**, [*s. l.*], vol. 10, n. 1, p. 3904, 2020.

CHESNAUX, R.; MOLSON, J.W.; CHAPUIS, R.P. An analytical solution for ground water transit time through unconfined aquifers. **Groundwater**, [*s. l.*], vol. 43, n. 4, p. 511–517, 2005.

CHOI, Woonsup. Streams, gaining and losing. *In*: RICHARDSON, Douglas *et al.* (orgs.). **International Encyclopedia of Geography**. 1. ed. [*S. l.*]: Wiley, 2017. p. 1–4. Disponível em: https://onlinelibrary.wiley.com/doi/10.1002/9781118786352.wbieg0062. Acesso em: 11 jan. 2025.

CID, Daniel Antonio Camelo; DE SOUZA FILHO, Francisco De Assis; PORTO, Victor Costa. Collaborative modeling to construct a hedging policy for drought management in reservoir systems. **Journal of Water Resources Planning and Management**, [*s. l.*], vol. 149, n. 1, p. 05022012, 2023.

CIRILO, José Almir *et al.* Development and application of a rainfall-runoff model for semi-arid regions. **RBRH**, [*s. l.*], vol. 25, p. e15, 2020.

COMPANINHA DE GESTÃO DE RECURSOS HÍDRICOS (CEARÁ). **Definidas vazões de liberação dos açudes Castanhão, Orós e Banabuiú para o segundo semestre de 2025**. Fortaleza: COGERH, 2025. Disponível em: https://www.ceara.gov.br/2025/06/17/definidas-vazoes-de-liberacao-dos-acudes-castanhao-oros-e-banabuiu-para-o-segundo-semestre-de-2025/. Acesso em: 6 nov. 2025.

COMPANINHA DE GESTÃO DE RECURSOS HÍDRICOS (CEARÁ). **Outorgas vigentes**. Fortaleza: COGERH, 2023. Disponível em: http://outorgasvigentes.cogerh.com.br/. Acesso em: 24 jan. 2023.

COMPANINHA DE GESTÃO DE RECURSOS HÍDRICOS (CEARÁ). **Relatório de avaliação da segurança hídrica:** aspectos quantitativos. plano de segurança hídrica das bacias hidrográficas estratégicas do Acaraú, Metropolitanas e da Sub-Bacia do Salgado**.** Fortaleza: COGERH, 2017.

CONANT, Brewster *et al.* A framework for conceptualizing groundwater-surface water interactions and identifying potential impacts on water quality, water quantity, and ecosystems. **Journal of Hydrology**, [*s. l.*], vol. 574, p. 609–627, 2019.

COSTA, Alexandre Cunha *et al.* Analysis of channel transmission losses in a dryland river reach in north-eastern Brazil using streamflow series, groundwater level series and multi-temporal satellite data. **Hydrological Processes**, [*s. l.*], vol. 27, n. 7, p. 1046–1060, 2013.

COSTA, Alexandre C. *et al.* Assessment of aquifer recharge and groundwater availability in a semiarid region of Brazil in the context of an interbasin water transfer scheme. **Hydrogeology Journal**, [*s. l.*], vol. 31, n. 3, p. 751–769, 2023.

COSTA, Alexandre *et al.* Expedição científica ao alto curso do Rio Jaguaribe, estado do Ceará: identificação da exata nascente do possivelmente maior rio efêmero do mundo. **Caderno de Geografia**, [*s. l.*], vol. 30, n. 63, p. 956, 2020.

COSTA, Alexandre C. *et al.* **Integrated surface-groundwater modelling for assessment of aquifer recharge and groundwater availability in a semi-arid region in the context of inter-basin water transfer**. [S. l.]: [s. n.], 2022. Disponível em: https://www.researchsquare.com/article/rs-1269113/v1. Acesso em: 11 jan. 2025.

COSTA, A. C.; BRONSTERT, A.; DE ARAÚJO, J. C. A channel transmission losses model for different dryland rivers. **Hydrology and Earth System Sciences**, [*s. l.*], vol. 16, n. 4, p. 1111–1135, 2012.

COULIBALY, Wawogninlin Brice *et al.* Influence of climate extremes on discharge inflow and reservoir management at the Kossou dam. **International Journal of River Basin Management**, [*s. l.*], p. 1–21, 2025.

COMPAINHA DE PESQUISA DE RECURSOS MINERAIS (BRASIL). **Mapa geológico:** Jaguaretama Folha SB.24-X-C-IV**.** Fortaleza: CPRM, 2014.

COMPAINHA DE PESQUISA DE RECURSOS MINERAIS (BRASIL). **Mapa hidrogeológico:** Jaguaribe - Folha SB.24**.** Fortaleza: CPRM, 2015.

CUNHA, V. C. V. **Avaliação da interação entre águas subterrâneas e superficiais na bacia do rio das Fêmeas, sistema aquífero Urucuia-Bahia.** [*S. l.*]: Centro de Desenvolvimento da Tecnologia Nuclear, 2017.

DA S. ALVES, R. *et al.* Effects of the latest drought on the alluvial aquifer of a semiarid region in northeastern Brazil. *In:* INTERNATIONAL ASSOCIATION OF HYDROLOGICAL SCIENCES, 11., 2022, Montpellier. **Proceedings** […]. Montpellier: IAHS, 2024. p. 225–229.

DARAMOLA, Mojolaoluwa Toluwalase; XU, Ming. Recent changes in global dryland temperature and precipitation. **International Journal of Climatology**, [*s. l.*], vol. 42, n. 2, p. 1267–1282, 2022.

DE ARAÚJO, José Carlos; BRONSTERT, Axel. A method to assess hydrological drought in semi-arid environments and its application to the Jaguaribe river basin, Brazil. **Water International**, [*s. l.*], vol. 41, n. 2, p. 213–230, 2016.

DE ARAÚJO JÚNIOR, Luiz Martins *et al.* Avaliação de indices de seca meteorológica e hidrológica em relação ao impacto de acumulação de água em reservatório: um estudo de caso para o reservatório de Jucazinho-PE. **Revista AIDIS de Ingeniería y Ciencias Ambientales. Investigación, desarrollo y práctica**, [*s. l.*], vol. 13, n. 2, p. 382, 2020.

DE ARAÚJO, J C; MEDEIROS, P H A. Impact of dense reservoir networks on water resources in semiarid environments. **Australasian Journal of Water Resources**, [*s. l.*], vol. 17, n. 1, p. 87–100, 2013.

DE MEDEIROS, Edson Ramos; CARVALHO, Terciane Sabadini; DE SOUZA, Kênia Barreiro. São Francisco river transposition project: socio-economic impacts in Brazilian Northeast semi-arid region. **Papers in Regional Science**, [*s. l.*], vol. 101, n. 6, p. 1441–1469, 2022.

DE SOUSA, Marionei Fomaca *et al.* Streamflow prediction based on machine learning models and rainfall estimated by remote sensing in the Brazilian savanna and Amazon biomes transition. **Modeling Earth Systems and Environment**, [*s. l.*], vol. 10, p. 1191–1202, 2024.

DEB, K. *et al.* A fast and elitist multiobjective genetic algorithm: NSGA-II. **IEEE Transactions on Evolutionary Computation**, [*s. l.*], vol. 6, n. 2, p. 182–197, 2002.

DESHPANDE, Gauri; DHORDE, Anargha Amit. Validating the curve number estimation approaches: a case study of an urbanizing watershed from Western Maharashtra, India. **Modeling Earth Systems and Environment**, [*s. l.*], vol. 10, p. 1615–1629, 2024.

DEVIA, Gayathri K.; GANASRI, B.P.; DWARAKISH, G.S. A review on hydrological models. **Aquatic Procedia**, [*s. l.*], vol. 4, p. 1001–1007, 2015.

DI CIACCA, Antoine *et al.* Deriving transmission losses in ephemeral rivers using satellite imagery and machine learning. **Hydrology and Earth System Sciences**, [*s. l.*], vol. 27, n. 3, p. 703–722, 2023.

EL-NASR, Ahmed Abu *et al.* Modelling the hydrology of a catchment using a distributed and a semi-distributed model. **Hydrological Processes**, [*s. l.*], vol. 19, n. 3, p. 573–587, 2005.

FAYE, Cheikh. Comparative analysis of meteorological drought based on the SPI and SPEI indices. **HighTech and Innovation Journal**, [*s. l.*], vol. 3, p. 15–27, 2022.

FREAD, D. L. Flow Routing. *In*: MAIDMENT, D. R. (org.). **Handbook of hydrology**. New York: D. R. Maidment, 1993. p. 316-345.

FUNDAÇÃO CEARENSE DE METEOROLOGIA E RECURSOS HÍDRICOS (BRASIL). **Ceará hydrological portal**. Fortaleza: FUNCEME, 2026. Disponível em: http://www.hidro.ce.gov.br. Acesso em: 22 jan. 2026.

GAMA, Allyne F. *et al.* Occurrence, distribution, and fate of pesticides in an intensive farming region in the Brazilian semi-arid tropics (Jaguaribe River, Ceará). **Journal of Soils and Sediments**, [*s. l.*], vol. 17, n. 4, p. 1160–1169, 2017.

GIBBS, Matthew S. *et al.* State updating and calibration period selection to improve dynamic monthly streamflow forecasts for an environmental flow management application. **Hydrology and Earth System Sciences**, [*s. l.*], vol. 22, n. 1, p. 871–887, 2018.

GNANACHANDRASAMY, G. *et al.* Evaluation of vulnerability zone of a coastal aquifer through GALDIT GIS index techniques. *In*: VENKATRAMANAN, S.; PRASANNA, M. V.; CHUNG, S. Y. (org.). **GIS and geostatistical techniques for groundwater science**. Amsterdam: Elsevier, 2019. p. 209–221. Disponível em: https://linkinghub.elsevier.com/retrieve/pii/B9780128154137000158. Acesso em: 11 jan. 2025.

GOMES, Maurício De Gois; MAIA, Adelena Gonçalves; MEDEIROS, Joana D'arc Freire De. Reservoir operation rule in semiarid areas: the quantity-quality approach.

Journal of Hydrology, [*s. l.*], vol. 610, p. 127944, 2022.

GOMEZ, Maria Laura *et al.* Review: hydrogeology of Northern Mendoza (Argentina), from the Andes to the eastern plains, in the context of climate change. **Hydrogeology Journal**, [*s. l.*], vol. 30, n. 3, p. 725–750, 2022.

GONÇALVES, Suellen Teixeira Nobre *et al.* Avaliação de índices de seca no monitoramento hidrológico de reservatórios estratégicos do Ceará, Brasil. **Revista Brasileira de Meteorologia**, [*s. l.*], vol. 38, p. e38230018, 2023a.

GONÇALVES, Suellen Teixeira Nobre *et al.* Comparative analysis of drought indices in hydrological monitoring in Ceará's semi-arid basins, Brazil. **Water**, [*s. l.*], vol. 15, n. 7, p. 1259, 2023b.

GOODRICH, D.C. *et al.* Southwestern intermittent and ephemeral stream connectivity. **JAWRA Journal of the American Water Resources Association**, [*s. l.*], vol. 54, n. 2, p. 400–422, 2018.

GOSLING, Simon N.; ARNELL, Nigel W. Simulating current global river runoff with a global hydrological model: model revisions, validation, and sensitivity analysis. **Hydrological Processes**, [*s. l.*], vol. 25, n. 7, p. 1129–1145, 2011.

GRABOWSKI, Robert C. *et al.* The land–river interface: a conceptual framework of environmental process interactions to support sustainable development. **Sustainability Science**, [*s. l.*], vol. 17, n. 4, p. 1677–1693, 2022.

GUI, Ziling *et al.* Improving runoff prediction using remotely sensed actual evapotranspiration during rainless periods. **Journal of Hydrologic Engineering**, [*s. l.*], vol. 24, n. 12, p. 04019050, 2019.

GUO, Yuhan *et al.* Regionalization of hydrological modeling for predicting streamflow in ungauged catchments: a comprehensive review. **WIREs Water**, [*s. l.*], vol. 8, n. 1, p. e1487, 2021.

GUTH, Peter L. *et al.* Digital elevation models: terminology and definitions. **Remote Sensing**, [*s. l.*], vol. 13, n. 18, p. 3581, 2021.

GUTH, Peter L.; GEOFFROY, Tera M. LiDAR point cloud and ICESat-2 evaluation of 1 second global digital elevation models: Copernicus wins. **Transactions in GIS**, [*s. l.*], vol. 25, n. 5, p. 2245–2261, 2021.

HAZBAVI, Zeinab *et al.* Changeability of reliability, resilience and vulnerability indicators with respect to drought patterns. **Ecological Indicators**, [*s. l.*], vol. 87, p. 196–208, 2018.

HONG, Xu *et al.* Investigation of drought risk using a dynamic optimization framework in regional water allocation procedure with different streamflow scenarios. **Frontiers in Environmental Science**, [*s. l.*], vol. 10, p. 813239, 2022.

HORTON, Pascal; SCHAEFLI, Bettina; KAUZLARIC, Martina. Why do we have so many different hydrological models? A review based on the case of Switzerland. **WIREs Water**, [*s. l.*], vol. 9, n. 1, p. e1574, 2022.

HSU, Nien-Sheng; CHENG, Ker-Wei. Network flow optimization model for basin-scale water supply planning. **Journal of Water Resources Planning and Management**, [*s. l.*], vol. 128, n. 2, p. 102–112, 2002.

HUGHES, D.A. A simple approach to estimating channel transmission losses in large South African river basins. **Journal of Hydrology: Regional Studies**, [*s. l.*], vol. 25,

p. 100619, 2019.

HUSSAIN, Fiaz; WU, Ray-Shyan; SHIH, Dong-Sin. Water table response to rainfall and groundwater simulation using physics-based numerical model: WASH123D. **Journal of Hydrology: Regional Studies**, [*s. l.*], vol. 39, p. 100988, 2022.

IZADY, A. *et al.* A framework toward developing a groundwater conceptual model. **Arabian Journal of Geosciences**, [*s. l.*], vol. 7, n. 9, p. 3611–3631, 2014.

KARAMOUZ, Mohammad; ARAGHINEJAD, Shahab. Drought mitigation through long-term operation of reservoirs: case study. **Journal of Irrigation and Drainage Engineering**, [*s. l.*], vol. 134, n. 4, p. 471–478, 2008.

KARLOVIĆ, Igor *et al.* Development of a hydrogeological conceptual model of the Varaždin alluvial aquifer. **Hydrology**, [*s. l.*], vol. 8, n. 1, p. 19, 2021.

KARNATAPU, Leela Krishna; ANNAVARAPU, Srinivasa Prasad; NANDURI, Umamahesh V. Multi-objective reservoir operating strategies by genetic algorithm and nonlinear programming (GA–NLP) hybrid approach. **Journal of The Institution of Engineers (India): Series A**, [*s. l.*], vol. 101, p. 105–115, 2020.

KIM, Shaun S. H. *et al.* Modelling daily transmission losses in basin-scale river system models under changing hydrological regimes. **Hydrological Processes**, [*s. l.*], vol. 36, n. 6, p. e14625, 2022.

KNIGHTON, A. David; NANSON, Gerald C. Flow transmission along an arid zone anastomosing river, cooper creek, australia. **Hydrological Processes**, [*s. l.*], vol. 8, n. 2, p. 137–154, 1994.

KREIS, Marjorie *et al.* Isotopic characterisation and dating of groundwater recharge mechanisms in crystalline fractured aquifers: example of the semi-arid Banabuiú watershed (Brazil). **Isotopes in Environmental and Health Studies**, [*s. l.*], vol. 56, n. 5–6, p. 418–430, 2020.

KUMAR, Amit *et al.* Assessment of machine learning models to predict daily streamflow in a semiarid river catchment. **Neural Computing and Applications**, [*s. l.*], 2024. Disponível em: https://link.springer.com/10.1007/s00521-024-09748-1. Acesso em: 15 jun. 2024.

LACHASSAGNE, Patrick; DEWANDEL, Benoît; WYNS, Robert. Review: hydrogeology of weathered crystalline/hard-rock aquifers—guidelines for the operational survey and management of their groundwater resources. **Hydrogeology Journal**, [*s. l.*], vol. 29, n. 8, p. 2561–2594, 2021.

LAMONTAGNE, Jonathan R.; BARBER, Caitline A.; VOGEL, Richard M. Improved estimators of model performance efficiency for skewed hydrologic data. **Water Resources Research**, [*s. l.*], vol. 56, n. 9, p. e2020WR027101, 2020.

LANGE, Jens. Dynamics of transmission losses in a large arid stream channel. **Journal of Hydrology**, [*s. l.*], vol. 306, n. 1–4, p. 112–126, 2005.

LIMA NETO, Iran Eduardo. Phosphorus dynamics in water and sediments in a large multi-use reservoir under extreme volume variation. **Ecological Modelling**, [*s. l.*], vol. 510, p. 111316, 2025.

LIU, Qi *et al.* Simulation of regional groundwater levels in arid regions using interpretable machine learning models. **Science of The Total Environment**, [*s. l.*], vol. 831, p. 154902, 2022.

LOPES, Alan Vaz; FREITAS, Marcos Airton de Sousa. A alocação de água como instrumento de gestão de recursos hídricos: experiências brasileiras. **REGA**, [*s. l.*], vol. 4, n. 1, p. 5–28, 2007.

LU, Chengpeng *et al.* estimation of the interaction between groundwater and surface water based on flow routing using an improved nonlinear Muskingum-Cunge method. **Water Resources Management**, [*s. l.*], vol. 35, n. 8, p. 2649–2666, 2021.

LUO, Chengxin *et al.* Characteristics of reservoirs to mitigate drought effects with a hedging rule triggered by drought limited water level. **Journal of Hydrology**, [*s. l.*], vol. 617, p. 129106, 2023.

MAIA, R.; BEZERRA, F. **Structural geomorphology in Northeastern Brazil.** Cham: Springer Cham, 2020.

MAMUDU, Lawal *et al.* Evaluating the predictive accuracy of some regression models and artificial neural networks in streamflow forecasting (a case study of the Kaduna river, northwest Nigeria). **Modeling Earth Systems and Environment**, [*s. l.*], vol. 11, p. 125, 2025.

MCKEE, T. B.; DOESKEN, N. J.; KLEIST, J. The relationship of drought frequency and duration to time scales. *In*: CONFERENCE ON APPLIED CLIMATOLOGY, 8., 1993, Anaheim. **Proceedings** […]. Boston: American Meteorological Society, 1993. p. 179–184.

MCMAHON, Thomas A.; ADELOYE, Adebayo J.; ZHOU, Sen-Lin. Understanding performance measures of reservoirs. **Journal of Hydrology**, [*s. l.*], vol. 324, n. 1–4, p. 359–382, 2006.

MCMAHON, Thomas A.; NATHAN, Rory J. Baseflow and transmission loss: a review. **WIREs Water**, [*s. l.*], vol. 8, n. 4, p. e1527, 2021.

MENGISTU, Haile A. *et al.* Conceptual hydrogeological and numerical groundwater flow modelling around the Moab Khutsong deep gold mine, South Africa. **Groundwater for Sustainable Development**, [*s. l.*], vol. 9, p. 100266, 2019.

MISHRA, A.K.; DESAI, V.R. Spatial and temporal drought analysis in the Kansabati river basin, India. **International Journal of River Basin Management**, [*s. l.*], vol. 3, n. 1, p. 31–41, 2005.

MISHRA, Surendra Kumar; SINGH, Vijay P. **Soil Conservation Service Curve Number (SCS-CN) Methodology**. Dordrecht: Springer Netherlands, 2003. Disponível em: http://link.springer.com/10.1007/978-94-017-0147-1. Acesso em: 30 abr. 2024.

MOLISANI, Mauricio Mussi *et al.* Trophic state, phytoplankton assemblages and limnological diagnosis of the Castanhão reservoir, CE, Brazil. **Acta Limnologica Brasiliensia**, [*s. l.*], vol. 22, n. 1, p. 1–12, 2010.

MORIASI, D. N.; GITAU, M. W.; DAGGUPATI, P. Hydrologic and water quality models: performance measures and evaluation criteria. **Transactions of the ASABE**, [*s. l.*], vol. 58, n. 6, p. 1763–1785, 2015.

MORIN, Efrat *et al.* Flood routing and alluvial aquifer recharge along the ephemeral arid Kuiseb river, Namibia. **Journal of Hydrology**, [*s. l.*], vol. 368, n. 1–4, p. 262–275, 2009.

MUJERE, Never *et al.* Dynamics and scales of transmission losses in dryland river systems: a meta-analysis. **Australasian Journal of Water Resources**, [*s. l.*], vol. 26,

n. 2, p. 227–241, 2022.

MUSY, A.; HIGY, C. **Hydrology:** a science of nature. New Hampshire: Science Publishers Enfield, 2011.

NEELAKANTAN, T R; SASIREKA, K. Review of hedging rules applied to reservoir operation. **International Journal of Engineering and Technology**, [*s. l.*], vol. 7, n. 5, 2015. p. 1571-1580.

NTONA, Maria Margarita *et al.* Modeling groundwater and surface water interaction: an overview of current status and future challenges. **Science of The Total Environment**, [*s. l.*], vol. 846, p. 157355, 2022.

PACHECO-GUERRERO, A. *et al.* Flooding in ephemeral streams: incorporating transmission losses. **Journal of Maps**, [*s. l.*], vol. 13, n. 2, p. 350–357, 2017.

PALHETA, E.S.M.; HOLANDA, J.L.R.; GOMES, I.P. **Carta geológica-geofísica. folha SB.24Z-A-I Orós.** Fortaleza: CPRM, 2019.

PEREIRA, F. J. S. **Estimativa da concentração de sedimentos suspensos no rio Jaguaribe-CE através de imagens do satélite RapidEye.** 2017. Dissertação (Mestrado em Engenharia Agrícola) - Centro de Ciências Agrárias, Universidade Federal do Ceará, Fortaleza, 2017.

PETERSON, D. M. **Variably saturated flow between streams and aquifers**. Socorro: New Mexico Water Resources Research Institute, 1988. p. 1–259.

PINHEIRO, Antônio Flávio Costa *et al.* Captação da água subterrânea no aquífero aluvionar do Rio Jaguaribe, Ceará: evolução e problemática. **Revista Brasileira de Geografia Física**, [*s. l.*], vol. 16, n. 5, p. 2908–2927, 2023.

QUICHIMBO, E. A. *et al.* Assessing the sensitivity of modelled water partitioning to global precipitation datasets in a data-scarce dryland region. **Hydrological Processes**, [*s. l.*], vol. 37, n. 12, p. e15047, 2023.

RABELO, Udinart P. *et al.* Representing a dense network of ponds and reservoirs in a semi-distributed dryland catchment model. **Journal of Hydrology**, [*s. l.*], vol. 603, p. 127103, 2021.

RAJASEKHAR, Madiga *et al.* Identification of groundwater recharge-based potential rainwater harvesting sites for sustainable development of a semiarid region of southern India using geospatial, AHP, and SCS-CN approach. **Arabian Journal of Geosciences**, [*s. l.*], vol. 13, n. 1, p. 24, 2020.

RAMAKRISHNAN, D.; DURGA RAO, K. H. V.; TIWARI, K. C. Delineation of potential sites for water harvesting structures through remote sensing and GIS techniques: a case study of Kali watershed, Gujarat, India. **Geocarto International**, [*s. l.*], vol. 23, n. 2, p. 95–108, 2008.

RAULINO, J. B.S.; SILVEIRA, C. S.; LIMA NETO, I. E.. Eutrophication risk assessment of a large reservoir in the Brazilian semiarid region under climate change scenarios. **Anais da Academia Brasileira de Ciências**, [*s. l.*], vol. 94, n. 4, p. e20201689, 2022.

RAULINO, João B. S.; SILVEIRA, Cleiton S.; LIMA NETO, Iran Eduardo. Assessment of climate change impacts on hydrology and water quality of large semi-arid reservoirs in Brazil. **Hydrological Sciences Journal**, [*s. l.*], vol. 66, n. 8, p. 1321–1336, 2021.

RÊGO, T. C. C. C. **Avaliação da perda d'água em trânsito na bacia do rio Jaguaribe.** 2021. Dissertação (Mestrado em Recursos Hídricos) - Centro de Tecnologia, Universidade Federal do Ceará, Fortaleza, 2021.

ROCHA, Maria Aparecida Melo *et al.* Total phosphorus modeling and carrying capacity of the largest reservoir in the Brazilian semiarid region. **Water, Air, & Soil Pollution**, [*s. l.*], vol. 236, n. 8, p. 525, 2025.

ROCHA, Maria Aparecida Melo *et al.* Understanding the water quality dynamics in a large tropical reservoir under hydrological drought conditions. **Water, Air, & Soil Pollution**, [*s. l.*], vol. 235, n. 1, p. 76, 2024.

ROTTLER, Erwin *et al.* Regional-scale seasonal forecast of surface water availability in a semi-arid environment: the case of Ceará state in northeast of Brazil. **Journal of Hydrology: Regional Studies**, [*s. l.*], vol. 56, p. 102058, 2024.

RUBEN, Lucas Dominguez. Large meandering bends with high width-to-depth ratios: Insights from hydro-sedimentological processes. **Geomorphology**, [*s. l.*], vol. 374, p. 107521, 2021.

SAEDI, Javad *et al.* Assessing the impact of climate change and human activity on streamflow in a semiarid basin using precipitation and baseflow analysis. **Scientific Reports**, [*s. l.*], vol. 12, n. 1, p. 9228, 2022.

SAHU, Mukul Kumar; SHWETHA, H. R.; DWARAKISH, G. S. State-of-the-art hydrological models and application of the HEC-HMS model: a review. **Modeling Earth Systems and Environment**, [*s. l.*], vol. 9, p. 3029–3051, 2023.

SANDOVAL, Eric *et al.* Groundwater recharge assessment in a rural, arid, mid-mountain basin in North-Central Chile. **Hydrological Sciences Journal**, [*s. l.*], vol. 63, n. 13–14, p. 1873–1889, 2018.

SANDOVAL-SOLIS, Samuel *et al.* Collaborative modeling to evaluate water management scenarios in the Rio Grande basin. **JAWRA Journal of the American Water Resources Association**, [*s. l.*], vol. 49, n. 3, p. 639–653, 2013.

SANTOS, Kelly Marina Silva. **Avaliação da eficiência do monitor de secas para definição de secas em Sergipe**. 2020. Dissertação (Mestrado em Engenharia Civil) - Centro de Ciências Exatas e Tecnologia, Universidade Federal de Sergipe, São Cristóvão, 2020.

SATOH, Yusuke *et al.* The timing of unprecedented hydrological drought under climate change. **Nature Communications**, [*s. l.*], vol. 13, n. 1, p. 3287, 2022.

SCHOENER, Gerhard. Quantifying transmission losses in a New Mexico ephemeral stream: a losing proposition. **Journal of Hydrologic Engineering**, [*s. l.*], vol. 22, n. 3, p. 05016038, 2017.

SCHREINER-MCGRAW, Adam; AJAMI, Hoori; VIVONI, Enrique R. Extreme weather events and transmission losses in arid streams. **Environmental Research Letters**, [*s. l.*], 2019. Disponível em: http://iopscience.iop.org/article/10.1088/1748-9326/ab2949. Acesso em: 11 jan. 2025.

ŞEN, Zekâi. Reservoirs for water supply under climate change impact: a review. **Water Resources Management**, [*s. l.*], vol. 35, n. 11, p. 3827–3843, 2021.

SHIH, Jhih-Shyang; REVELLE, Charles. Water supply operations during drought: a discrete hedging rule. **European Journal of Operational Research**, [*s. l.*], vol. 82, n.

1, p. 163–175, 1995.

SOOD, Aditya; SMAKHTIN, Vladimir. Global hydrological models: a review. **Hydrological Sciences Journal**, [*s. l.*], vol. 60, n. 4, p. 549–565, 2015.

SOPHOCLEOUS, Marios. Interactions between groundwater and surface water: the state of the science. **Hydrogeology Journal**, [*s. l.*], vol. 10, n. 1, p. 52–67, 2002.

STRINGER, Lindsay C. *et al.* Climate change impacts on water security in global drylands. **One Earth**, [*s. l.*], vol. 4, n. 6, p. 851–864, 2021.

SWAIN, Sushree Swagatika *et al.* Water scarcity-risk assessment in data-scarce river basins under decadal climate change using a hydrological modelling approach. **Journal of Hydrology**, [*s. l.*], vol. 590, p. 125260, 2020.

THOMS, M.C; SHELDON, F. Water resource development and hydrological change in a large dryland river: the Barwon–Darling river, Australia. **Journal of Hydrology**, [*s. l.*], vol. 228, n. 1–2, p. 10–21, 2000.

THORNTHWAITE, C. W.; MATHER, J. R. **The water balance.** Centerton: Laboratory of Climatology, 1995.

TOLEDO, Cristian Epifanio *et al.* Water loss in transit in an intermittent river in Brazilian semi-arid. **Revista Agro@mbiente On-line**, [*s. l.*], vol. 12, n. 3, p. 177, 2018.

TOMASELLA, Javier *et al.* Assessment of trends, variability and impacts of droughts across Brazil over the period 1980–2019. **Natural Hazards**, [*s. l.*], vol. 116, n. 2, p. 2173–2190, 2023.

TONÉ, Arthur Jordan de Azevedo *et al.* Spatiotemporal river–aquifer interactions of a large tropical dryland river with high anthropic intervention. **Hydrological Sciences Journal**, [*s. l.*], vol. 68, n. 14, p. 2009–2026, 2023.

TONÉ, Arthur Jordan de Azevedo *et al.* Streamflow prediction based on data-scarce river-aquifer dynamics estimated by a simplified modelling framework in a dryland catchment. **Modeling Earth Systems and Environment**, [*s. l.*], vol. 11, n. 4, p. 282, 2025.

TU MING-YEN *et al.* Optimization of hedging rules for reservoir operations. **Journal of Water Resources Planning and Management**, [*s. l.*], vol. 134, n. 1, p. 3–13, 2008.

UFC; COGERH. **Estudos de regionalização de parâmetros de modelo hidrológico chuva-vazão, para as bacias totais e incrementais dos reservatórios monitorados pela Companhia de Gestão dos Recursos Hídricos. Relatório 1.1.12.** Fortaleza: UFC, 2013.

WANG, Jin *et al.* A construction method of visual conceptual scenario for hydrological conceptual modeling. **Environmental Modelling & Software**, [*s. l.*], vol. 145, p. 105190, 2021.

WANG, Ping; POZDNIAKOV, Sergey P.; VASILEVSKIY, Peter Yu. Estimating groundwater-ephemeral stream exchange in hyper-arid environments: field experiments and numerical simulations. **Journal of Hydrology**, [*s. l.*], vol. 555, p. 68–79, 2017.

WATSON, Andrew *et al.* Quantifying and understanding the source of recharge for alluvial systems in arid environments through the development of a seepage model. **Journal of Hydrology**, [*s. l.*], vol. 601, p. 126650, 2021.

WEREDE, Kindie Zewdie *et al.* Assessing the impacts of climate change on streamflow in the upper Omo Gibe basin of southwest Ethiopia using MIKE NAM. **International Journal of River Basin Management**, [*s. l.*], p. 1–17, 2024.

WIEGAND, Mário Cesar. **Proposta metodológica para estimativa da produção de sedimentos em grandes bacias hidrográficas:** estudo de caso Alto Jaguaribe, CE. 2009. Dissertação (Mestrado em Engenharia Agrícola) - Centro de Ciências Agrárias, Universidade Federal do Ceará, Fortaleza, 2009.

WOESSNER, W. W. Stream and fluvial plain groundwater interactions: rescaling hydrogeologic thought. **Ground Water**, [*s. l.*], vol. 38, n. 3, p. 423–429, 2000.

WOLSTENHOLME, Joshua M. *et al.* A new approach for measuring surface hydrological connectivity. **Hydrological Processes**, [*s. l.*], vol. 34, n. 3, p. 538–552, 2020.

XIMENES NETO, Antonio Rodrigues *et al.* Transgressive deposits and morphological patterns in the equatorial Atlantic shallow shelf (Northeast Brazil). **Regional Studies in Marine Science**, [*s. l.*], vol. 24, p. 212–224, 2018.

XU, Tianfang; LIANG, Feng. Machine learning for hydrologic sciences: an introductory overview. **WIREs Water**, [*s. l.*], vol. 2, p. 1533, 2021.

YANG, Shuyu *et al.* A physical process and machine learning combined hydrological model for daily streamflow simulations of large watersheds with limited observation data. **Journal of Hydrology**, [*s. l.*], vol. 590, p. 125206, 2020.

ZANIOLO, Marta *et al.* Automatic design of basin-specific drought indexes for highly regulated water systems. **Hydrology and Earth System Sciences**, [*s. l.*], vol. 22, n. 4, p. 2409–2424, 2018.

ZARGAR, Amin *et al.* A review of drought indices. **Environmental Reviews**, [*s. l.*], vol. 19, nº NA, p. 333–349, 2011.

ZHANG, Zhenyu *et al.* A method for detecting the non-stationarity during high flows under global change. **Science of The Total Environment**, [*s. l.*], vol. 851, n. 2, p. 158341, 2022.

ZHOU, Pengpeng *et al.* Numerical modeling for the temporal variations of the water interchange between groundwater and surface water in a regional great lake (Poyang lake, China). **Journal of Hydrology**, [*s. l.*], vol. 610, p. 127827, 2022.

ZHOU, Zibo; CARTWRIGHT, Ian. Using geochemistry to identify and quantify the sources, distribution, and fluxes of baseflow to an intermittent river impacted by climate change: the upper Wimmera river, southeast Australia. **Science of The Total Environment**, [*s. l.*], vol. 801, p. 149725, 2021.

APPENDIX A – SUPPLEMENTARY MATERIAL FOR CHAPTER 2

Figure S2.1 - River discharge measurement using RiverSurveyor M9 ADCP in the stream gauge.

Source: Toné *et al.* (2023).

Figure S2.2 - Curve Number in the study site, with its hydrologic and geologic description and stream gauges identification.

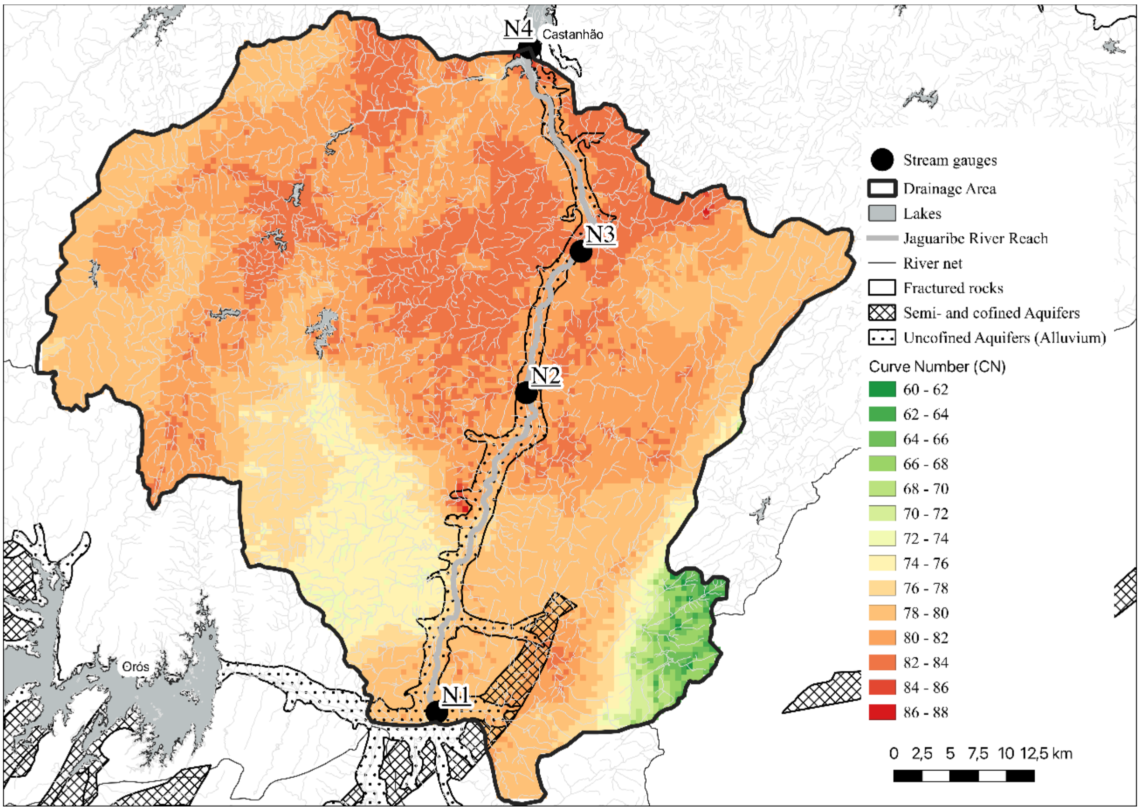

Source: prepared by the author.

Figure S2.3 - Rating curves of stream gauges (N1, N2, N3 and N4).

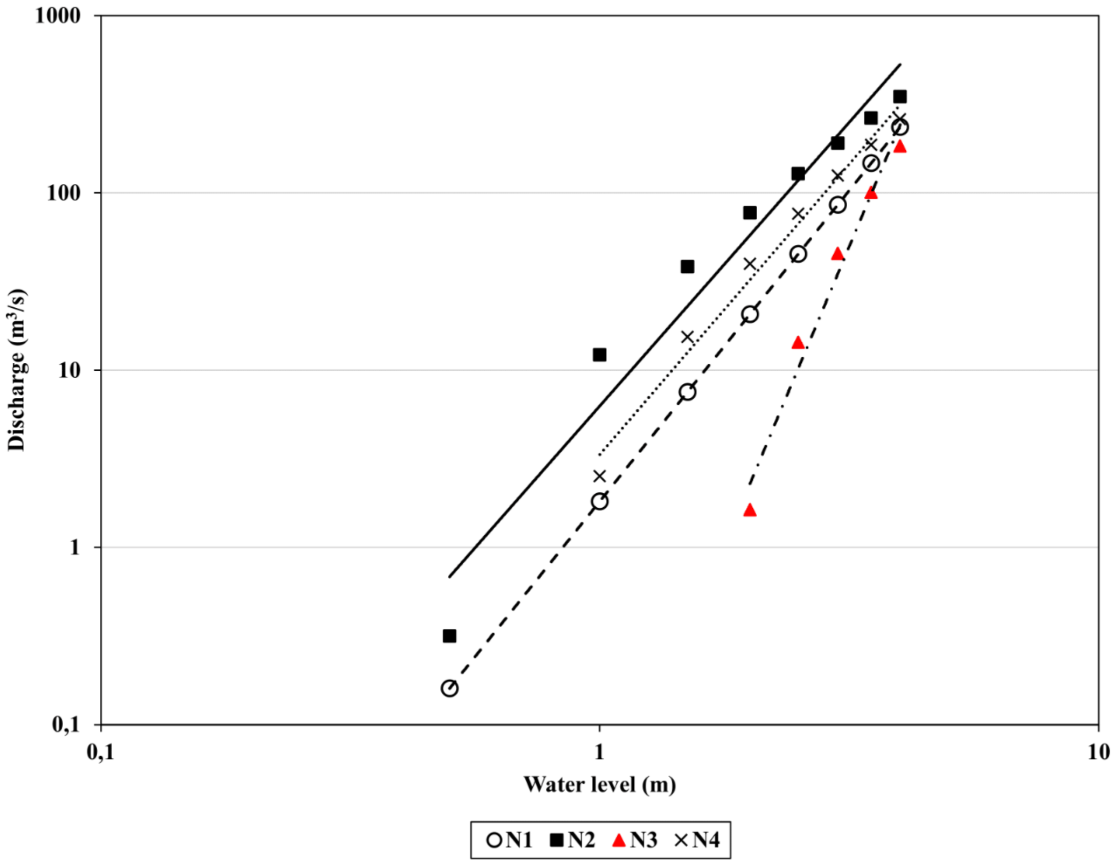

Source: prepared by the author.

APPENDIX B – SUPPLEMENTARY MATERIAL FOR CHAPTER 3

The conceptual model for the study site reach was developed in Chapter 1 (Toné *et al.*, 2023). This model represents the area where interactions between the Jaguaribe River and alluvium occur, considering a single-layer isotropic aquifer. It encompasses processes such as surface runoff from the incremental basin, rainfall and evaporation related to the river, groundwater exploitation, gains and losses of the river concerning groundwater, and event-based routing. In summary, at the beginning of the rainy season, when the water table is below the riverbed, vertical infiltration occurs from the riverbed into the alluvium and vadose zones. This contributes downstream as hyporheic flow (Figure S3.1a). Conversely, baseflow, resulting from the elevation of the water table due to aquifer recharge, hyporheic flow, and direct precipitation on the river reach, may overlap with transmission losses, ultimately contributing to river discharge (Figure S3.1b).

Figure S3.1 - Conceptual model of river-aquifer interaction at the study site.

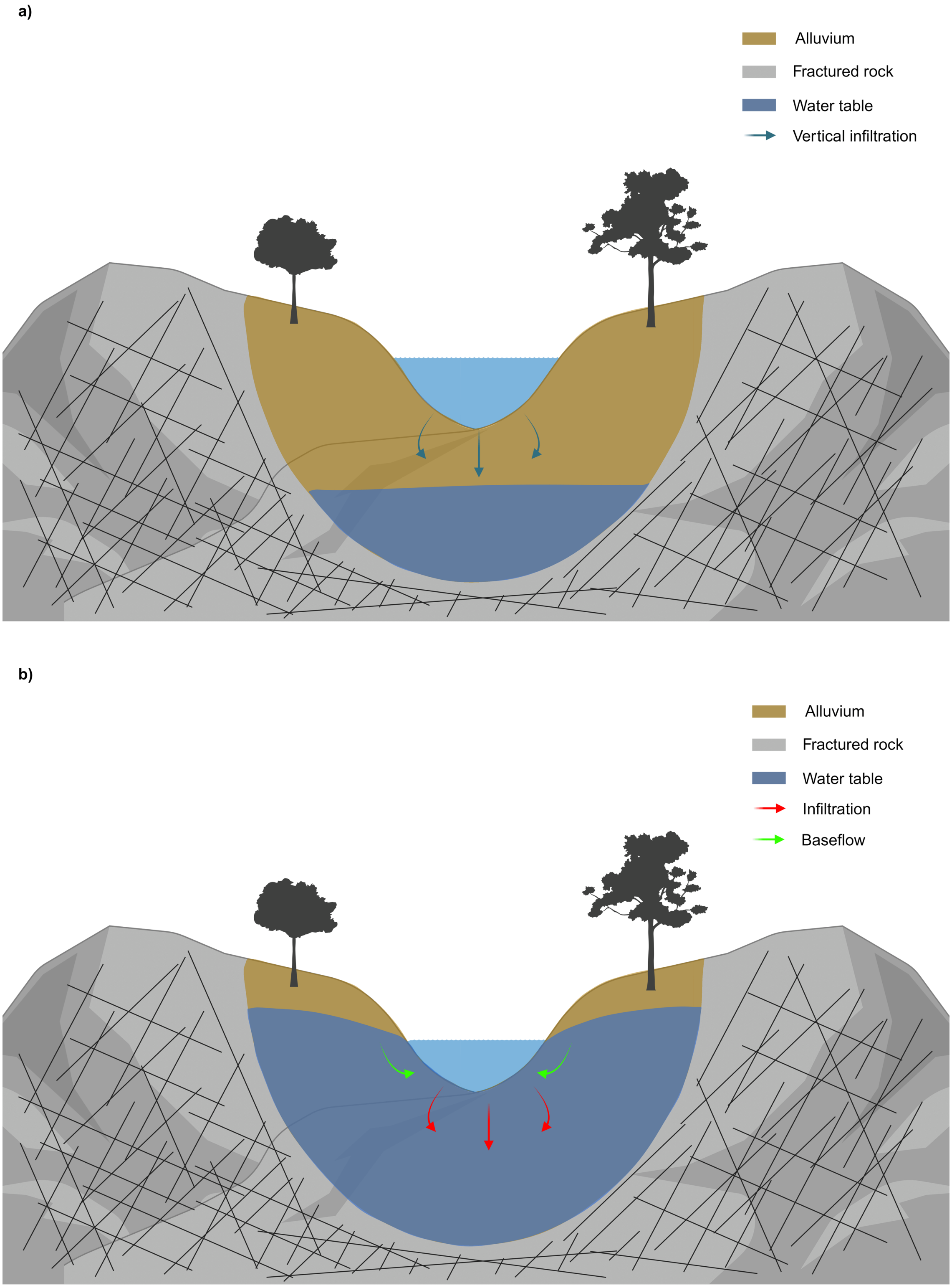

Source: prepared by the author.

Figure S3.2 - Schematic of the study site for elaborate the river-aquifer numerical model.

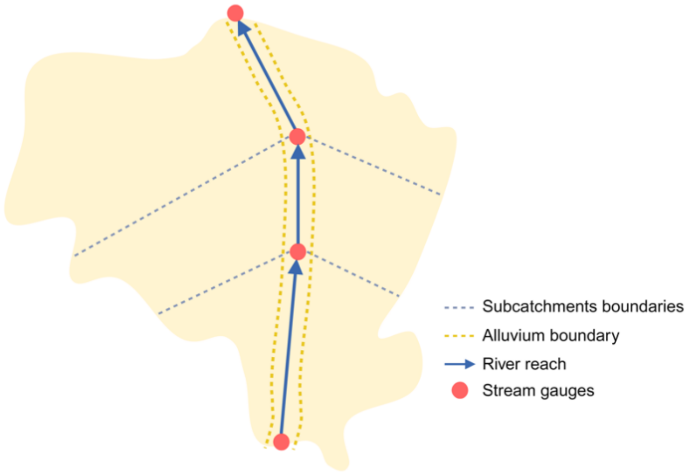

Source: prepared by the author.

Figure S3.3 - A schematic representation of the numerical streamflow model, with the steps where commonly overlooked stream-aquifer processes are estimated, highlighted in yellow.

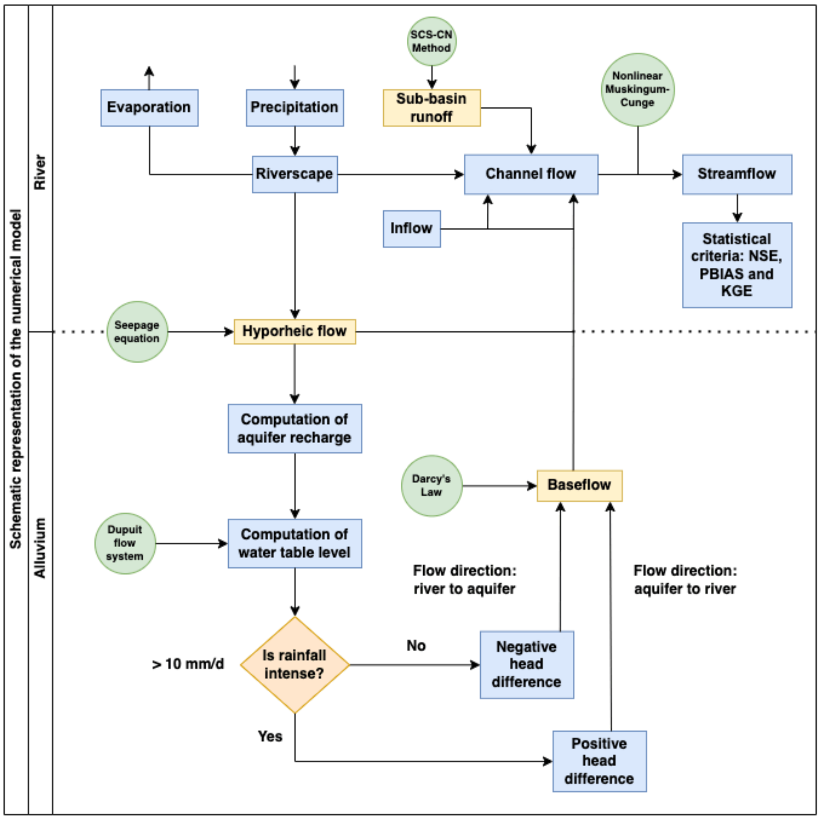

Source: prepared by the author.

Figure S3.4 - Schematic representation of the aquifer for the analytical solution.

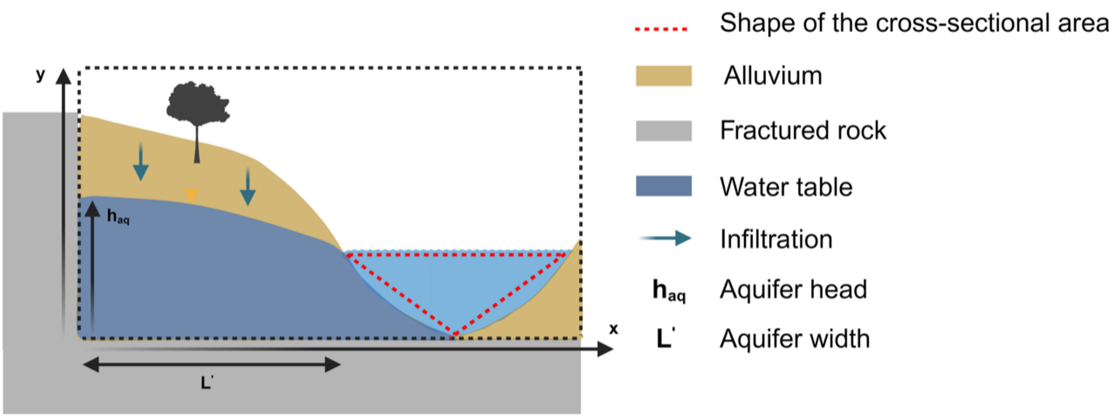

Source: prepared by the author.

Table S3.1 - Required parameters to run the numerical model.

Component	Required Parameter
River	Geometric shape of the channel cross-sectional area (-)
	Area (L^2), perimeter (L), hydraulic radius (L), and top width (L) of cross sections
	Channel length (L), channel slope (-)
	Inflow (L^3 T^{-1}), volume (L^3), river stage head (L)
	Area (L^2), and curve number (CN) of the incremental basin
	Daily evaporation (L), and rainfall (L)
	Hydraulic conductivity of the riverbed (L T^{-1})
Alluvium	Hydraulic conductivity (L T^{-1})
	Aquifer width (L)

Source: prepared by the author.

Table S3.2 - Rating curves for each river gauge.

River gauge	Rating curve
Cruzeirinho (N1)	$f(x) = 1.822x^{3.506}$
Mapuá (N2)	$f(x) = 33.252(x-0.420)^{1.844}$
Jaguaribe (N3)	$f(x) = 20.478(x-1.630)^{2.545}$

Monte Belizário (N4)	$f(x) = 21.039(x-0.640)^{2.076}$

Source: Toné *et al.* (2023).

Table S3.3 - Calibration values for the numerical model during Periods 1 (P1) and 2 (P2).

Period	Parameter	Reach 1	Reach 2	Reach 3
1	m	2.0	1.2	1.6
	γ^{+}	0.4	1.1	0.9
	γ^{-}	0.6	1.5	0.5
2	m	1.0	1.8	
	γ^{+}	2.0	0.7	
	γ^{-}	1.2	3.0	

Source: prepared by the author.

Figure S3.5 - Observed and estimated daily streamflow at reaches 1 (N1-N2), and 2 (N2-N3) during the calibration period 2 (01/04/2023 to 05/09/2023).

a)

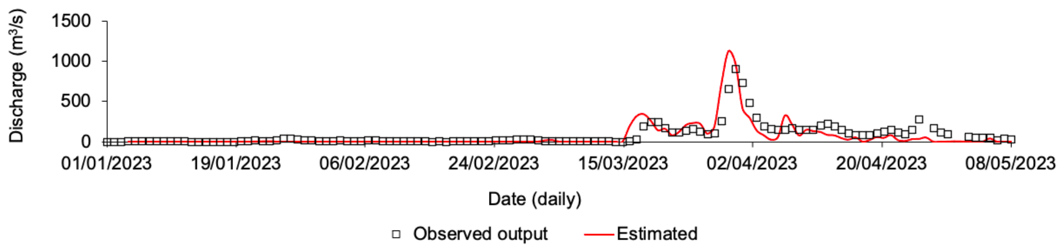

b)

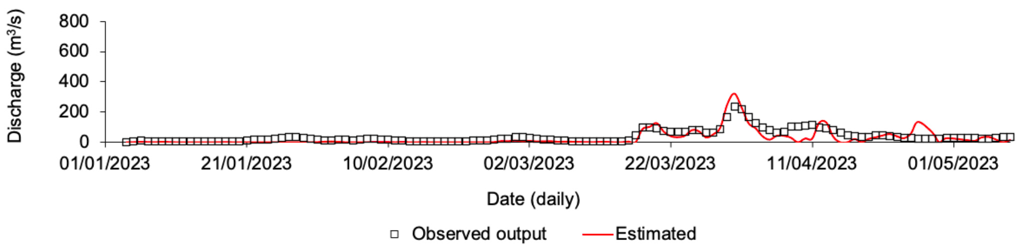

Source: prepared by the author.

Figure S3.6 - Observed and estimated daily streamflow at reaches 1 (N1-N2), 2 (N2-N3), and 3 (N3-N4) during the validation period 1 (04/01/2022 to 06/21/2022).

a)

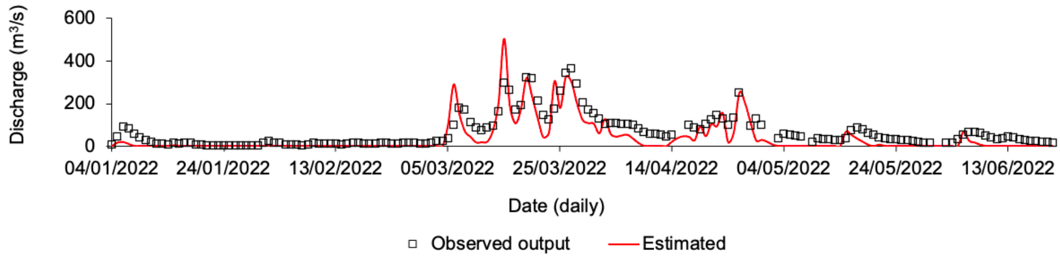

b)

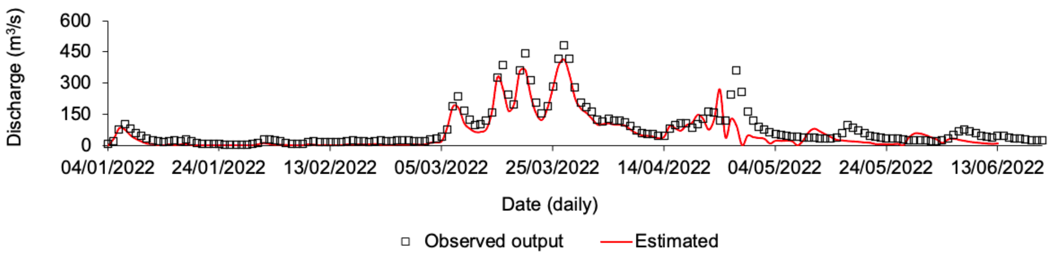

Source: prepared by the author.

Figure S3.7 compares the quantiles of the observed and simulated streamflow data over periods 1 and 2 at the study site, respectively. It is worth noting that the quantile-quantile plots do not consider time as one of their dimensions (Alves *et al.*, 2020), meaning that the maximum values of observed streamflow do not necessarily coincide with the maximum estimated streamflow at the same time step. Neither the observed nor the simulated data had a normal distribution; the 'S'-shaped curves in both figures suggest the presence of some outliers in the data. The estimated values are close to the observed values in both figures, indicating no significant departure between them.

Figure S3.7 - Quantile-Quantile plots comparing observed and estimated streamflow discharge for reaches 1 and 2 during the validation process in period 1 (a, b) and period 2 (d, e).

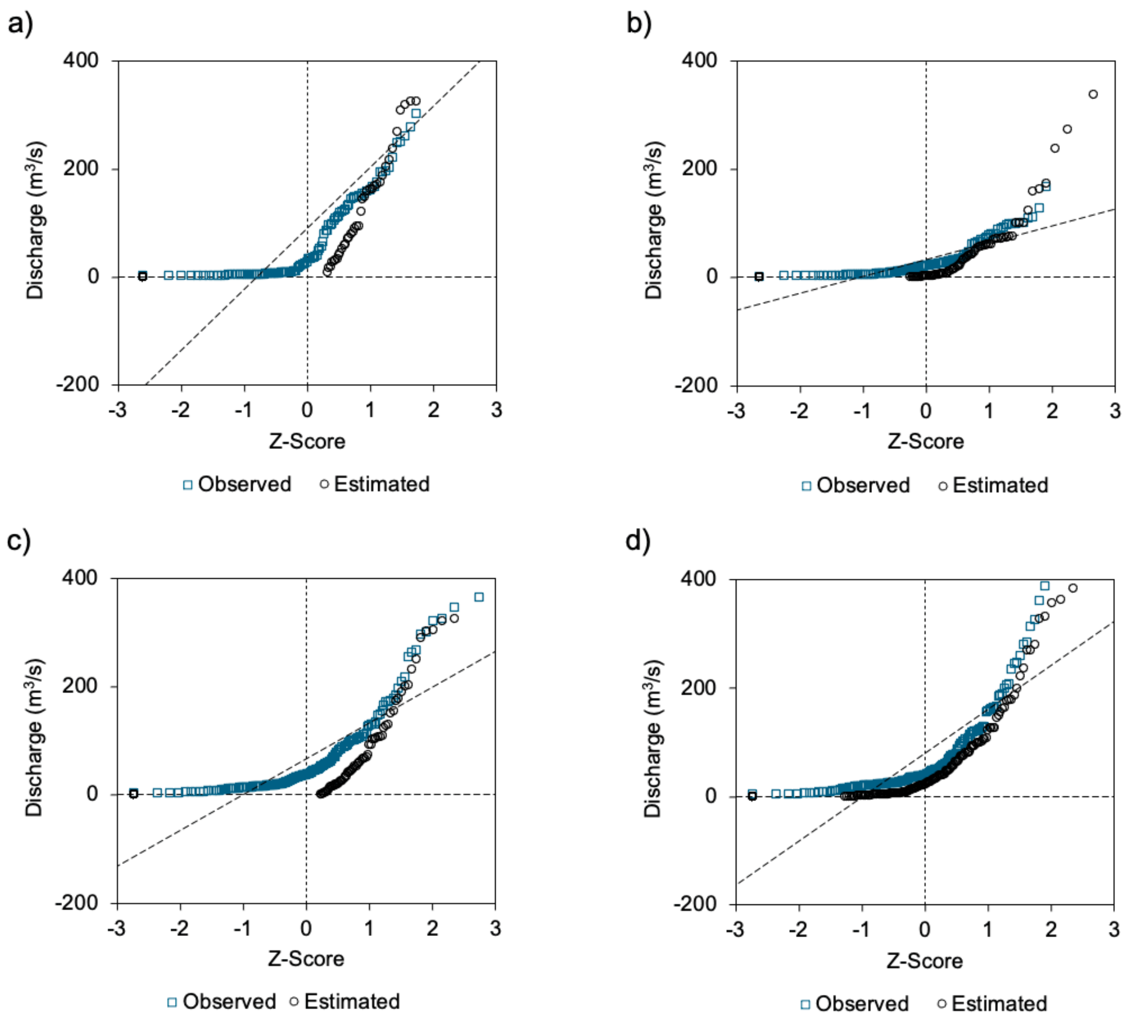

Source: prepared by the author.

Figure S3.8 - Observed inflow and estimated daily outflow at reaches 1 (a), 2 (b), and 3 (c) during calibration period 1.

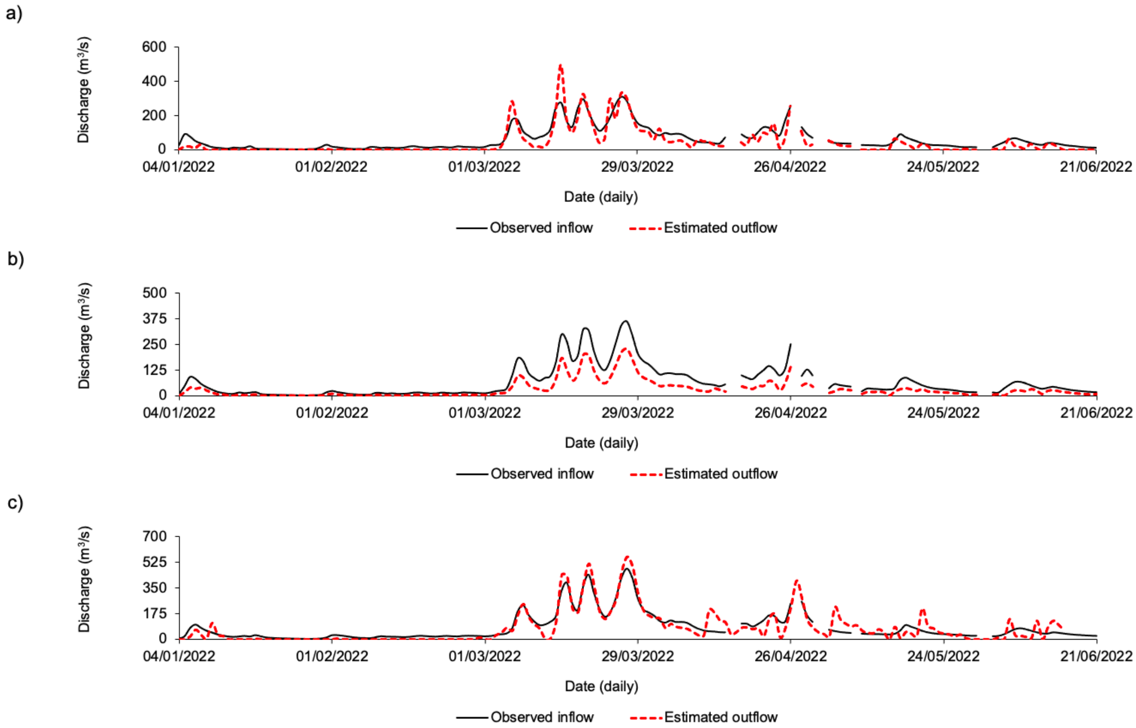

Source: prepared by the author.